AD-A177 950 APPLICATION OF NONDESTRUCTIVE TESTING TECHNIQUES TO MATERIALS TESTING(U) STANFORD UNIV CA EDWARD L GINZTON LAB OF PHYSICS G S KINO 1984 GL-4073 AFOSR-TR-87-0119 1/1

UNCLASSIFIED AFOSR-84-0063 F/G 14/2 NL

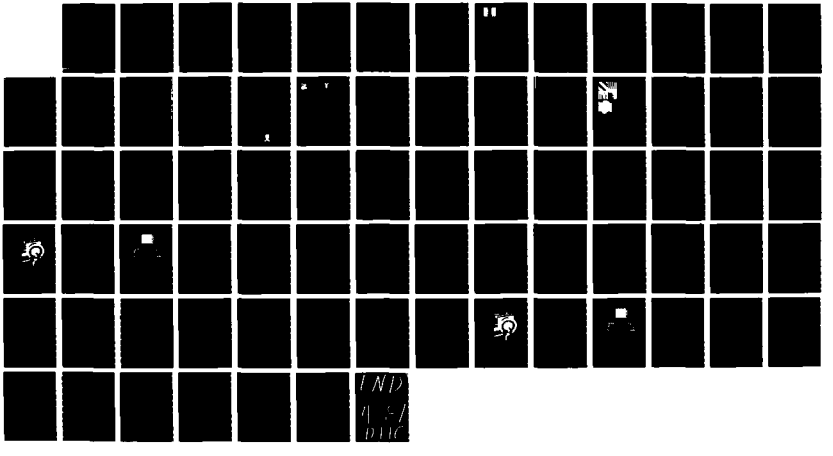

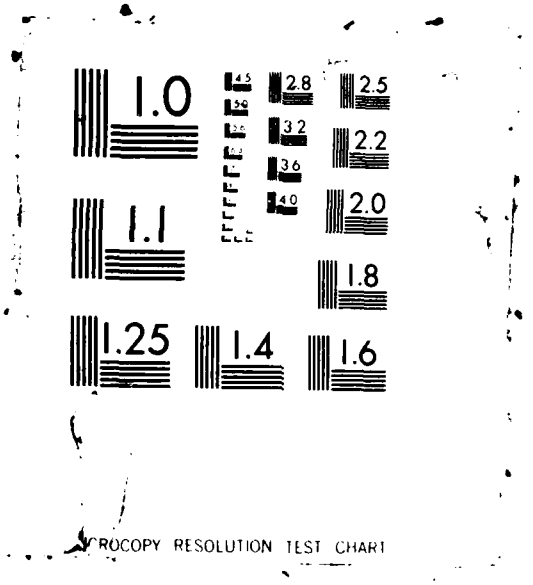
1.0
1.1
1.25
1.4
1.6
1.8
2.0
2.2
2.5
2.8
3.2
3.6
4.0
ROCOPY RESOLUTION TEST CHART

# AD-A177 950

## REPORT DOCUMENTATION PAGE

| | |
|---|---|
| 1a. REPORT SECURITY CLASSIFICATION: UNCLASSIFIED | 1b. RESTRICTIVE MARKINGS |
| 2a. SECURITY CLASSIFICATION AUTHORITY | 3. DISTRIBUTION/AVAILABILITY OF REPORT: Approved for public release; distribution unlimited. |
| 2b. DECLASSIFICATION/DOWNGRADING SCHEDULE | |
| 4. PERFORMING ORGANIZATION REPORT NUMBER(S) | 5. MONITORING ORGANIZATION REPORT NUMBER(S): ~~AFOSR-84-0063~~ AFOSR-TR-87-0119 |
| 6a. NAME OF PERFORMING ORGANIZATION: Stanford University; 6b. OFFICE SYMBOL (If applicable): | 7a. NAME OF MONITORING ORGANIZATION: AFOSR |
| 6c. ADDRESS (City, State and ZIP Code): Leland Stanford Jr. Univ. 660 Arguello Way Encina Hall Stanford CA 94305 | 7b. ADDRESS (City, State and ZIP Code): ~~B19 410~~ Bolling AFB DC 2033206448 |
| 8a. NAME OF FUNDING/SPONSORING ORGANIZATION: AFOSR; 8b. OFFICE SYMBOL (If applicable): NE | 9. PROCUREMENT INSTRUMENT IDENTIFICATION NUMBER: AFOSR-84-0063 |
| 8c. ADDRESS (City, State and ZIP Code): same as 7b | 10. SOURCE OF FUNDING NOS: PROGRAM ELEMENT NO. 61102F; PROJECT NO. 2306; TASK NO. A2; WORK UNIT NO. |
| 11. TITLE (Include Security Classification): Application of Nondestructive Testing Techniques To Materials Testing | |
| 12. PERSONAL AUTHOR(S): Kino | |
| 13a. TYPE OF REPORT: Annual; 13b. TIME COVERED: FROM 1-1-84 TO 12-31-84 | 14. DATE OF REPORT (Yr., Mo., Day): 1-1-4; 15. PAGE COUNT |
| 16. SUPPLEMENTARY NOTATION | |
| 17. COSATI CODES: FIELD; GROUP; SUB. GR. | 18. SUBJECT TERMS (Continue on reverse if necessary and identify by block number) |

19. ABSTRACT (Continue on reverse if necessary and identify by block number)

* ABSTRACT ON BACK *

DTIC FILE COPY

DTIC ELECTE MAR 1 2 1987

| | |
|---|---|
| 20. DISTRIBUTION/AVAILABILITY OF ABSTRACT: UNCLASSIFIED/UNLIMITED ☐ SAME AS RPT. ☐ DTIC USERS ☐ | 21. ABSTRACT SECURITY CLASSIFICATION: UUUU |
| 22a. NAME OF RESPONSIBLE INDIVIDUAL: Major Joseph Hager | 22b. TELEPHONE NUMBER (Include Area Code): 767-4931; 22c. OFFICE SYMBOL: NE |

DD FORM 1473, 83 APR EDITION OF ...

During the last year, we finished our work on electronic imaging. We have developed a new type of acoustic microscope which is capable of measuring both the phase and amplitude of an acoustic wave. With this system, we have been able to measure the thickness of films of a few thousand Angstroms thick using a 50 MHz microscope with an acoustic wavelength in water of 30um. microns An interesting feature has been that we can now measure the amplitude and phase of the V(z) curves (the variation in the amplitude of the signal received at the microscope determined as a function of the distance z of the surface of the solid object from the focus). The two papers on this subject to be published in the IEEE Ultrasonic Transactions in April 1985 form part of the Appendix of this report. During the year we have begun to work on a new type of scanning optical microscope which uses a Bragg cell to scan an optical beam. Our early results indicate that we can measure the thickness of transparent and opaque films to high accuracies.

A

B

2306-A2

One Year ~~Progress~~ Report

to

Air Force Office of Scientific Research

for

# APPLICATION OF NONDESTRUCTIVE TESTING TECHNIQUES TO MATERIALS TESTING

for the period

January 1, 1984 through December 31, 1984



G. L. Report No. 4073



Contract No. AFOSR-84-0063
Contract Period: January 1, 1984 through December 31, 1984
Amount of Contract: $198,473



Principal Investigator:
G. S. Kino



Edward L. Ginzton Laboratory
W. W. Hansen Laboratories of Physics
Stanford University
Stanford, California 94305

APPLICATION OF NONDESTRUCTIVE TESTING TECHNIQUES TO MATERIALS TESTING

by

G. S. Kino

## SYNTHETIC APERTURE IMAGING

During the last year, we finished our work on electronic imaging. This culminated in a Ph.D. thesis by Kent Peterson, "Real-Time Digital Synthetic-Aperture Image Reconstruction." We wrote an invited paper for the Special Issue on Digital Imaging of the IEEE Transactions on Sonics and Ultrasonics, "Real-Time Digital Image Reconstruction: A Description of Imaging Hardware and an Analysis of Quantization Errors," by D. K. Peterson and G. S. Kino. This work summarized a body of theory developed to determine the sidelobe, grating lobe, and digital errors that occur in synthetic aperture imaging and other imaging systems. The results, which are confirmed by experiments, are fundamental to the design of all computer processed imaging systems. The paper is included as an Appendix of this report.

## ACOUSTIC MICROSCROPY

We have developed a new type of acoustic microscope which is capable of measuring both the phase and amplitude of an acoustic wave. By using short tone bursts, we can separately measure the phase delay of the Rayleigh wave induced on a solid substrate, and the phase of the specular reflection from the substrate. Since we can measure phase to an accuracy of $0.1°$, it is possible to measure changes in height to an accuracy of better than a thousandth of a wavelength.

With this system, we have been able to measure the thickness of films of a few thousand Angstroms thick using a 50 MHz microscope with an acoustic wavelength in water of 30 μm . We have also used the device to determine the material properties of films and various types of solids by making extremely accurate measurements of the phase velocity of Rayleigh waves.

An interesting feature has been that we can now measure the amplitude and phase of the V(z) curves (the variation in the amplitude of the signal received at the microscope determined as a function of the distance z of the surface of the solid object from the focus). We have developed inverse Fourier transform procedures to invert this data that enable us to directly measure the longitudinal wave, shear wave, and Rayleigh wave velocities.

The two papers on this subject to be published in the IEEE Ultrasonic Transactions in April 1985 form part of the Appendix of this report.

## SCANNING OPTICAL MICROSCOPE

During the year we have begun to work on a new type of scanning optical microscope which uses a Bragg cell to scan an optical beam. The device is the first optical microscope capable of making quantitative measurements of optical amplitude and phase simultaneously. The concept arises directly out of our work on the acoustic microscope, where we began to realize how useful it is to measure both the amplitude and phase of the coherent wave. The work on the acoustic microscope also taught us how to eliminate speckle in a coherent wave system.

Our early results indicate that we can measure the thickness of transparent and opaque films to accuracies of the order of 30 A . A preprint of our work on this subject is included in the Appendix. A thesis is currently being finished on this work and on our fiber-optic sensor, "Characterization of Surface Variations Using Optical Interferometry," by R. L. Jungerman.

# Real-Time Digital Image Reconstruction: A Description of Imaging Hardware and an Analysis of Quantization Errors

D. K. PETERSON AND GORDON S. KINO, FELLOW, IEEE

*Invited Paper*

***Abstract*—General-purpose computers have been used to reconstruct images for more than two decades. Although computer-based reconstruction is versatile, it is notoriously slow. A real-time digital acoustic imaging system (called DAISY) is described, which is capable of reconstructing more than thirty new image frames per second. Both the imaging hardware and its operation are discussed. The latter portion of this paper is concerned with the effects of quantization errors in digital imaging systems. The discrete nature of both the data (digitized signal data) and the aperture (array apertures) are considered. The discussion is couched in general terms and is not specialized to acoustic imaging alone.**

## I. INTRODUCTION

GENERAL-PURPOSE digital computers have been used to reconstruct images for more than two decades now. Although computer-based reconstruction is versatile, it is notoriously slow. For some applications, such as oil exploration, this is only a nuisance. For other applications, real-time capability is a necessity. For instance, cardiac imaging, whether X-ray or acoustic, requires that images literally be reconstructed within a fraction of a heartbeat.

Real-time image reconstruction is also desirable because it allows interactive examination of the object. The operator obtains immediate feedback when the object is moved or changed. This makes it possible to adjust the position of the transducer to obtain an optimum image.

In most digital image reconstruction systems, the imaging process can be broken into two phases. First, the signal data is collected from a sequence of transducer positions or orientations (e.g., microwave antennas, X-ray detectors, acoustic transducers) and stored in a digital form for subsequent image reconstruction. Then the signal data is rearranged by one of several algorithms (backprojection, synthetic-aperture, holography, etc.) to reconstruct an image. As long as the signal data has been sampled above the Nyquist rate, a computer can be used to interpolate the data to any desired accuracy and to reconstruct the image.

Real-time digital imaging systems, on the other hand, do not enjoy the same luxury. Real-time interpolation of the data set would require a machine capable of hundreds of millions or even billions of interpolations per second. Currently, this is not feasible. Therefore, *real-time digital imaging systems must make direct use of the quantized data samples, as stored.*

In this paper we shall describe a real-time synthetic-aperture digital imaging system called DAISY (an acronym for digital acoustic imaging system). The basic operation of this system has been described elsewhere [6], [7]. The main application of DAISY is in acoustic nondestructive testing (NDT) of materials. Over the last several years, DAISY has been used in several NDT experiments ranging from imaging simple man-made defects [3] to the visualization of fatigue cracks using shear, longitudinal, and Rayleigh acoustic waves [14], [15]. As we gained experience with the imaging system, it became clear that there were certain aberrations in the images which were due, not to shortcomings of the hardware, but to quantization errors intrinsic in the image reconstruction algorithm itself. Indeed, as the hardware improved in quality, these aberrations became increasingly evident. Two examples are shown in Fig. 1. On the left is an image of a point target. In addition to the main lobe and barely perceptible sidelobes, there is a mottled region flanking the object in a sideways "bow-tie" shape which sags towards the left. At the right in Fig. 1 is the image of a flat specular (mirrorlike) reflector. The image shows the correct location and shape of the object, but also exhibits a fine "serration" pattern. It was found that aberrations such as these could be traced to quantization errors in the digital image reconstruction.

We have developed an analytic theory which explains the effects of quantization errors in the digital reconstruction, particularly quantization sidelobes in near-field images. These sidelobes are quantitatively and qualitatively different from those which have been considered in far-field imaging systems such as phased-array radar, and are closely related to the sidelobes of an optical Fresnel zone phase plate. This theory explains most of the characteristics of images observed in earlier experiments with DAISY (e.g., Fig. 1), and describes the dynamic-range limitations of real-time digital imaging systems due to quantization errors. These results pertain not only to digital synthetic-aperture imaging systems, but also, with minor changes, to other image reconstruction methods which use a finite number of array elements and/or a finite number of delay steps (e.g., real-time analog imaging systems

Manuscript received March 1, 1984; revised June 22, 1984. This work was supported under Air Force Office of Scientific Research Contract F49620-79-C-0217.

The authors are with Edward L. Ginzton Laboratory, W. W. Hansen Laboratories of Physics, Stanford University, Stanford, CA 94305.

0018-9537/84/0700-0337$1.00 

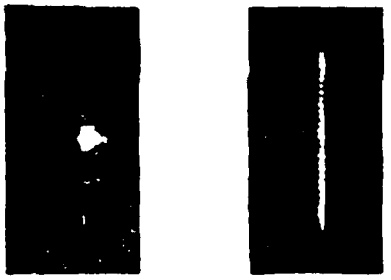


Fig. 1. Typical real-time images from DAISY. (a) A point object (thin wire in water). (b) A specular object (the edge of an aluminum block).

with switchable delay lines, charge coupled devices (CCD's) or other finite delay elements).

DAISY hardware and the execution of the image reconstruction algorithm with this hardware are described in Section II.

At the heart of the real-time reconstruction hardware is a so-called "focus map" which is a look-up table containing all of the information needed to reconstruct images in real time. The reasons for using a "focus map" are discussed in detail in Section III.

In Sections IV and V, we examine the effects of delay quantization errors on the point spread function (PSF) of an imaging system in both the far field and the near field. It is shown that delay quantization errors produce a series of "delay quantization lobes" in the far field and a series of "subsidiary foci" in the near field.

Then we turn our attention to the special problems encountered with digital imaging systems employing sampled apertures (i.e., systems which suffer from both temporal and spatial sampling errors). Section VI examines the effect on the point spread function, while Section VII examines the effect on images of specular reflectors.

Section VIII is a brief discussion of the effects of signal amplitude quantization errors.

## II. DAISY Hardware [1]

The main problem in making a time-delayed acoustic imaging system operating in real time is the provision of suitable delay elements. Lumped delay lines have been used for this purpose. Such delay lines tend to be bulky and limited in flexibility. CCD delay lines have also been suggested for this purpose [19]. This is an extremely attractive concept, but involves a great deal of technological development.

We chose instead a digital system in which the return echo signals are [illegible] in RAM's, and the time delay is obtained by [illegible] from the appropriate points in

[1] DAISY was designed [illegible] at P. D. C. at Stanford University around [illegible]. The [illegible] hardware refer to this thesis: "A Real-Time, Synthetic-Aperture, Digital Acoustic Imaging System," Ph.D. dissertation, E.E. Dept., Stanford University, also available as Ginzton Laboratory Report No. 3444, June 1982.

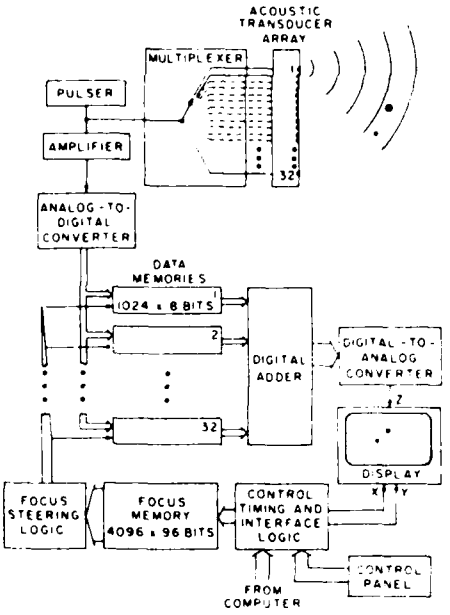


Fig. 2. Block diagram of DAISY hardware.

the RAM's. This has the great advantages of flexibility, relative ease of programming, and ever increasing availability of sophisticated high-speed digital components. It has the disadvantages of high power consumption and relatively expensive analog-to-digital (A-D) converters for real-time systems.

The DAISY hardware, illustrated in Fig. 2, employs a 32-to-1 multiplexer switch to address each of thirty-two elements of a piezoelectric acoustic transducer array. This has the advantage that only one A-D converter and receiver amplifier are required. A short pulse (typically about $2\frac{1}{2}$ cycles) with a center frequency of 3–3.5 MHz is transmitted from the selected element by exciting it with a unipolar pulse through the multiplexer. The return echoes to the same element are amplified, digitized, and stored in a 1024 × 8 bit RAM. This process is repeated, in turn, for each of the thirty-two elements in the array (with the current system the acoustic waves are always transmitted from and received on the same array element, but this is not a requirement for synthetic-aperture imaging). The echoes are thus stored in thirty-two independently addressable RAM's called the "data memory."

Each pixel in the focused image is reconstructed by applying the appropriate delays to each of the digitized time records and then summing the contributions from each element. The required time delays are stored in a 48 kilobyte "focus memory" in a condensed form as a lookup table called a "focus map." Simplifications required to limit the size of this focus memory are described in the next section.

The summing of the data stored in the image memory is carried out in a 32-byte input digital adder. The digital adder takes 1 byte of data from each of the thirty-two data memories and forms the 13-bit sum. The output of the adder is digitally rectified, then converted to a baseband video signal by the DAC.

The video signal is filtered, mixed with TV synch pulses and sent to the video monitor for display. The video signal is displayed in a 256-line noninterlaced format at a frame rate of

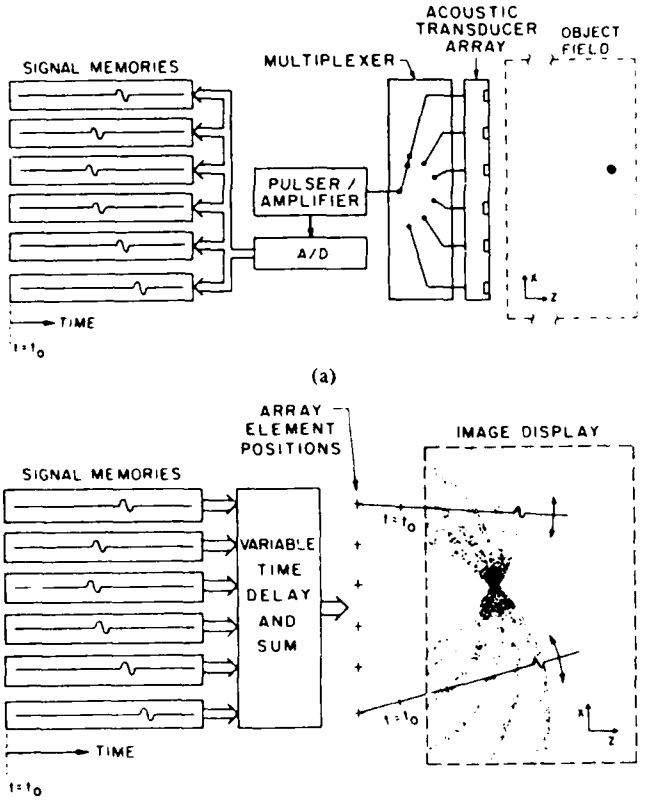


Fig. 3. Data recording and image reconstruction using the DAISY hardware. (a) The multiplexer selects a single element. A pulse is sent to that element; return echos are amplified, digitized, and stored in appropriate data memory. (b) Image is reconstructed from this data by summing contents of data memories after applying time delays appropriate for focusing. This is equivalent to "backprojection" of the data along circular arcs centered at the position of the collecting transducer element.

about 40 Hz. No video scan converter is required because the picture is generated at real-time rates in a standard raster format with the horizontal image lines perpendicular to the face of the transducer array.

The operation of the four subsystems of the imaging hardware are coordinated by the control and timing logic. The imaging hardware is organized as a parallel/pipeline processor made up of thirty-two parallel pipelines with seven stages in each pipe.

An interface to a laboratory computer is supplied for loading the focus memory with the appropriate focus map. After this process is carried out, the interface between the computer and the imaging hardware may be severed.

Using a clock rate of 10–15 MHz, DAISY generates about forty image frames per second. Since most of the transducer arrays have acoustic center frequencies of about 3 MHz, this gives three to five samples per wavelength, well above the Nyquist sampling rate.

Fig. 3 shows the collection and reconstruction of image data from a point object using a simplified, six-element imaging system. Note that the backprojection interpretation of image reconstruction is vividly apparent here. The echo data from each array element is backprojected in a circular arc whose center corresponds to the physical position of the array element. A single-element system would supply only one arc and so give only range information but no azimuthal information. As more elements are added to the array, the position of the object becomes more well defined.

## III. The Focus Map

### A. Look-Up Tables

In principle, the synthetic-aperture image reconstruction algorithm (or equivalently, the backprojection algorithm) requires computation of $N \cdot L \cdot P$ different distances, where $N$ is the number of transducer elements, $L$ is the number of lines in the image, and $P$ is the number of pixels in each line. For DAISY, this would be $32 \cdot 256 \cdot 1024 = 8$ million distances, each of which must be computed to 10-bit accuracy. At present, real-time computation of these distances is orders of magnitude beyond the capabilities of any general-purpose computing machine. Fortunately, there are solutions to this insurmountable computational obstacle.

Since the distance calculations do not change from one frame to the next, they may be computed once (on a general-purpose computer) and then stored in a high-speed look-up table, called a "focus map." By using a look-up table, one trades the problem of prodigious computing power for the problem of prodigious memory capacity.

The size of the focus map may be reduced by reconstructing the image in a radial sector scan format and assuming a paraxial geometry [19]. When this is done, the time-delay information can be separated into two one-dimensional focus maps: one for angle steering, another for range focusing; and the total time delay required is just the sum of these two components. The disadvantages of this approach are that only paraxial objects are well focused, and it requires a scan converter to translate from sector scan format into TV raster format.

For these reasons, DAISY was designed with a full two-dimensional focus map containing time delay information appropriate for direct reconstruction in a raster format. Therefore, the images have optimal resolution out to very large angles, and they can be presented in real-time directly on a standard TV monitor.

### B. Compression by Encoding

To backproject the data from any given array element onto any given image line (see Fig. 4), we require a set of distances (1024 in the case of DAISY) from the element located at $(x', 0)$ to each pixel $(x, z)$ in the line. Specifically, we need the value of

$$R_{x',x} = \sqrt{(x' - x)^2 + z^2}. \tag{1}$$

Fortunately, this is not a random collection of numbers; it is an ordered sequence of values monotonically increasing with $z$.

A common method of storing or representing a sequence of highly correlated values is "delta encoding." In this scheme, only the *difference* between a value and its successor is stored. In DAISY, the distance function is monotonically increasing, and can be represented by a binary sequence of 0's and 1's. By employing delta encoding, the look-up table can be compressed from a table of 10-bit distances to a table of 1-bit distance *increments*.

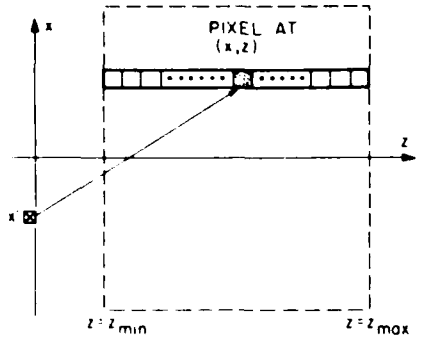


Fig. 4. Coordinates of the reconstructed image pixels. Transducer array lies along $x$ axis.

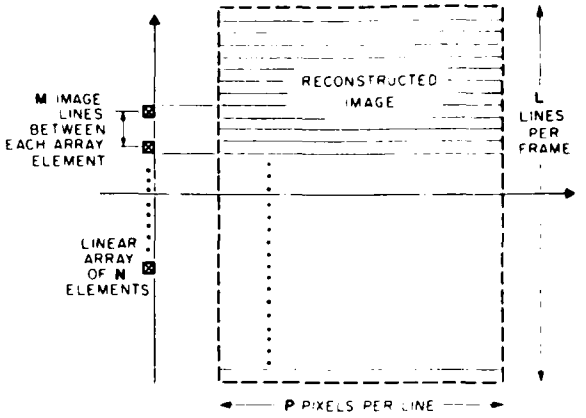


Fig. 5. Relationship between reconstructed image and array elements.

It should be noted that in delta encoding, one has made a trade-off between memory capacity and hardware complexity because additional hardware is needed to "decode" the encoded table values. In the case of delta encoding, this is extremely simple. An accumulator keeps the current distance value and the next value is obtained by adding the new, delta encoded, increment to this current value. In DAISY, the accumulator is a simple up-counter, and the binary sequence of increments is supplied to the clock input of each data memory address counter: a "1" causes the counter to increment and a "0" leaves the counter value unchanged. This small degree of added complexity is a small price to pay for the tenfold savings in focus memory capacity.

### C. Compression by Exploiting Symmetries

By exploiting the symmetries which are offered by a periodic image raster and a periodic array, we can decrease the size of the focus map still further.

Specifically, let us assume that the reconstructed image is to be $L$ lines by $P$ pixels per line, as shown in Fig. 5. The array has $N$ elements and is centered on the midline of the image field. Also, and this is very important, the spacing between the array elements is assumed to be some multiple $M$ of the spacing between the lines of the image raster. For DAISY these parameters are

$N$ = 32 elements

$L$ = 256 lines

$P$ = 1024 pixels/line

$M$ = 4 image lines between each array element position.

Because of the matching periodicities of the array and the image raster, there are only $(L + NM)/2$ unique element/line separations in the $x$ direction, shown as solid arrows in Fig. 6. The other possible element/line separations (shown as broken arrows) are redundant and need not be stored. For DAISY this reduces the size of the focus memory from 8096 lines to 2176 lines of focus data. Since each line of focus data is 1024 bytes, the total focus memory is now 192 kilobytes, a factor of 4 reduction.

*By using delta encoding and exploiting symmetries, the size of the focus memory is reduced from 1 megabytes to 24 kilobytes, an important savings in cost, size, complexity, and power consumption.*

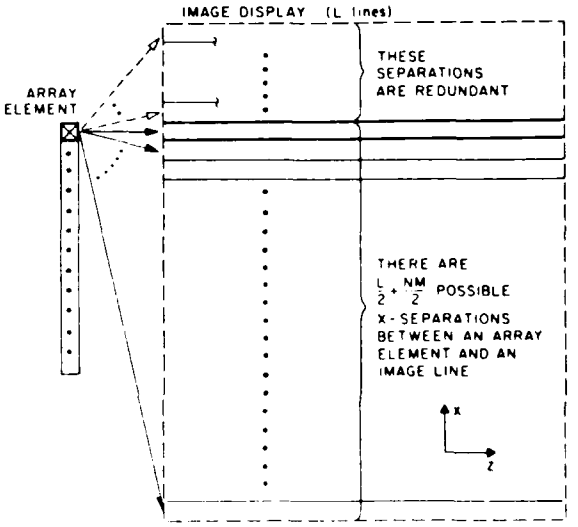


Fig. 6. Pictorial enumeration of all possible $x$ separations between an array element and an image line. Separations shown by the dashed arrows are redundant; only those $x$ separations represented by solid arrows need be stored.

The parallel architecture of DAISY makes it desirable, although not absolutely necessary, to organize the focus memory slightly differently than described above. In the architecture described two paragraphs above, some of the focus lines would need to be used by two different pipelines at the same time. Since there are $N$ pipeline channels running in parallel ($N$ = 32 for DAISY) it is more convenient to have $N$ *distinct* lines of focus data to feed each of the pipelines. The number of focus lines required for this slightly modified architecture is

(# of lines of focus data)

= (# of lines needed to represent distances to first line)

+ (# of new lines)

· (# of lines of focus data for each new line)

$= N + (L - 1) - 1.$ (2)

TABLE I

| Function | Parameter Subject to Quantization | Name Used in This Paper | Example |
|---|---|---|---|
| Imaging Signal $s(t)$ | $s(\cdot)$ | Signal amplitude quantization | The echo data are stored as 8-bit values |
| | $t$ | Delay quantization | The echo signal is periodically sampled and stored in a RAM (digital) or CCD (analog) |
| Pupil Function $P(x)$ | $P(\cdot)$ | Aperture amplitude quantization* | The aperture apodization profile is set by a digital command word |
| | $x$ | Array quantization | A transducer array is used to sample the aperture at periodic intervals |

*The effects of aperture amplitude quantization errors are a routine application of Fourier optics theory and will not be treated here as they are adequately discussed elsewhere [5] and [2].

For DAISY, this requires (32 + 255) kilobits or roughly 36 kilobytes of focus memory.[2] Such an architecture requires 50 percent more memory, but makes the focus steering logic less complex.

## IV. Delay Quantization Errors in the Far Field

All imaging systems share two common elements: 1) a spatially extended aperture represented by the so-called "pupil function," $P(x)$, and 2) an imaging signal $s(t)$, which carries information about the object back to the aperture.

In a digital imaging system, either or both of these functions may be quantized. The quantization can be of two different forms: 1) amplitude quantization, where the true amplitude is rounded off and represented by a finite length digital code, and 2) sampling quantization, where the value of the function is represented only at discrete values of the argument.

The possible sources of quantization errors in a digital imaging system are shown in Table I. A quantity which is not quantized will be referred to as "continuous" (e.g., continuous delays, continuous aperture).

In the early 1960's, the first microwave phased arrays were developed for electronically scanned radar systems. A linear phase shift across the elements of the microwave array was used to "steer" the beam off-axis. The phase shifters used in these systems could be programmed to select one of several discrete phase delays. It was found that phase quantization errors introduce so-called "quantization lobes" in the far field which are similar in appearance to the grating lobes caused by using an undersampled array [1], [12], [5], and [17]. More recently, acoustic phased array systems have been shown to exhibit similar "quantization lobes" [11].

In this section we will recapitulate the early theory of phase delay quantization in the far field, both because it is interesting in its own right and because it is a convenient vehicle for introducing some notation and concepts which will be used again in the next section where we analyze the more difficult problem of delay quantization in the near field.

[2] For historical reasons DAISY's focus map is split into four independent sections, each of which is capable of reconstructing 64 image lines. Therefore, the amount of focus memory in DAISY is actually 4[32 + (64 − 1)] kilobits or about 48 kilobytes.

### A. Phase Quantization and Phase Quantization Errors

For a system with no quantization errors, the phase delays are continuously variable over the interval $[0, 2\pi)$. In a digital system only a finite number of phase delays is available. We denote by $\mu$ the number of delays available within the interval $[0, 2\pi)$. For instance, if $\mu = 2$ (as in a Fresnel zone phase plate), phase delays of 0 and $\pi$ are used. The quantized phase delay will be represented by the notation $[\phi]_{2\pi/\mu}$ where $\phi$ is the continuous phase variable being quantized, and $2\pi/\mu$ is the phase quantization interval. This function is shown in Fig. 7(a). The quantization *error* is represented by the notation $\epsilon_{2\pi/\mu}(\phi)$, defined as

$$\epsilon_{2\pi/\mu}(\phi) = [\phi]_{2\pi/\mu} - \phi, \tag{3}$$

and shown in Fig. 7(b). It is a periodic function with period $2\pi/\mu$, the quantization interval. In the future we will omit the subscript $2\pi/\mu$, unless it is required for clarity.

Subsequently, we will use the periodic function $\exp[i\epsilon(\phi)]$ which can be represented by the following Fourier series

$$\exp[i\epsilon(\phi)] = \sum_{m=-\infty}^{\infty} A_m e^{im\mu\phi},$$

where

$$A_m = \operatorname{sinc}(m+1,\mu) = \frac{(-1)^m \sin(\pi/\mu)}{\pi(m+1,\mu)}. \tag{4}$$

### B. Far-Field PSF of an Imaging System with Continuous Delays

In phase steered systems the beam is pointed off-axis at an angle $\theta_0$ by applying a linear phase taper across the aperture.[3] This is represented by a complex valued pupil function

$$P(x') = \exp(-i2\pi x' \sin\theta_0/\lambda) \operatorname{rect}(x'/D), \tag{5}$$

where rect is the rectangle function and $D$ is the width of the aperture. The far field beam pattern is simply the Fourier

[3] Here, and throughout the rest of the paper, we will consider the case in a two-dimensional plane using a one dimensional aperture. For the moment we shall assume that the aperture is continuous.

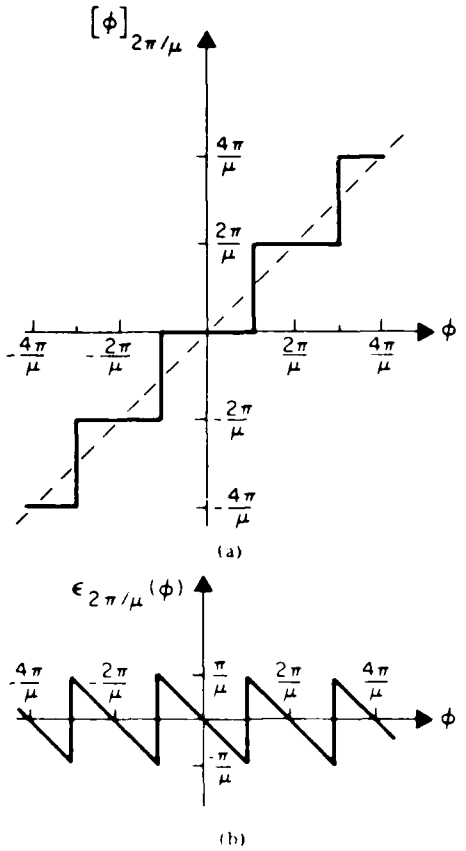


Fig. 7. (a) Plot of quantized phase function $[\phi]_{2\pi/\mu}$. (b) Plot of phase quantization error function $\epsilon_{2\pi/\mu}(\phi)$.

transform of the pupil function[4] [9]:

$$U(r,\theta) = \mathcal{F}\{P(x')\} = D \operatorname{sinc}[(\theta - \theta_0) D/\lambda] \cdot e^{i2\pi r/\lambda}. \tag{6}$$

A plot of a typical far-field beam pattern (with $D = 100\ \lambda$, $\theta_0 = 0.05$ radian, and $r = 20\,000\ \lambda$) is shown in Fig. 8(a).

### C. Far-Field PSF of an Imaging System with Quantized Delays

In a digital phased array system, the phase is quantized and the pupil function becomes

$$P_{\text{quant}}(x') = \exp\{-i[2\pi x' \sin\theta_0/\lambda]_{2\pi/\mu}\} \cdot \Pi(x'/D), \tag{7}$$

where $[\ ]_{2\pi/\mu}$ represents the quantization of phase into $2\pi/\mu$ radian intervals. Substitution of (3) and (5) yields

$$P_{\text{quant}}(x') = \exp\{-i\epsilon(2\pi x' \sin\theta_0/\lambda)\} \cdot P(x'). \tag{8}$$

Again, the far-field beam pattern is given by the Fourier transform of the pupil function:

$$U_{\text{quant}}(r,\theta) = \mathcal{F}\{P_{\text{quant}}(x')\} = \mathcal{F}\{\exp(-i\epsilon_{2\pi/\mu}(2\pi x' \sin\theta_0/\lambda))\} * U(r,\theta), \tag{9}$$

[4] For some purposes it is convenient to use polar coordinates $(r,\theta)$, and for others it is easier to use rectangular coordinates $(x,z)$. In this paper we will use both. The origins of both coordinate systems lie at the center of the aperture, with the $z$ axis (or $\theta = 0$ radian) perpendicular to the aperture so that $x = r\sin\theta$, and $z = r\cos\theta$.

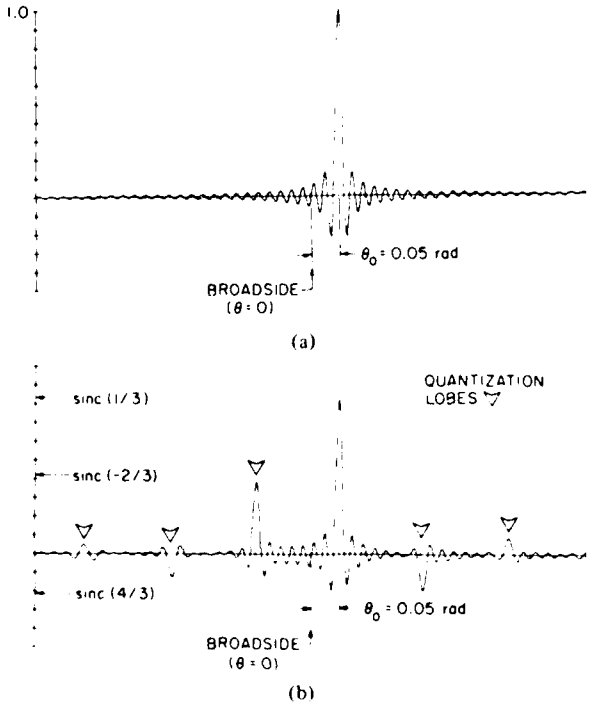


Fig. 8. Far-field PSF of a continuous aperture imaging system. (a) With continuous phase delays. (b) With quantized phase delays ($\mu = 3$).

where the asterisk represents the convolution operator. At this point, we make use of the Fourier series representation of $e^{i\epsilon}$ mentioned earlier (4) to obtain

$$U_{\text{quant}}(r,\theta) = \sum_{m=-\infty}^{\infty} \operatorname{sinc}(m+1/\mu) \cdot U(r, \theta + m\mu\theta_0). \tag{10}$$

Eq. (10) states that *the far-field beam pattern for an imaging system with quantized phase delays contains a mainlobe* ($m = 0$) *of diminished amplitude* $A_0 = \operatorname{sinc}(1/\mu)$ *and a series of "delay quantization lobes"* ($m \neq 0$) *of amplitude* $A_m = \operatorname{sinc}(m + 1/\mu)$ *located at* $\theta = (1 + m\mu)\theta_0$. *Therefore, in the far-field, the effect of phase quantization is very similar in appearance to that of grating lobes.* The delay quantization lobes are due to a periodic phase error across the aperture, while grating lobes are due to a periodic amplitude error. As one would expect, when $\mu$ is large (i.e., the phase delays are finely quantized), the quantization lobes diminish in amplitude and move far away from the mainlobe. Fig. 8(b) shows the far-field beam pattern of an imaging system using quantized delays (with $D = 100\ \lambda$, $r = 20\,000\ \lambda$, $\theta_0 = 0.05$ radian, and $\mu = 3$).

## V. Delay Quantization Errors in the Near Field

Phased array radars work in the far field of the antenna. In acoustic imaging one often works in the near field of the acoustic array, employing (roughly parabolic) phase curvature for dynamic focusing, as well as linear phase taper for beam steering. Bates has investigated the effects of phase quantization errors on a beam-forming imaging system which used a digital delay line to accomplish the phase delays [2]. In his

analysis, it was necessary to assume that the quantization errors were very small and could be treated as a perturbation of the pupil function. It was also necessary to assume that the aperture consisted of a periodic array. Then the magnitude and position of the quantization sidelobes could be estimated if certain phase matching conditions were satisfied.

In this section we go back to the earlier theory developed for quantization errors in the far field (described in the previous section) and generalize it to treat the case of quantization errors in the near field. This new theory is exact (within the paraxial approximation) and has a simple physical interpretation. The theory is first developed for a continuous aperture so the effects of delay quantization are not complicated by the effects of array quantization. The analysis of delay quantization in array systems will be left to the following two sections.

We will consider the effect of using digitized signal data in a synthetic-aperture imaging system, such as DAISY. The theory for dynamically focused systems using quantized phase (or time) delay elements is very similar and does not justify a separate treatment.

It is assumed that the imaging signal has spatial and time harmonic dependence of the form

$$\cos(\omega t - kz) = \mathrm{Re}\{e^{i(\omega t - kz)}\}. \tag{11}$$

We will work with the complex exponential representation, bearing in mind that it is the real component which interests us. At the end of the section we will comment on the effects of using broad-band imaging signals.

### A. Near-Field PSF of an Imaging System with Continuous Delays

Consider an infinitesimal aperture element at position $(x', 0)$ in the aperture (see Fig. 9). The element is excited with a continuous wave (CW) signal $e^{i\omega t}$. The echo received from an object at location $(x_0, z_0)$ is delayed by a round-trip transit delay of $2R_{x',x_0}/v$ where $v$ is the wave velocity in the intervening medium,[2] and is scaled by a factor $1/R$ due to round-trip diffraction loss. (This factor would be $1/R^2$ in three dimensions). Therefore, the signal received at the point $(x', 0)$ in the aperture, due to a reflector at $(x_0, z_0)$, is

$$s(x', 0; x_0, z_0, t) = \exp\left\{i\omega\left(t - \frac{2}{v}R_{x',x_0}\right)\right\}/R_{x',x_0}. \tag{12}$$

To reconstruct the image amplitude at $(x, z)$, one "synthesizes a lens" which is focused at $(x, z)$. This is done by summing together the signals received at each of the aperture elements, after delaying each by an amount $2R_{x',x}/v$, to obtain

[2] In optics the wave propagation is usually "one way" from the source to the aperture so that the transit times are of the form $kR$. In radar or sonar, where the illumination comes from the aperture itself, the wave takes a "two-way" or "round-trip" path so that the transit times are of the form $2R/v$. This factor of two causes constantly occur discrepancies between synthetic-aperture imaging and optical imaging.

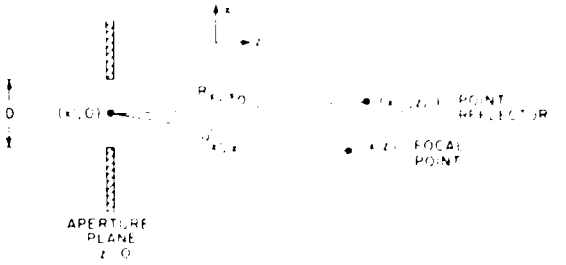


Fig. 9. Distances $R_{x',x_0}$ and $R_{x',x}$ used in near-field image reconstruction.

$$U(x, z; x_0, z_0) = \int dx' P(x') s\left(x', 0, x_0, z_0, t = \frac{2}{v}R_{x',x}\right)$$

$$= \int_{-D/2}^{D/2} dx' \exp\left\{i\omega\frac{2}{v}(R_{x',x} - R_{x',x_0})\right\}/R_{x',x_0}. \tag{13}$$

If we assume paraxial geometry, so that

$$R_{x',x} \approx z + \frac{(x' - x)^2}{2z}$$

and

$$R_{x',x_0} \approx z_0 + \frac{(x' - x_0)^2}{2z_0}, \tag{14}$$

then the PSF in the plane of the object ($z = z_0$) can be written in closed form as:

$$U(x, z_0, x_0, z_0) = \frac{D}{z_0} e^{i\pi(x - x_0)^2/\lambda z_0} \cdot \mathrm{sinc}\frac{x - x_0}{\lambda z_0/2D}. \tag{15}$$

This is the familiar result from diffraction theory for one-dimensional lenses, except that here the Rayleigh resolution ($\lambda z_0/2D$) is improved by a factor of two due to the use of "round-trip" phase delays.

Fig. 10 is a plot of the near-field PSF for an imaging system with continuous delays ($\lambda = 1$, $D = 80$, and $z_0 = 400$).[3] In this figure, as in the other PSF plots presented in this paper, the paraxial approximation is *not* used, since it is our purpose to compare the mathematical theory developed here with the performance of a large numerical aperture imaging system, such as DAISY.

### B. Near-Field PSF for an Imaging System with Quantized Delays

In a digital system the echo received by each aperture element is digitized and stored at periodic sampling intervals. How are the above results affected by quantization of the time samples?

[3] This PSF is [illegible] PSF. Since it is plotted on a [illegible] it is [illegible] phase [illegible] PSF. This is shown explicitly in (15).

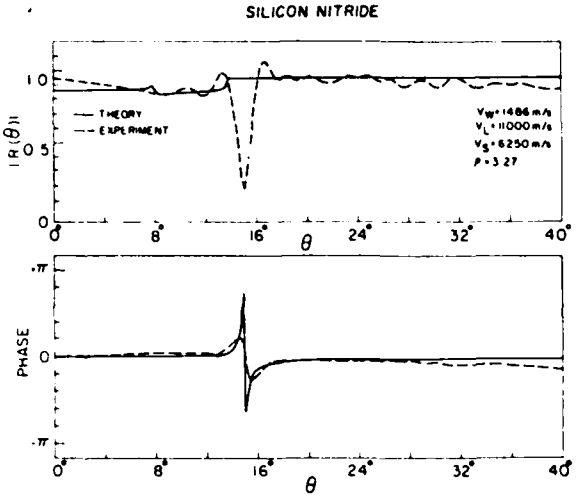


Fig. 11. Comparison of the theoretical and experimental reflectance function for the water-silicon-nitride interface.

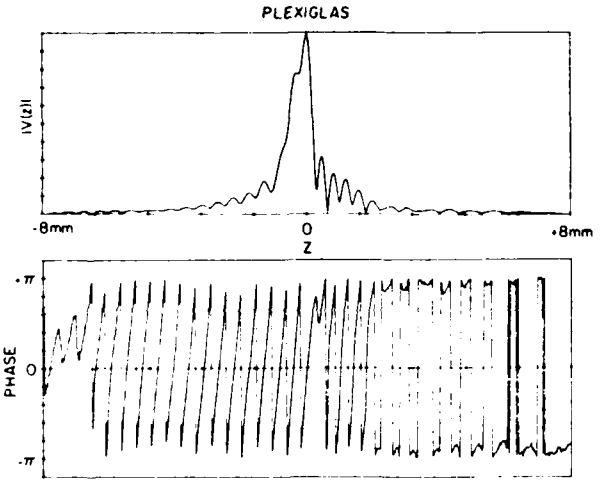


Fig. 12. Experimental $V(z)$ of a water-Plexiglas interface at 10.17 MHz.

nique does not preclude the characterization of such acoustic properties as shear loss, temperature dependence of the Rayleigh-wave velocity, and various contributing factors to the Rayleigh critical-angle phenomenon.

### *Plexiglas*

Figs. 12 and 13 are the $V(z)$ and $R(\theta)$, respectively, for plexiglas or lucite, a low-acoustic velocity and high loss material. This example illustrates how material loss can be determined. The longitudinal critical angle is located at $\theta = 32.7°$, which corresponds to a longitudinal wave velocity of 2750 m/s. The magnitude of the reflectance peaks at 0.7 rather than one, as it would be for a lossless substrate. The amount of diminution of the peak level depends on the loss for the longitudinal mode. The theoretical curve is fitted to the experimental one by varying the longitudinal loss factor $Q_L$. The $Q_L$ is found to be about 50, which translates into an attenuation coefficient of 232 Np/m or 20 dB/cm at 10 MHz, which agrees well with other published values [16].

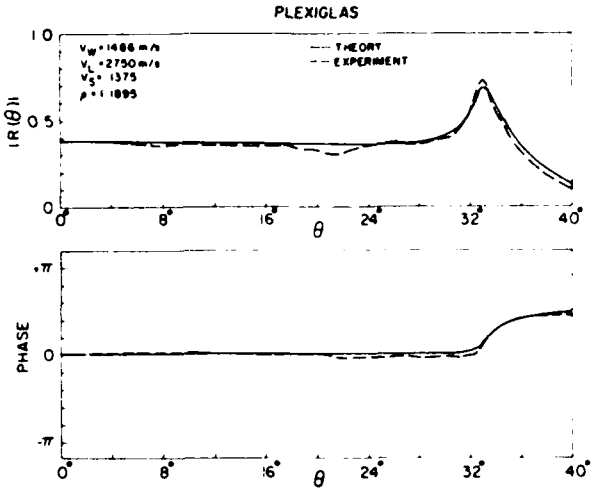


Fig. 13. Comparison of the theoretical and experimental reflectance function for a water-Plexiglas interface.

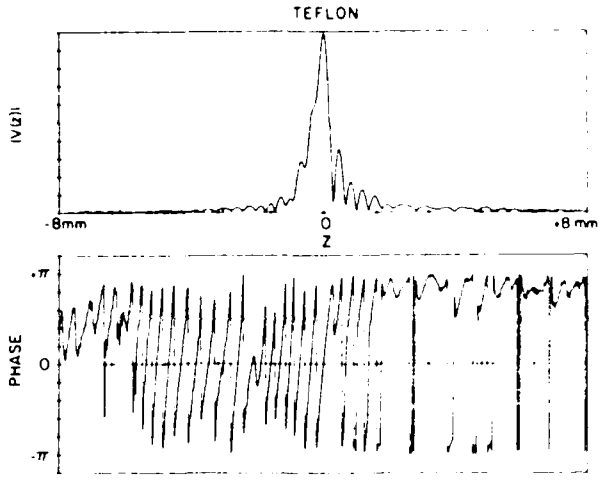


Fig. 14. Experimental $V(z)$ of a water-teflon interface at 10.17 MHz.

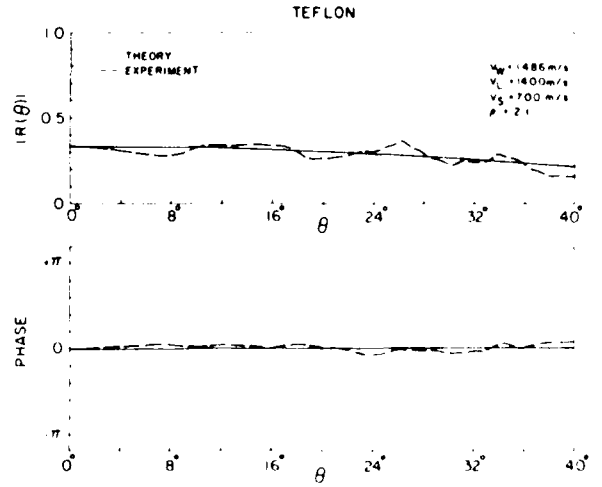


Fig. 15. Comparison of the theoretical and experimental reflectance function for a water-teflon interface.

### *Teflon*

$V(z)$ and $R(\theta)$ for teflon are displayed in Figs. 14 and 15. As expected no critical angle is observed, since teflon

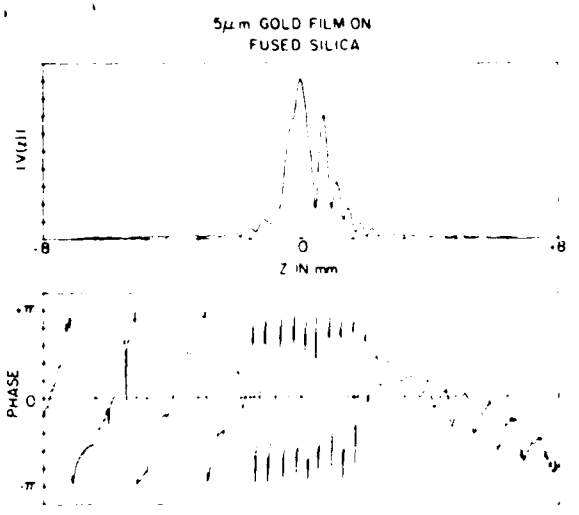


Fig. 16. Experimental $V(z)$ of a water and 5-$\mu$m gold film on a fused-silica interface at 10.7 MHz.

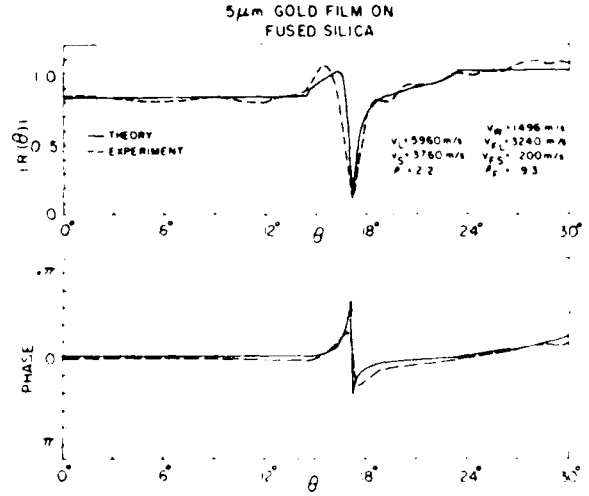


Fig. 17. Comparison of the theoretical and experimental reflectance function for a water and 5-$\mu$m gold film on a fused-silica interface.

has a longitudinal velocity of 1400 m/s, which is lower than that of water.

### *Thin-Film Measurement*

The following example demonstrates the potential application of acoustic microscopy in thin-film characterization and also confirms a thin-film matching phenomenon predicted by numerical computation. The thin-film structure used in this example is a 5-$\mu$m-thick gold film deposited on a fused-silica substrate. At 10 MHz the thickness of the gold film corresponds to about 1.5 percent of the longitudinal wavelength. Figs. 16 and 17 are the plots of $V(z)$ and $R(\theta)$, respectively. The agreement with the theoretically generated $R(\theta)$ is good. $R(\theta)$ shows a null at $\theta = 17.23°$, an angle between the longitudinal and shear critical angles of the fused silica substrate. Physically this means that the incident longitudinal mode in water couples very strongly into a bulk propagating mode in the fused silica substrate. The physics of this coupling is not well understood, but it is believed that the longitudinal wave in water converts in the gold film to a leaky Sezawa wave, which leaks into the fused silica substrate in the form of a propagating shear wave. The coupling efficiency and the angle of incidence, at which maximum transmission occurs, have been shown to be functions of the film thickness by numerical analysis. Thus by measuring the reflectance, one can get information about the film thickness. The experimental demonstration of this thin-film phenomenon also opens up the possibility of using the thin-film matching technique in the design of acoustic transducers to improve the transmission efficiency between two media with vastly different acoustic impedances.

## V. Error Analysis

The introduction of experimental artifacts in the experimental $R(\theta)$ due to the spatial truncation of the $V(z)$ curve is treated in this section. This problem arises because of the finite distance over which $V(z)$ data can be collected. Equation (26) shows that $V(u)$ and $[P^2(t)R(t)]$ form a Fourier-transform pair. It can be shown by Fourier-transform theory that since $[P^2(t)R(t)]$ is finite in the $t$ domain, $V(u)$ has to be infinite in the $u$ domain. Experimentally $V(z)$ can only be obtained for some finite-width data window. Therefore the actual waveform $V'(z)$ used in the inversion is a truncated version of $V(u)$. Thus

$$V'(u) = V(u) \text{ rect } (u/D) \tag{32}$$

where $u = z/\lambda$, and $D$ is the width of the data window defined in terms of the number of wavelengths in water. Noting that multiplication in the $u$ domain corresponds to convolution in the transform domain $t$, the reflectance function obtained by inverting $V'(u)$ is

$$[P^2(t)R(t)]' = [P^2(t)\ R(t)]^* D \text{ sinc } (Dt) \tag{33}$$

where * denotes convolution.

The effects of the convolution between the reflectance function and the waveform sinc $(Dt)$ are twofold. First, the angular resolution in the $t$ domain is degraded. Second, because of the oscillatory nature of sinc $(Dt)$, sharp features in $P^2(t)R(t)$ tend to generate ripples in the resulting $[P^2(t)R(t)]'$. The resolution degradation effect can be estimated as follows. The full width between zeroes of the main lobe of sinc $(Dt)$ is

$$\Delta t = 2/D. \tag{34}$$

The $\Delta t$ is essentially the transition width of the response to a sharp step in $P^2(t)R(t)$ and hence can be regarded as the worst case resolution in $t$. Using the relation $t = 2 \cos \theta$ given in (24), we get the following expression for the angular resolution in terms of the angle of incidence $\theta$

$$\Delta\theta = \frac{\Delta t}{2 \sin \theta}. \tag{35}$$

Combining (34) and (35), the resolution in $\theta$ in terms of the width of the data window $D$ is found to be

$$\Delta\theta = \frac{1}{D \sin \theta}. \tag{36}$$

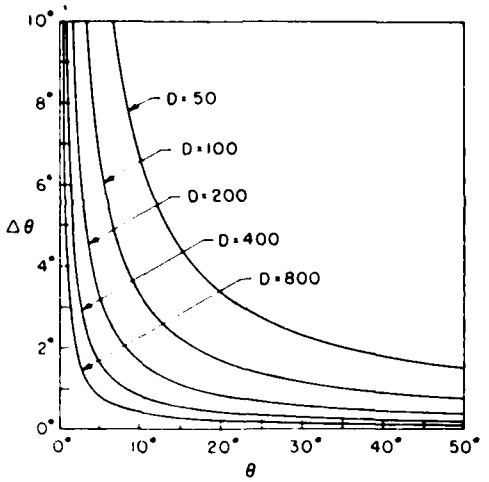


Fig. 18. Variation of angular resolution degradation as a function of the incident angle and the normalized data window width $D$.

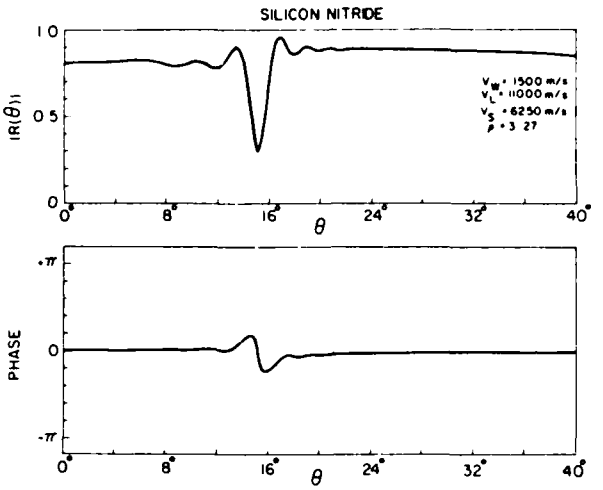


Fig. 19. Simulated reflectance function of a water-silicon nitride interface obtained by inverting spatially truncation $V(z)$ data.

Equation (36) is plotted in Fig. 18 with $D$ as a parameter. The data window $D$ used in the experiment is about 100. This implies angular resolution of about 3.3° at $\theta$ = 10°, 1.7° at $\theta$ = 20°, and 1.1° at $\theta$ = 30°. The experimental reflectance of silicon nitride in Fig. 11 is a pathological example of the degradation effect of this angular resolution. The Rayleigh critical angle occurs at a low value of $\theta$ = 15.0° and in the vicinity of this angle, the magnitude of the reflectance is unity but the phase goes through a rapid $2\pi$ radian change over a 2° angular range. The net result of the convolution with sinc ($Dt$) is a sharp dip in the magnitude of the experimental reflectance and a smoothing of the phase curve near the Rayleigh critical angle. The effect of the convolution is much less serious at angles of high incidence as shown in Fig. 18 and as evidenced by the experimental $R(\theta)$'s of fused silica and aluminum, where only a slight dip occurs in the reflectance magnitude.

A computer simulation has been carried out where the theoretical $R(\theta)$ for silicon nitride is used to generate the $V(z)$, which is truncated and then inverted in an identical manner to the experimental data. The result is shown in Fig. 19. The simulated $R(\theta)$ exhibits exactly the same behavior in both amplitude and phase as the experimental one in Fig. 11.

The locations of the critical angles are generally used to determine the phase velocities of propagating modes, which are given by

$$v_* = v_w/\sin\theta_*$$

where $v_w$ is the velocity in water; the asterisk stands for $L$ (longitudinal), $S$ (shear), or $R$ (Rayleigh); and the subscript $c$ denotes critical angle. The percentage error in the estimation of $v_*$ as a consequence of the truncation of $V(z)$ can be shown to be

$$\left|\frac{\Delta v_*}{v_*}\right| = \frac{1}{2}\frac{\cos\theta_*}{\sin\theta_*}\,\Delta\theta_* = \frac{1}{2}\frac{\cos\theta}{D\sin^2\theta}. \tag{37}$$

Equation (37) is plotted in Fig. 20 with $D$ as a parameter.

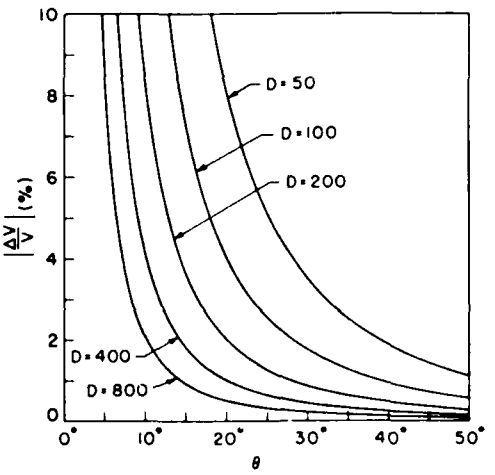


Fig. 20. Phase velocity estimation error as a function of angle of incidence due to degradation of the angular resolution.

The error decreases drastically with increasing incidence and increasing $D$. For $D$ = 100, $|\Delta v_*/v_*|$ is four percent at $\theta$ = 20° and 1.75 percent at $\theta$ = 30°. One should bear in mind that (37) represents the worst-case estimation, and the actual error could well be substantially smaller, especially for the Rayleigh critical angle $\theta_{Rc}$. The determination of $\theta_{Rc}$ involves locating the point, where the phase of $R(\theta)$ is $\pi$ radians. Around $\theta_{Rc}$ the magnitude of the reflectance function for a lossless material is constant while the phase $\Psi$ can be shown to have the form [9]

$$\tan\Psi = 2\,\frac{k_r - k\sin\theta_{Rc}}{\alpha} \tag{38}$$

where $\alpha$ is the leak rate of the Rayleigh wave. The phase function $\Psi$ is the antisymmetric in $k_r$ about $\Psi = \pi$ around the point $k_r = k\sin\theta_{Rc}$. It is similarly antisymmetric in $k_z$ or $t$ in the neighborhood of $k_z = k\cos\theta_{Rc}$. Since the sinc function with which $[P^2(t)R(t)]$ is convolved is symmetric, the phase function $\Psi$ around the Rayleigh critical angle remains essentially unchanged by the convolution,

provided that the width of the main lobe of the sinc function $\Delta t$ is smaller than the transition width of $\Psi$ through the Rayleigh critical-angle region. For example, in the case of fused silica and aluminum, the respective leaky surface-acoustic-wave velocities calculated from the experimental phase curve are almost identical to those predicted by theory.

The second problem associated with the generation of ripples can be partly remedied, though with some further loss in angular resolution, by applying a smooth apodization function for the $V(z)$ data before inversion takes place. The apodization function used in processing the $V(z)$ data is

$$a(u) = \frac{\sin^2(\pi u/D)}{n + \sin^2(\pi u/D)} \tag{38}$$

where $n$ is a free parameter for adjusting the tapering characteristics of the apodization. The $n = 0.1$ is used to process the experimental data shown here. The resulting apodization essentially leaves the data in the center of the window unchanged, but it behaves much like Hamming weighting at the edges of the data window.

The obvious solution to both the resolution degradation and ripple problems is to increase the data window width $D$ of $V'(u)$. Equation (31) shows that this can be realized by increasing the radius of curvature $f_0$ or reducing the aperture size or both. Also $D$ can be increased by increasing the frequency of operation. For silicon nitride, $R(\theta)$ can be reproduced much more faithfully if $\Delta\theta$ is reduced to $\frac{1}{4}^\circ$, which can be achieved by using an $F/1.5$ lens with a focal length of 32 mm operating at 20 MHz.

Another important source of error is in the estimation of the velocity of water. Since

$$u = z/\lambda = zf/v$$

then

$$du = -\frac{zf}{v^2}\,dv = -u\,dv/v. \tag{39}$$

Suppose the wrong velocity is used in the inversion. In (25) this is equivalent to changing $u$ to

$$u' = u + \Delta u = u(1 - \Delta v/v). \tag{40}$$

The resulting inversion is given by

$$[P^2(t)R(t)]' = \int V(u)\exp[j2\pi u(1 - \Delta v/v)t]\,du$$

or

$$[P^2(t)R(t)]' = P^2R[(1 - \Delta v/v)t]. \tag{41}$$

Therefore using an erroneous $v$ results in a stretched reflectance function in $t$. Since the velocity of water has a large temperature coefficient, 4 m/s per °C, this error can be significant. It may cause enough misalignment of the inversions of the sample material of interest and the calibration lead sample to have a serious effect on the determination of $R(\theta)$. From (35) and (41) it can easily be shown that the shift distortion as a function of incidence angle is of the form

$$|\Delta\theta| = \cot\theta\,\Delta v/v \tag{42}$$

which shows that the most serious errors occur at low angles of incidence.

The problem of determining the true transform $P^2(\theta)R(\theta)$ from a finite segment $V'(z)$ of $V(z)$ is a common one in Fourier analysis and spectral estimation. Various techniques exist in the literature for extrapolating $V'(z)$ so that a more accurate determination of $P^2(\theta)R(\theta)$ can be made. Since $P^2(\theta)R(\theta)$ is a bandlimited function, the maximum spatial frequency being limited by the angular extent of the pupil function, $V(z)$ is analytic in the entire $z$ axis [17]. In principle, an iterative algorithm proposed by Papoulis [18] can be used to improve the accuracy of the estimation of $P^2(\theta)R(\theta)$.

## Conclusion

We have demonstrated that the reflectance function of a liquid–solid interface can be determined by inverting the corresponding complex $V(z)$ data from an acoustic microscope. This inversion technique represents a more complete approach to material characterization than previous $V(z)$-related work. The phase velocities of the various propagating modes in the solid medium can be obtained directly from the reflectance function. The effect of material loss can also be observed and quantified. Moreover, this measurement technique provides a means of gauging imaging performance of focused systems by directly measuring the pupil function illumination. In addition, there are useful practical applications in the area of thin-film characterization, and many interesting possibilities exist for more complex structures, such as multi-layered films. The nonparaxial formulation of the $V(z)$ integral is important in that it lays a sound theoretical foundation for the inversion measurement technique. The excellent agreement between the theoretically and experimentally obtained reflectance functions further supports the validity of the nonparaxial theory.

Although this work has been carried out and discussed in the context of acoustic microscopy, the validity and applicability of many of the underlying concepts extend to optical microscopy as well. Provided one can accurately measure the optical phase, which is not trivial but certainly realizable [22], the inversion algorithm described here can be used to obtain the optical reflectance function from the corresponding complex optical $V(z)$ function.

## Acknowledgment

The authors would like to thank Dr. Simon Bennett and Dr. Ian Smith for the stimulating discussions related to this work.

## Appendix

Auld and Kino [19]–[21], by using the reciprocity theorem, were able to determine the normalized reflected signal or reflection coefficient $s_{11}$ from an object. The theory

for longitudinal waves in a liquid can be stated in the form

$$s_{11} = \frac{j\omega \int (u^i p - u p^i)\, n\, dS}{4P} \tag{A1}$$

where the integral is taken over the surface of the object, $u$ is the displacement, and $p$ is the pressure fields associated with an incident wave of temporal frequency $\omega$. Here $\exp(j\omega t)$ time dependence is assumed. The superscript $i$ denotes the incident or transmitted wave when the object is not present, and the unsuperscripted terms denote the total field at the obstacle. The parameter $P$ is the power exciting the transducer for a given incident signal $u^i$, $p^i$.

The total fields can be written in the form

$$u = u^i + u^r \tag{A2}$$

$$p = p^i + p^r \tag{A3}$$

where the superscript $r$ denotes the waves reflected from the object. Substituting (A2) and (A3) into (A1) yields

$$s_{11} = \frac{j\omega \int (u^i p^r - u^r p^i) n\, dS}{4P}. \tag{A4}$$

If the object is a semi-infinite plane normal to the $z$ direction, $s_{11}$ can be written in the normalized form

$$V(z) = \frac{\int (u_z^i p^r - u_z^r p^i)\, dS}{2 \int u_z^i p^{i*}\, dS} \tag{A5}$$

where the asterisk denotes the complex conjugate. Finally it is convenient to write the pressure in terms of the potential. For a liquid with $u = \nabla\phi$, it can be shown that $p = j\omega\rho\phi$. Hence it follows that

$$V(z) = \frac{\int (u_z^i \phi^r - u_z^r \phi^i)\, dS}{2 \int u_z^i \phi^{i*}\, dS} \tag{A6}$$

Note that for a perfect plane reflector located at the focal plane $z = 0$ of a lens, $\phi^r = \phi^i = \phi^{i*}$, and $u_z^r = -u_z^i$; therefore $V(z) = 1$.

## References


[1] A. Atalar, "An angular spectrum approach to contrast in reflection acoustic microscopy," *J. Appl. Phys.*, vol. 49, pp. 5130-5139, Oct. 1978.

[2] H. K. Wickramasinghe, "Contrast and imaging performance in the scanning acoustic microscope," *J. Appl. Phys.*, vol. 50, pp. 644-668, Feb. 1979.

[3] R. D. Weglein, "Metrology and imaging in the acoustic microscope," in *Scanned Image Microscopy*, E. A. Ash, Ed. London: Academic, 1980.

[4] J. Kushibiki and N. Chubachi, "Material characterization by line-focus-beam acoustic microscopy," *IEEE Trans. Sonics Ultrason.*, vol. SU-32, pp. 189-212, Mar. 1985.

[5] W. Parmon and H. L. Bertoni, "Ray interpretation of the material signature in the acoustic microscope," *Elect. Lett.*, vol. 15, pp. 684-686, 1979.

[6] A. Atalar, "A physical model for acoustic material signature," *J. Appl. Phys.*, vol. 50, pp. 8237-8239, 1979.

[7] J. Kushibiki, A. Ohkubo, and N. Chubachi, "Acoustic anisotropy detection of materials by acoustic microscope using line-focus-beam," in *Proc. IEEE Ultrason. Symp.*, 1981, pp. 552-556.

[8] J. Kushibiki, K. Horii, and N. Chubachi, "FFT velocity measurement of multiple leaky waves by line-focus-beam acoustic microscope," in *Proc. IEEE Ultrason. Symp.*, 1983, pp. 637-640.

[9] H. L. Bertoni, "Ray-optical evaluation of $V(z)$ in the reflection acoustic microscope," *IEEE Trans. Sonics Ultrason.*, vol. SU-31, no. 2, pp. 105-116, Mar. 1984.

[10] P. M. Morse and H. Feshbach, *Method of Theoretical Physics*. New York: McGraw-Hill, 1953.

[11] I. J. Cox, D. K. Hamilton, and C. J. R. Sheppard, "Observation of optical signature of materials," *Appl. Phys. Lett.*, vol. 41, no. 7, pp. 604-606 Oct. 1982.

[12] J. A. Hildebrand, K. Liang, and S. D. Bennett, "Fourier-transform approach to material characterization with the acoustic microscope," *J. Appl. Phys.*, vol. 54, no. 12, pp. 7016-7019, Dec. 1983.

[13] K. Liang, S. D. Bennett, B. T. Khuri-Yakub, and G. S. Kino, "Precision phase measurements with the acoustic microscope," *IEEE Trans. Sonics Ultrason.*, vol. SU-32, pp. 000-000, Mar. 1985.

[14] G. Mott, "Reflection and refraction coefficients at a fluid-solid interface," *J. Acoust. Soc. Am.*, vol. 50, no. 3, pp. 819-829, 1971.

[15] F. L. Becker and R. L. Richardson, "Influence of material properties or Rayleigh critical-angle reflectivity," *J. Acoust. Soc. Am.*, vol. 51, no. 5, pp. 1609-1617, 1972.

[16] T. Bourbie, "Effects of attenuation on reflections," Ph.D. Thesis, Stanford University, Stanford, CA, April 1982.

[17] N. I. Akhiezer, *Theory of Approximations*. New York: Ungar, 1956.

[18] A. Papoulis, "A new algorithm in spectral analysis and band-limited extrapolation," *IEEE Trans. Circuits and Systems*, vol. CAS-22, no. 9, pp. 735-742 Sept. 1975.

[19] G. S. Kino and B. A. Auld, "Reciprocity theories for flaw analysis," ARPA/AFML annual review of progress in quantitative NDE, Cornell University, Ithaca, NY, 1977.

[20] B. A. Auld, "General electromechanical reciprocity relations applied to the calculation of elastic-wave scattering coefficients," in *Wave Motion*, vol. 1. Amsterdam: North-Holland, 1979, pp. 3-10.

[21] G. S. Kino, "The application of reciprocity theory to scattering of acoustic waves by flaws," *J. Appl. Phys.*, vol. 49, no. 6, pp. 3190-3199, June 1978.

[22] R. L. Jungerman, P. C. D. Hobbs, and G. S. Kino, "Phase sensitive scanning optical microscope," *Appl. Phys. Lett.*, vol. 45, no. 8, pp. 846-848, Oct. 1984.

[23] J. Fraser and C. Desilets, Precision Acoustic Devices, Inc., Palo Alto, CA, private communication.


**Kenneth K. Liang** was born in Hong Kong in 1954. He received the B.S.E.E. degree from the University of Minnesota, Minneapolis, MN, in 1976.

He is currently finishing his doctoral dissertation in electrical engineering at Stanford University, Stanford, CA. His current interests are in the application of acoustic imaging techniques to nondestructive testing.

**Gordon S. Kino** (S'52-A'54-SM'63-F'66) was born in Melbourne, Australia on June 15, 1928. He received the B.Sc. and M.Sc. in mathematics at London University, England, and the Ph.D. in electrical engineering at Stanford University, Stanford, CA.

He is Professor of Electrical Engineering and Professor by Courtesy of Applied Physics at Stanford University. He has worked on microwave tubes, electron guns, plasmas, and the Gunn effect. His current interests are in microwave acoustics and acoustic and fiber optic techniques for medical instrumentation, nondestructive testing, and signal processing.

Dr. Kino was a Guggenheim Fellow in 1967 and is a Fellow of the American Physical Society, AAAS, and a member of the National Academy of Engineering.

**Butrus T. Khuri-Yakub** (S'70-M'76) was born in Beirut, Lebanon. He received the B.S. degree in 1970 from the American University of Beirut, the M.S. degree in 1972 from Dartmouth College, Hanover, NH, and the Ph.D. degree in 1975 from Stanford University, Stanford, CA, all in electrical engineering.

He joined the research staff at the E. L. Ginzton Laboratory of Stanford University in 1976 as a Research Associate. He was promoted to a Senior Research Associate in 1978, and to a Professor of Electrical Engineering (research) in 1982. His current research interests include thin-film deposition, surface acoustic wave devices, bulk-wave transducers and arrays, nondestructive evaluation of structural materials, acoustic imaging, and photo-acoustic interactions.

Dr. Khuri-Yakub is a member of the Acoustical Society of America.

# Precise Phase Measurements with the Acoustic Microscope

KENNETH K. LIANG, SIMON D. BENNETT, MEMBER, IEEE, BUTRUS T. KHURI-YAKUB, MEMBER, IEEE, GORDON S. KINO, FELLOW, IEEE

*Abstract*—**The measurement and the use of phase in acoustic microscopy are discussed. It is demonstrated that in many applications phase can be used to provide sensitivity and information unparalleled by amplitude-only measurement methods. A technique capable of high-accuracy measurement of the phase of short RF acoustic pulses is described. The power of this phase measurement technique is illustrated in a number of applications. Surface material property measurements such as the Rayleigh-wave velocity and the inversion of the complex $V(z)$ to obtain the reflectance function of a liquid-solid interface are considered. Surface topography mapping based on phase measurement is examined. A Fourier transform approach for precision determination of linewidths comparable to the resolution spot size is also presented.**

## I. Introduction

THE SCANNING acoustic microscope is a high-resolution imaging system in which, unlike conventional optical microscopes, it is relatively straightforward to measure the phase of the return signal. With only a few exceptions [1]-[3], attention has centered only on the use of intensity information. In some of the main areas of application of the acoustic microscope, the phase of the received signal plays an important role. For example, in the so-called $V(z)$ measurements [4]-[7], the amplitude of the received signal $V(z)$ as a function of the separation between the lens and the substrate exhibits periodic peaks and nulls. This phenomenon is due to the beating between a specularly reflected signal from the substrate and a delayed leaky Rayleigh-wave signal, which reemits to the lens while propagating along the surface of the substrate. The phase difference between these two signal components is therefore of great importance, and in fact it controls the contrast of reflectional images. In addition, it has been shown that the independent measurement of phase and amplitude can be very useful in the determination of the elastic constants of tissue [8], [9]. However, little effort has been made to extract the phase of the return signal separately.

One reason for the reluctance to make use of the phase is that it is not generally trivial to measure the phase of a high-frequency tone burst with sufficient accuracy. We will describe here an approach that is relatively easy to implement and capable of yielding high-precision phase data, even from very short tone bursts. The details of the phase measurement technique will be published elsewhere, and we will concentrate here on some of the applications of the system to acoustic microscopy.

There are many motivations for making measurements of this type. Firstly, they offer a direct indication of material properties as in the measurement of Rayleigh-wave velocity. Also, the results of the phase measurement can be used to infer the width and the height of surface features. Finally, the combination of amplitude and phase measurements can be used in the reconstruction processes in which complete information about the interaction between acoustic field and material is required, as in the inversion of $V(z)$ data to find the reflection coefficient as a function of angle [10].

## II. Phase Measurement Scheme

### A. Acoustic Lens Configuration

In making precise phase measurements that are related to physical properties, it is generally important to ensure that the reference signal, against which the phase of the probing signal is to be compared, and the probe itself share as many of the instrumental and environmental phase disturbances as possible. In other words, precise measurements are best done in an interferometer, where the two arms are closely matched.

In this work we have made use of two acoustic measurement configurations that largely satisfy this general condition. The first (Fig. 1(a)) is reminiscent of the defocused condition used in $V(z)$ measurements, except that here a fixed separation between the lens and the sample surface is maintained. Two components of the acoustic field returned to the lens contribute most significantly to the output signal: the on-axis specular reflection of the longitudinal wave in the water ($L$ in Fig. 1a); and the off-axis rays ($R$), which satisfy the condition $v_w/v_R = \sin\theta_R$ for the conversion of longitudinal waves with velocity $v_w$ in the water to leaky Rayleigh waves with velocity $v_R$ on the surface of the sample [4], [5].

These two signals, $L$ and $R$, differ slightly in path length in water but otherwise experience much the same environ-

Manuscript received September 1984, revised December 1984. This work was supported by the Air Force Office of Scientific Research under Contract F49620-79-C-0217.

K. Liang, B. T. Khuri-Yakub, and G. S. Kino are with the Edward L. Ginzton Laboratory, W. W. Hansen Laboratories of Physics, Stanford University, Stanford, California 94305, USA.

S. D. Bennett is with Datasonics Corp., 911 Del Avenue, Campbell, CA 95008, USA.

0018-9537/85/0300-0266$01.00 

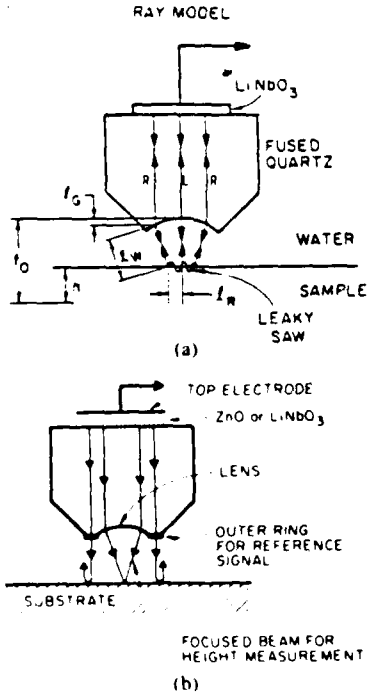


Fig. 1. Acoustic lens configurations. (a) Rayleigh-wave velocity perturbation measurement. (b) Topography mapping.

mental disturbances. However, the Rayleigh-wave component acquires substantial phase delay at the surface of the specimen, hence the effective path length for the *R* signal is longer than that of the specular reflection. Indeed in our experiments we use the different arrival time of these two return signals to facilitate their separation and subsequent phase comparison. The excitation signal is two to three cycles in duration, and the defocus distance is sufficient that there is no temporal overlap of the signals. It is clear that changes in the Rayleigh-wave velocity as a function of position along the surface of the specimen may be sensed in this way. By combining a high-accuracy phase measurement scheme with a suitably extended Rayleigh-wave path, remarkably sensitive measurements can be made.

The second configuration that concerns us is illustrated in Fig. 1(b). In this case the lens is positioned so that its focus is at the surface of the specimen or slightly above it so that no Rayleigh wave of importance is excited. A reference path is provided by an annular beam that propagates through the flat outer periphery of the lens. By exciting the lens with a short pulse, and once again using time discrimination to separate the signals from the two different paths, an interferometer is formed. Now small local changes in the surface topography result in large changes in the phase of the focused beam relative to the phase of the large diameter reference beam.

In both measurement configurations it is apparent that the signals of interest arrive at different times, and this would ordinarily make phase comparison impossible. However, the electronic system described in the next section essentially reconstructs two phase-coherent continuous signals that are directly related to the amplitudes and phases of the two time-distinct return signals.

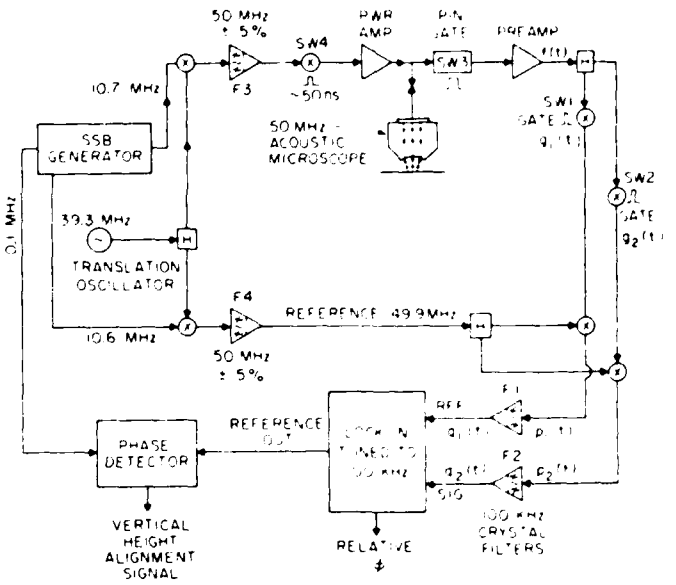


Fig. 2. Schematic for the phase measurement system.

The first configuration is also used where the signal of interest is the transducer output voltage, when the system is operated in the $V(z)$ mode. In this case the exciting signal has a much longer duration so that the return signals ($L$ and $R$) overlap and interfere at the transducer even for large defocus distances. The idea here is to measure both the amplitude and the phase of the signal relative to some reference as a function of the axial separation $z$ between the acoustic lens and the specimen. The resulting complex $V(z)$ can be inverted [10] to obtain the angular dependence of the reflectance of the liquid–specimen interface. From the reflectance function, various material property parameters can readily be extracted.

In the experiments described here, a center frequency of 50 MHz was used with an acoustic transducer having a bandwidth of 20 percent. The lens material was fused quartz and had a radius of curvature of 3.2 mm, giving a focal length in water of 4.24 mm. The opening aperture of the lens was 5.0 mm in diameter, corresponding to a maximum half angle of 36° or an f-number of 0.85.

Providing the same fractional bandwidth can be maintained, there should be little difficulty in applying the same techniques to a system operating at much higher frequency, perhaps up to 2 GHz. Beyond that frequency, limitations in the electronic-switching components presently available may present difficulties.

### *B. Electronics*

The essential elements of the phase measurement electronics are shown schematically in Fig. 2. The system will be described in detail in a forthcoming paper [18], where various sources of error and an analysis of the ultimate performance are discussed. A more general review of the concepts will suffice here.

The basic scheme involves signal recovery by synchronous detection and subsequent phase measurement with a lock-in amplifier. The key component (Fig. 2) in the signal source is the single sideband generator (SSB) with synchronous outputs at 100 kHz, 10.6 MHz, and 10.7 MHz. The 10.7-MHz output is in fact the upper sideband of the product of the 100 kHz and 10.6-MHz signals. The lower sideband at 10.5 MHz is suppressed by at least 50 dB using a standard FM radio system IF filter. The translation oscillator shifts the operating frequency up to the desired center frequency of the acoustic system, which is 50 MHz in this case. A reference signal at 49.9 MHz is also generated. Again the lower sideband components of the product signals have to be removed. At this point however the filtering requirements are not as stringent as in the SSB generator and tunable bandpass filters (F3 and F4) with five-percent bandwidth are adequate, since the sidebands are now widely separated. This signal generation scheme is flexible in that the operating frequency is tunable over a fairly wide range, which is limited in this case to 100 MHz by the bandpass filters. For much higher frequency of operation, filters with greater selectivity would be needed or, alternatively, successive stages of heterodyning could be used with filtering at each stage to step up incrementally to the desired operating frequency.

As illustrated in Fig. 2 with a 50-MHz acoustic microscope, the 50-MHz continuous wave (CW) signal is timegated to produce a short tone burst that excites the acoustic transducer. Switch SW3 is used as a time gate to pass the low-level acoustic return signals of interest and to block high-level extraneous ones, which may damage the preamplifier. The acoustic return signals are time-separated RF pulses, and they are electronically separated through timegating into two channels as shown. Each of the resulting signals is mixed with the 49.9 MHz reference signal, and the product is narrow-band filtered to extract the 100-kHz component.

It can be shown [18] that the 100-kHz signals are essentially low-frequency CW replicas of the pulse modulated RF acoustic signals, bearing identical phase and amplitude information. With a biphase lock-in amplifier tuned to 100 KHz, one can readily measure the phase difference between the two signals and also the amplitude of the signal being fed to the "signal" channel of the lock-in, if it is required. Phase sensitivity is basically limited by the lock-in amplifier because the problem of system noise can in most cases be overcome by increasing the integration time in the lock-in output stage. This effectively reduces the system noise bandwidth, but it also includes the obvious disadvantage of longer data acquisition time. Good-quality lock-in amplifiers routinely have phase resolution of the order of 0.1°, which corresponds to an overall system phase sensitivity of 1/3600 of a wavelength.

In velocity perturbation measurements the measured phase is dependent on the distance between the lens and the specimen. This distance changes with the sample surface topography and is susceptible to thermal drift as well, thus introducing phase error into the measurement. To minimize this error, a feedback mechanism is employed to keep the lens-to-specimen spacing constant. The acoustic lens is mounted on a piezoelectric (PZT) stack so that its vertical position can be adjusted continuously by an electronic control signal. The acoustic on-axis reflection pulse, whose phase is a direct measure of the lens to sample distance, is applied to the reference channel of the lock-in amplifier as shown in Fig. 2. The reference channel generates a 100-kHz constant-amplitude phase-locked replica of the reference input, which is then compared with the 100-kHz output of the SSB generator to produce the control signal for the PZT stack. The acoustic lens automatically tracks the surface topography of the sample during scanning to ensure that the measured phase change is due to material property variation alone. This feedback mechanism is also used effectively in such modes of operation as topography measurement to compensate for thermal effects.

## III. Applications

The power of this measurement scheme is illustrated in the following with a number of examples. We will consider both material property measurements, such as Rayleigh-wave velocity and complex reflectivity, and surface topography measurements.

### *A. Velocity Perturbation Measurements*

In this section we will specifically deal with the perturbation to the Rayleigh-wave propagation velocity as a result of material property change and also the presence of surface residual stress.

*1) Velocity Perturbation Due to Thin-Film Overlay:* The sample in this example is a multiple-thickness indium film deposited on glass. The thicknesses are 240 Å and 620 Å, respectively. The objective was to measure the perturbation of the Rayleigh-wave velocity caused by the indium film. A line scan over the surface of the sample (Fig. 3) exhibits phase changes of 7° and 11° for the 240-Å and 380-Å step changes in film thickness. The spatial resolution of the system is defined by the Rayleigh-wave path length on the substrate and is determined to be about 0.8 mm from the step transition width in the line scan. It can be calculated from first order perturbation theory [11] that the velocity perturbation due to the indium film is 0.18 percent and 0.46 percent for the 240-Å and 620-Å layers, respectively. Based on these estimated parameters, one would expect phase changes of 7.6° and 12° for the 240-Å and 380-Å step transitions. Hence there is fairly good agreement between the experimentally obtained and theoretically predicted phase changes. It should also be noted that in the line scan, the small phase variations in the supposedly flat regions of the indium film are real and repeatable. The fluctuations are less than 0.5° and are due to nonuniformity in the thickness of the indium film. Since the phase sensitivity of the system is limited by the lock-in amplifier to 0.1°, this measurement technique can po-

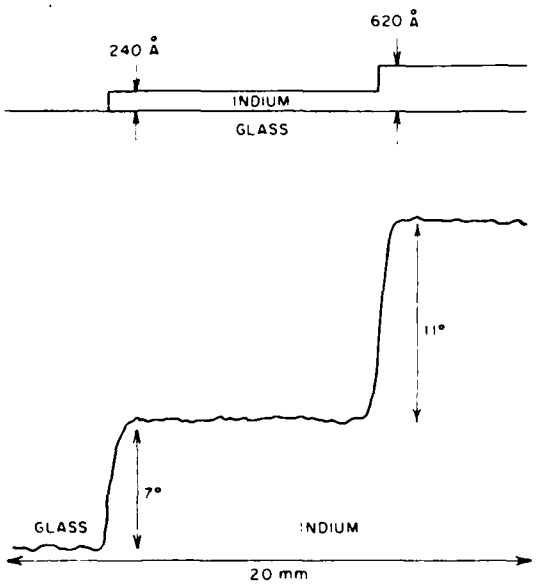


Fig. 3. Measurement of velocity perturbation due to indium film on glass.

tentially detect velocity perturbations on the order of one part in $10^5$.

*2) Residual Stress Measurement:* In nondestructive testing, knowledge of the surface residual stress distribution in a component plays an important role in the prediction of failure modes. One way of characterizing residual stress is by measuring the acoustic wave propagation velocity, which varies linearly with the local stress [12]. With the measurement configuration shown in Fig. 1(a) the measured change in the relative phase between the $L$ and $R$ signal pulses as the lens is scanned can be shown to be directly proportional to the residual stress on the object surface [13].

The sample used in the experiment is a glass disk of two inches in diameter that was heated and then thermally quenched with air jets to introduce a radial distribution of residual stress. Fig. 4(b) shows the radial variation of the measured phase perturbation. For comparison a destructive test was carried out on a similar sample to determine the actual residual stress distribution. A Vicker's indenter was used at a prescribed load to produce median cracks at different points on the glass disk. By measuring the crack lengths, the residual stress as a function of radial distance was calculated [14]. The result of the destructive test is shown in Fig. 4(a). The variation of the principal stresses are essentially the same, with the radial and tangential components tracking each other to within 20 MPa. Since the phase measurement is omnidirectional in that a spherical lens was used to launch Rayleigh waves propagating in all directions along the surface, the resulting phase perturbation is a measure of the sum of the principal stresses. Comparison of Figs. 4(a) and 4(b) shows that there is fairly good corroboration between the phase perturbation curve and the actual residual stress distribution. From these results we empirically deduce that 40 MPa of stress, which is the change from the center of the sample to the

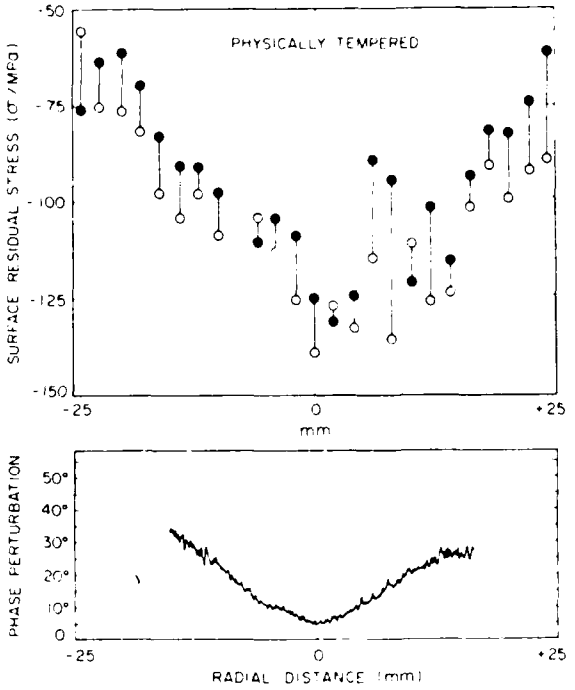


Fig. 4. Residual stress measurements on the surface of a tempered glass disk. (a) Variation of radial (open symbols) and tangential stresses (closed symbols) across a diameter of the glass disk estimated from indentation fracture tests. (b) Radial variation of measured phase perturbation.

limit of the line scan, corresponds to a phase variation of 30°.

### *B. Surface Topography Measurements*

We have used the acoustic microscope in the measurement configuration shown in Fig. 1(b) as a high-resolution noncontacting profilometer [13], [15]. Besides being able to make use of phase profile to map the depth variation, we can also determine with high precision the transverse profile of surface features in special cases. Of particular interest in this regard is the measurement of the widths of long rectangular strips, which is a matter of great concern in the fabrication of semiconductor components. We will show here both experimentally and theoretically the advantages of utilizing phase to determine the linewidth. We will also introduce here a Fourier transform technique for linewidth measurement in cases where the strip width is comparable to the spot size.

*1) Depth Profiling:* Topography images of metallized stripe patterns on a fused-silica substrate are shown in Figs. 5(a), 5(b), and 5(d). The patterns have progressively finer pitches and the linewidths are 250, 125, and 62.5 $\mu$m, respectively. The metallization is gold with a thickness of about 3000 Å. The gold stripes show up as bright areas in the images. At 50 MHz, with an f-number of 0.85 and a uniformly excited aperture, the Rayleigh resolution of the acoustic lens is $1.13\ F\lambda = 0.96\ \lambda$ or 29 $\mu$m, while the 3-dB resolution is $0.64\ F\lambda = 0.54\ \lambda$ or 16 $\mu$m. The 62.5-$\mu$m line image in Fig. 5(d) is clearly resolved, as would be expected. The amplitude image of the 125-$\mu$m stripes is shown in Fig. 5(c) for comparison. There is vir-

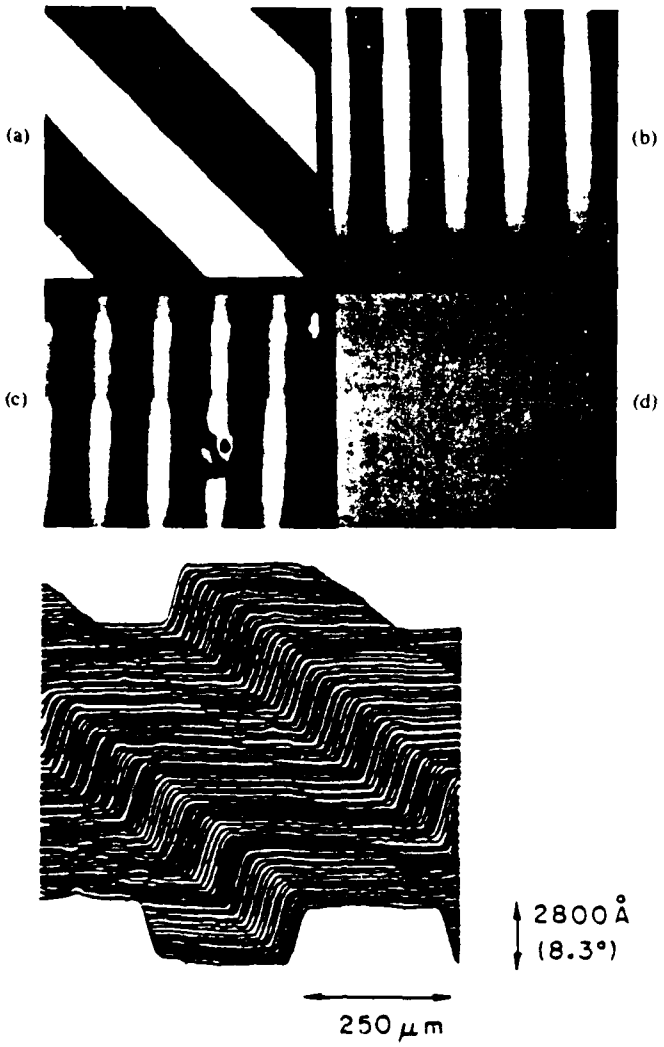


Fig. 5. Topography images of striped metallization patterns on a fused quartz substrate. The metallization is gold and the thickness is about 3000 Å. (a) Phase image of 250-μm lines. (b) Phase image of 125-μm lines. (c) Amplitude image of 125-μm lines. (d) Phase image of 62.5-μm lines. (e) Perspective plot of the measured topography map of the 250-μm line pattern.

tually no contrast to suggest the presence of a striped pattern, clearly illustrating that phase is a far more sensitive means of gauging distances. The measured phase difference between the surface of the metallization and the surface of the fused-silica substrate is 8.3°, which corresponds to a film thickness of 2800 Å after taking into account the angular dependence of the complex reflectance function and the effect of focusing.

We will show here that, based on theoretical considerations, indeed the phase rather than the magnitude of the acoustic microscope output $V(x)$ is a more sensitive measure of the depth profile. Consider the simple case of a rectangular strip of width $w$ on a substrate of identical material. Assume that the reflection coefficient $\Gamma_0$ of the surface is real. Then the spatial response of the strip structure is given by

$$R(x) = \Gamma_0 + \Gamma_0 (e^{j\phi} - 1) \text{ rect } (x/w) \tag{1}$$

where $\phi$ is the phase change due to the thickness of the strip. Let the response of the imaging system to a line source be $h(x)$. Furthermore, suppose that the lens is uniformly illuminated in the back focal plane and the lens is aberration-free so that $h(x)$ is real. The acoustic microscope output is therefore given by

$$V(x) = R(x) * h(x) \tag{2}$$

or

$$V(x) = \Gamma_0 K + \Gamma_0 (e^{j\phi} - 1)\, s(x) \tag{3}$$

where

$$s(x) = h(x) * \text{rect } (x/w) \tag{4}$$

and

$$K = \int_{-\infty}^{+\infty} h(x)\, dx.$$

The first term on the right-hand side of (3) corresponds to the constant background reflection from the substrate, and the second term corresponds to the additional spatially varying contribution that is due to the strip. It can easily be shown that for a thin strip where $\phi << 1$, to second order in $\phi$, the magnitude and the phase of $V(x)$ are given respectively by the relations

$$V_{\text{mag}}(x) = \Gamma_0 K + \frac{\Gamma_0\, s(x)}{2} [s(x) - K]\, \phi^2 \tag{5}$$

and

$$V_{\text{phase}}(x) = \frac{\phi}{K} s(x). \tag{6}$$

The $V_{\text{phase}}(x)$ is directly proportional to $\phi$, whereas the spatially varying part of $V_{\text{mag}}(x)$ depends on $\phi$ to the second order. Thus for thin strips, phase is a much more sensitive measure of the depth profile.

*2) Linewidth Measurement:* A major advantage of scanned confocal imaging systems such as ours is that because the point spread function is always positive and falls off rapidly at large distances, there is hardly any ripple in the amplitude of the step response [16], [17]. A similar smooth transition in the phase of the step response can also be observed in the perspective plot shown in Fig. 5(e). For the purpose of comparison, we have carried out a numerical analysis for the step phase responses of different imaging configurations. For small step heights, or equivalently small phase changes, the normalized phase step response is of the form

$$\beta(x) = \int_x^{\infty} g(r) \cos^{-1} (x/r)\, r\, dr \tag{7}$$

where $x$ is the distance between the center of the beam and the step, and $g(r)$ is the point response function of the imaging system. It is assumed that regions on either side of the step are of equal reflectivity. The step response function is plotted in normalized form in Fig. 6 for two

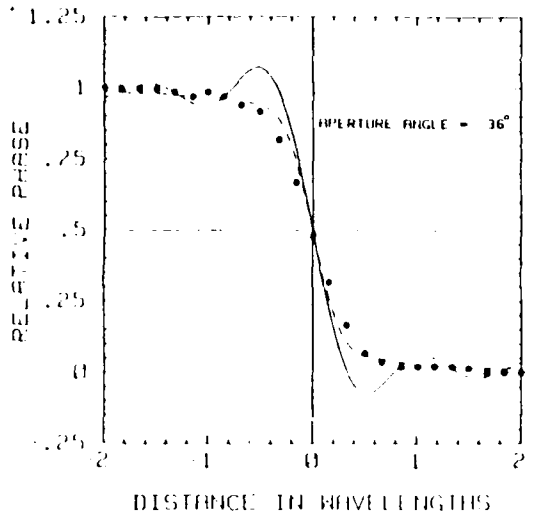


Fig. 6. Step phase response of a normal phase interference microscope (solid curve) and a confocal imaging system (theory in dashed curve, experimental result in closed circles).

ifferent cases. The solid curve corresponds to $g(r) = \text{jinc}(2r \sin\theta/\lambda)$, which is the point response of a normal phase interference microscope where the illumination is a plane wave. Here $\theta$ is the maximum half angle of the objective lens; $\lambda$ is the wavelength of the illumination; and jinc $(x)$ is defined as $2J_1(\pi x)/\pi x$. Note that in this case $g(r)$ reverses in sign and its corresponding step phase response does not change monotonically with distance. The dashed curve corresponds to $g(r) = \text{jinc}^2(2r \sin\theta/\lambda)$, the point response of a confocal system. The confocal response shows a distinct lack of ripples. The experimentally measured step phase response is also plotted in closed circles showing close agreement with theory. In both imaging configurations, the 50-percent threshold of the phase profile demarcates the location of the edge. It is obvious, however, that the smooth transition of the confocal step phase response enables a straightforward and unambiguous determination of not only the strip thickness but also the strip width.

The 50-percent threshold criterion used to locate the edges of a strip for estimating the linewidth is a valid one for wide strips. For strip widths comparble to the spot size of the imaging system, the step responses of the two edges are in close proximity and tend to interfere with each other, making the establishment of a general criterion for locating the strip edges difficult. We will describe here a Fourier transform method that circumvents these difficulties.

Applying Fourier transform to (6) and using the definition of $s(x)$ in (4), the spatial frequency spectrum of $V_{\text{phase}}(f_x)$ is given by

$$\tilde{V}_{\text{phase}}(f_x) = \frac{\Phi}{K} H(f_x) \cdot w \,\text{sinc}(wf_x) \tag{8}$$

where $H(f_x)$ is the Fourier transform of $h(x)$. The term with the sinc function corresponds to the Fourier transform of the spatial variation of the strip and its zeroes are located at

$$f_x = n/w, \qquad n = 1, 2, 3, \cdots. \tag{9}$$

The term $H(f_x)$ represents the angular spectral response of the imaging system. For a confocal system $|H(f_x)|$ is maximum at $f_x = 0$ and generally falls off monotonically, until it becomes zero at the upper cutoff frequency of

$$f_{x\max} = 1/(F\lambda)$$

where $F$ is the f-number of the lens, and $\lambda$ is the wavelength of the illumination [16], [17]. Hence the zeroes of $\tilde{V}_{\text{phase}}(f_x)$ are those of the strip response within the passband of the imaging system. As long as

$$w > F\lambda \tag{10}$$

the strip width $w$ can be determined using (8) from the locations of the zeroes of $\tilde{V}_{\text{phase}}(f_x)$. In our case $F = 0.85$, so in principle we can determine linewidths as small as 0.85 $\lambda$ or 25 $\mu$m at 50 MHz in water.

The merit of this Fourier-transform technique lies in its simplicity. Given *a priori* knowledge of the strip geometry, one does not need to know the exact nature of imaging system. The mere location of the zeroes for the spectral response of the object suffices for the accurate determination of the linewidth.

Fig. 7 illustrates the experimental $|\tilde{V}_{\text{phase}}(f_x)|$ for $w$ = 76 $\mu$m, 43 $\mu$m, and 33 $\mu$m, respectively. The strips are 5000-Å-thick gold lines on a fused-quartz substrate. The acoustic microscope operates at 50 MHz ($\lambda$ = 30 $\mu$m) with $F$ = 0.85, and the acoustic beam is focused on the surface of the fused-quartz substrate. The $|\tilde{V}_{\text{phase}}(f_x)|$ is plotted on a log scale. The weighting due to the imaging system response $|H(f_x)|$ all the way out to the resolution limit is very much in evidence. The linewidths estimated from the position of the first zero of $\tilde{V}_{\text{phase}}(f_x)$ are 76.3, 43.5, and 31.4 $\mu$m, respectively. They agree very well with the optically measured widths. The minor discrepancies are mainly due to the nonuniformity in the widths of the gold lines.

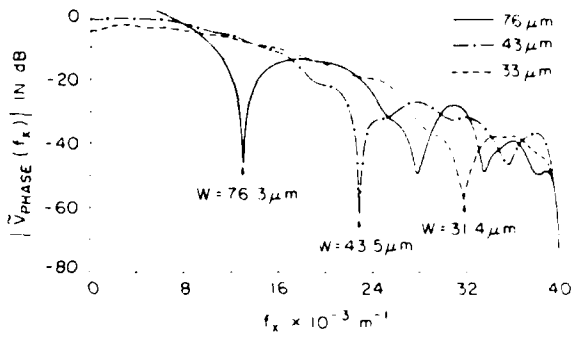


Fig. 7. Spectral responses of 5000-Å-thick gold lines on a fused-quartz substrate. The nominal linewidths are 76 $\mu$m, 43 $\mu$m, and 33 $\mu$m, respectively.

In addition, this Fourier transform approach is essentially insensitive to defocusing. It is obvious from (8) that

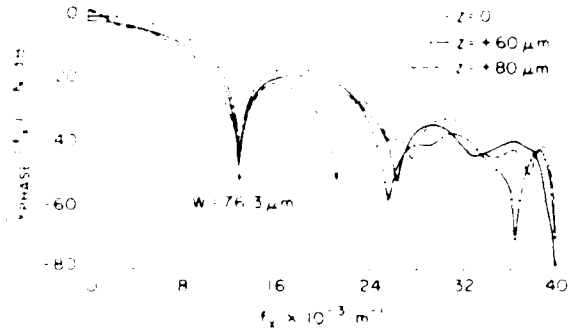


Fig. 8. Spectral responses of 2000-Å thick 76-μm wide chrome line on a fused quartz substrate at various defocusing distances: $z = 0$ μm, $+60$ μm, and $+80$ μm, respectively.

defocusing only changes the spectral response of the imaging system $H(f_x)$ slightly and does not introduce any new zeroes to nor does it affect the zeroes of $|\tilde{V}_{\text{phase}}(f_x)|$. Fig. 8 shows the experimental $|\tilde{V}_{\text{phase}}(f_x)|$ for a 2000-Å-thick and 76-μm-wide chrome line on fused quartz at various defocusing distances. The focus was located on the substrate, and 60 μm and 80 μm above the substrate, respectively. The locations of the first zero in all three cases are essentially coincident, giving a width estimate of 76.3 μm.

*3) Independent Measurement of Velocity Perturbation and Topography:* In conventional acoustic micrographs, surface topography and material property both contribute to contrast in the image, and their respective effects are generally indistinguishable from one another. With the topography tracking mechanism described in Section II-2 built into our phase measurement system, surface topography and material property change can essentially be obtained independent of each other.

Fig. 9(a) is the topographic line scan of an aluminum film step on glass with a nominal thickness of 5000 Å. The initial and trailing slow phase changes are due to the large spatial extent of the reference signal as it traverses the step, whereas the abrupt phase change is due to the focused beam as it crosses the step. Fig. 9(b) is the same profile on an expanded scale. The phase change caused by the step is 11.25°, which corresponds to a thickness of 4688 Å. With a limiting phase resolution of 0.1°, the ultimate height sensitivity of the system is about 50 Å.

Fig. 9(c) shows a velocity perturbation scan of the same sample. The phase change measured is 7.75°, corresponding to a velocity perturbation of 0.25 percent, which is in fair agreement with the theoretically calculated value of 0.21 percent.

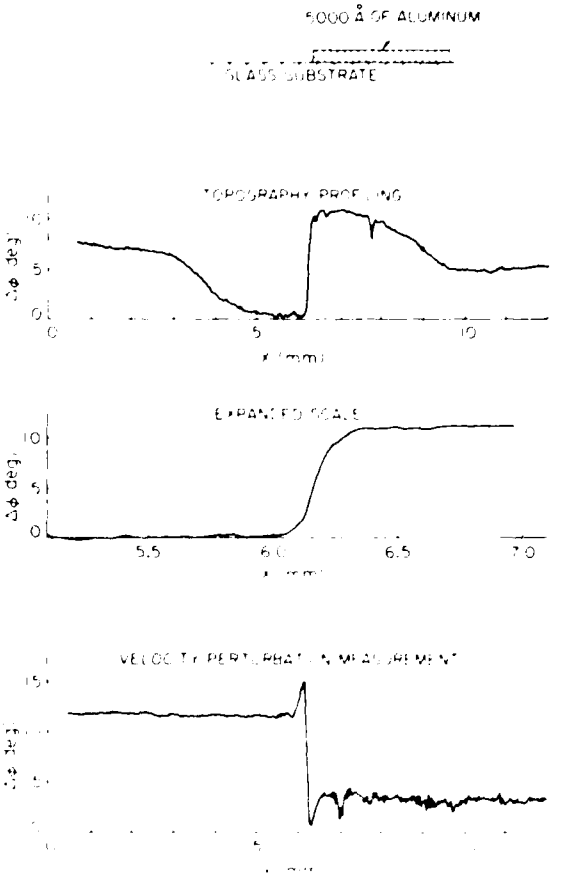


Fig. 9. Independent measurements of velocity perturbation and topography profile due to 5000-Å aluminum film step. (a) Topography profile scan. (b) Topography profile scan on an expanded scale. (c) Velocity perturbation scan.

### C. Reflectance by Inversion of Complex $V(z)$

It has been demonstrated that the reflectance function at a liquid–solid interface can be obtained by inverting the corresponding complex $V(z)$ data [10]. The principle motivation behind this endeavor is that one can obtain much more useful material property information from the reflectance function than the usual and rather limited treatment of measuring the periodicity of the nulls in the $V(z)$ curve to determine only the Rayleigh-wave velocity. The solid curves in Fig. 10 show the magnitude and the phase of the theoretical reflectance function of a water–fused-silica interface. The reflectance function contains information on the longitudinal and shear critical angles, and thus the velocities of propagation of the respective modes in fused silica. Also, the Rayleigh critical angle corresponds to the point at which the phase is $\pi$ radians in the region, where the phase curve undergoes a rapid $2\pi$ radian change.

It can be shown that the relation between $V(z)$ and the reflectance function $R(\theta)$ is essentially one of Fourier transformation [10]. The inversion formula is given by

$$R(t) \quad \frac{\mathfrak{F}\{V(u)\exp[j\pi u \sin^2(\alpha/2)]\}}{[U_i'(t)]^2 P^2(t)[1 - 2t\sin^2(\alpha/2)]} \qquad (11)$$

where

$$u = \frac{4z\sin^2(\alpha/2)}{\lambda}$$

and

$$t \quad \sin^2(\theta/2)$$
$$\sin^2(\alpha/2)$$

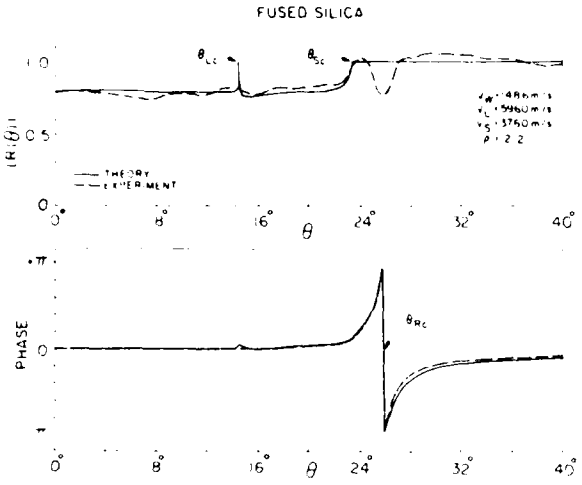


Fig. 10. Theoretical and experimental reflectance function for a water-fused-quartz interface obtained by inversion of the corresponding complex $V(z)$.

The $\alpha$ is the maximum half angle of the lens; $\theta$ is the incident angle with respect to the liquid-solid interface; and $\lambda$ is the wavelength of the acoustic wave in the liquid medium. In addition, $U_i^+$ is the back focal plane illumination, and $P$ is the pupil function of the lens. Generally these two lens parameters are not known, but $[U_i^+]^2 P^2$ in the denominator of (11) can be calibrated by measuring the $V(z)$ for a material whose reflectance function has uniform amplitude and phase over the range of angular spectral components excited by the acoustic lens.

The $V(z)$ measurements were conducted at 10 MHz. A water-lead interface, in which the reflectance function is uniform in magnitude and phase out to $\theta = 40°$, was used to calibrate the $[U_i^+]^2 P^2$ term. The experimental reflectance function of fused silica, obtained from the inversion procedure, is superposed on Fig. 10 in dashed lines. There is good agreement between theory and experiment in both magnitude and phase. The measured shear critical angle at $\theta = 23.5°$ and the Rayleigh critical angle at $\theta = 25.85°$ compare extremely well with theoretical values.

## IV. Conclusion

We have demonstrated that phase information is a useful asset in acoustic microscopy. Phase can be used to provide sensitivity and information in surface material characterization unparalleled by amplitude-only measurement techniques. Most of the concepts described in this work have complete generality and can readily be used in other applications. In fact, many ideas presented in this work have been applied to a new scanning optical microscope [19] developed by Jungerman and Kino for surface topography measurement. In the optical case both the amplitude and the phase of the reflected beam can be measured as in the acoustic microscope. Preliminary results from the scanning optical microscope give further confirmation of most of the concepts put forth in this paper.

## References

[1] H. K. Wickramasinghe and M. Hall, "Phase imaging with the scanning acoustic microscope," *Electron. Lett.*, vol. 12, pp. 637–638, Nov. 1976.

[2] C. C. Lee, C. S. Tsai, and X. Cheng, "Complete characterization of thin-and thick-film materials using wideband reflection acoustic microscopy," *IEEE Trans. Sonics Ultrason.*, vol. SU-32, no. 2, pp. 248–258, Mar. 1985.

[3] S. D. Bennett and E. A. Ash, "Differential imaging with the acoustic microscope," *IEEE Trans. Sonics Ultrason.*, vol. SU-28, pp. 59–69, 1981.

[4] A. Atalar, "An angular spectrum approach to contrast in reflection acoustic microscopy," *J. Appl. Phys.*, vol. 49, pp. 5130–5139, Oct. 1978.

[5] H. K. Wickramasinghe, "Contrast and imaging performance in the scanning acoustic microscope," *J. Appl. Phys.*, vol. 50, pp. 664–668, Feb. 1979.

[6] R. D. Weglein, "Metrology and imaging in the acoustic microscope," in *Scanned Image Microscopy*, E. A. Ash, Ed. London: Academic, 1980.

[7] J. Kushibiki and N. Chubachi, "Material characterization by line-focus-beam acoustic microscope," *IEEE Trans. Sonics Ultrason.*, vol. SU-32, no. 2, pp. 189–212, Mar. 1985.

[8] J. R. Smith, D. A. Sinclair, and H. K. Wickramasinghe, "Acoustic microscopy of elastic constants," in *Proc. 1980 IEEE Symp. Sonics Ultrason.*, Boston, MA, Oct. 1980.

[9] D. A. Sinclair and J. R. Smith, "Tissue characterization using acoustic microscopy," in *Acoustic Imaging*, vol. 12, E. A. Ash and C. R. Hill, Ed. New York: Plenum, 1982.

[10] J. A. Hildebrand, K. Liang, S. D. Bennett, "Fourier transform approach to material characterization with the acoustic microscope," *J. Appl. Phys.*, vol. 54, no. 12, pp. 7016–7019, Dec. 1983.

[11] B. A. Auld, *Acoustic Fields and Waves in Solids*, vol. 2. New York: John Wiley & Sons, 1973, p. 278.

[12] D. Husson and G. S. Kino, "A perturbation theory for acoustoelastic effects," *J. Appl. Phys.*, vol. 53, p. 7250, Nov. 1982.

[13] K. Liang, S. D. Bennett, B. T. Khuri-Yakub, and G. S. Kino, "Precision measurement of Rayleigh wave velocity perturbation," in "DARPA-AF Review of Progress in Quantitative NDE," La Jolla, CA, Aug. 1982.

[14] D. B. Marshall and B. R. Lawn, "Measurement of nonuniform distribution of residual stresses in tempered glass disks," *Glass Tech.*, vol. 19, no. 3, June 1978.

[15] K. Liang, S. D. Bennett, B. T. Khuri-Yakub, and G. S. Kino, "Precision measurement of Rayleigh wave velocity perturbation," *Appl. Phys. Lett.*, vol. 41, no. 12, pp. 1124–1126, 1982.

[16] R. A. Lemons, "Acoustic microscope by mechanical scanning," Ph.D. Thesis, Stanford University, Stanford, CA, 1975.

[17] J. W. Goodman, *Introduction to Fourier Optics*. New York: McGraw-Hill, 1968.

[18] K. Liang, S. D. Bennett, and G. S. Kino, "Precision phase measurement for acoustic microscopy," to be submitted to *Rev. Sci. Inst.*

[19] R. L. Jungerman, P. C. D. Hobbs, and G. S. Kino, "Phase sensitive scanning optical microscope," submitted to *Appl. Phys. Lett.*, vol. 45, pp. 846–848, Oct. 1984.

**Kenneth K. Liang**, for a photograph and biography please see page 223 of the March 1985 issue of this TRANSACTIONS.

**Simon D. Bennett** (S'73–M'78), for a photograph and biography please see page 131 of this TRANSACTIONS.

**Butrus T. Khuri-Yakub**, (S'70–M'76), for a photograph and biography please see page 224 of the March 1985 issue of this TRANSACTIONS.

**Gordon S. Kino** (S'52–A'54–SM'63–F'69), for a photograph and biography please see page 224 of the March 1985 issue of this TRANSACTIONS.

# Characterization of surface defects using a pulsed acoustic laser probe

R. L. Jungerman, B. T. Khuri-Yakub, and G. S. Kino
*Edward L. Ginzton Laboratory, W. W. Hansen Laboratories of Physics, Stanford University, Stanford, California 94305*

(Received 13 May 1983; accepted for publication 13 September 1983)

A pulsed acoustic laser probe is used to measure vertical acoustic displacements in the near field of surface defects. A method of optically determining acoustic reflection coefficients in the time domain is presented. The spatial variation of acoustic displacements over a slot is modeled with a static theory. This theory estimates a depth of 230 $\mu$m for a 250-$\mu$m-deep slot. A near field image of a fatigue crack demonstrates an application of the technique.

PACS numbers: 46.30.Rc, 42.80.Mv, 43.40.Cw, 68.25. + j

In the field of nondestructive evaluation of materials, there is considerable interest in determining the location and size of surface defects. Defects, such as fatigue cracks in the surface of a metal sample, can determine the failure of the specimen under load. Acoustic surface waves have been used to locate and size defects using time domain reflectometry.[1,2] In this method, a piezoelectric transducer is used to excite a short acoustic pulse. The reflected echo from a discontinuity is then detected with a transducer. The amplitude of the reflected signal gives information on the cross-sectional area of the defect while the time delay of the echo determines the defect position. In analyzing the acoustic reflection coefficient, allowance must be made for the transmitting and receiving transducer insertion loss, acoustic attenuation, and diffraction. In addition, it is often difficult to locate the defect precisely, knowing only the time delay of the echo. In this letter we will present a method of optically measuring acoustic displacements in the near field of a defect using a laser probe. Two methods of characterizing defects will be discussed. The first is a variation of time domain reflectometry, using the laser probe to detect the incident and reflected acoustic pulses. Calibration is greatly simplified using this method. The second approach involves measuring the spatial variation of the vertical acoustic displacement over a defect to determine its dimensions.

The laser probe used in these experiments is a variation of the all-fiber-optic interferometer described in earlier work.[3,4] The probe compensates for optical reflectance changes encountered while scanning rough surfaces, making it applicable to surface finishes produced by most common manufacturing processes.[5] We have adapted the sensor to operate in a pulsed mode in which the piezoelectric transducer is excited with a short tone burst. The laser diode is gated to turn on after a time delay which allows for the acoustic transit time between the transducer and the location where the optical measurement is made. The acoustic transducer and laser are gated with duty cycles in the range 10:1–100:1.

An optical measurement of the acoustic reflection coefficient can be made by positioning the laser probe spot in the near field of a defect and between the acoustic transducer and the defect. As the time delay between the acoustic tone burst and laser gating signal is increased, the incident acoustic amplitude, and then the reflected amplitude, are measured. The same laser probe is used to measure the incident and reflected pulses so no transducer insertion loss correction is required. Also, since the measurement is made close to the defect, diffraction and attenuation corrections are not significant.

Figure 1 demonstrates this technique for a 375-$\mu$m-deep slot in an aluminum sample using a 5-$\mu$s acoustic tone burst at 1.5 MHz. The measurement is made 1 cm from the slot. The experimental reflection coefficient is $0.32 \pm 0.06$, as compared to a theoretical prediction of 0.23.[1] The principal error comes from ringing in the transducer which causes the fluctuating baseline and makes a precise estimation of the peak amplitudes difficult.

The second method of characterizing defects is to fix the laser gating time delay so that the incident acoustic pulse is centered over the defect when the laser is switched on. The laser spot is scanned across the defect to measure the spatial variation of the normal displacement of the surface due to the acoustic wave. Steele has developed a theory[6] to calculate the vertical surface displacements near a rectangular slot in the surface of a half-space when loaded statically in tension. The displacement curves are a function of the slot depth $t$, the width $e$, and the applied longitudinal stress $\sigma$. By operat-

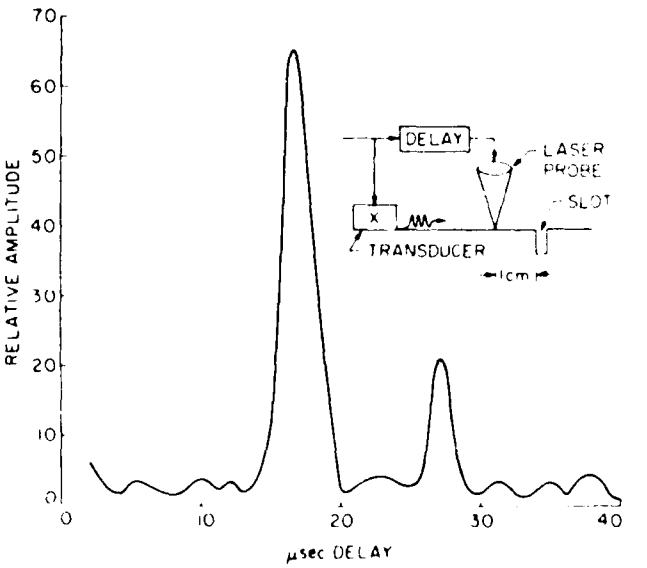


FIG. 1. Time domain measurement of the acoustic reflection coefficient from a slot in an aluminum sample. The time delay between the acoustic tone burst and the laser gating signal is used to separate the incident and reflected pulses. The reflection coefficient is $0.32 \pm 0.06$. The acoustic frequency is 1.5 MHz and the slot depth is 375 $\mu$m.

 0003-6951/84/040392-02$01.00  

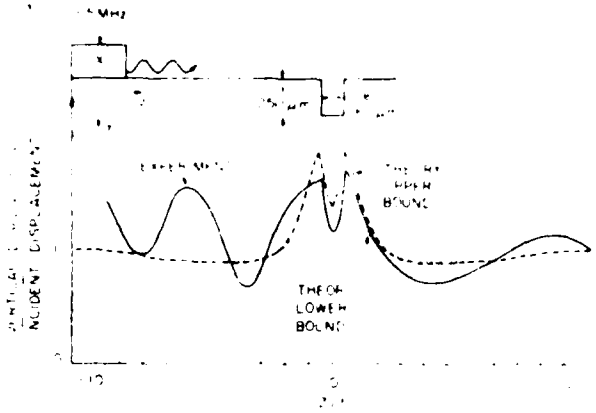

FIG. 2. Vertical displacements in the near field of a slot with 1.5-MHz Rayleigh wave excitation. The static theory provides an upper bound (dashed) and a lower bound (dots) for the vertical displacements. The half-width $d$ is used to predict a slot depth of 230 $\mu$m. The true slot depth is 250 $\mu$m.

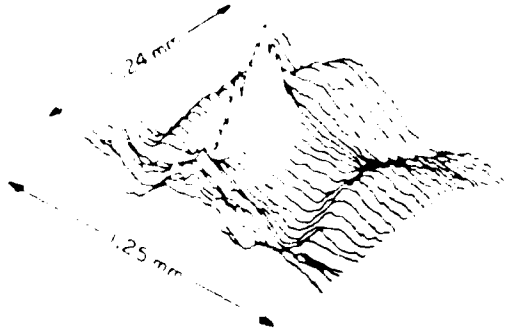

FIG. 3. Acoustic displacement image of a fatigue crack in an aluminum sample. Vertical displacement amplitude is plotted as a function of position. The defect is 450 $\mu$m long, half-penny shaped, and 200 $\mu$m deep. The 5.5-MHz acoustic transducer is to the left.

ing in the long wavelength regime (the Rayleigh wavelength is much larger than the defect dimensions), we can apply this theory to a slot under the influence of a Rayleigh wave stress field. Near the surface, the shear stress is zero and the longitudinal stress along the direction of propagation $z$ decays exponentially with depth $y$.[7] The value of $\sigma_{zz}(y)$ averaged over the depth of the slot is used in the theory. This value of $\bar{\sigma}_{zz}$ can be normalized in terms of the incident Rayleigh wave amplitude at the surface $u_y$.

Figure 2 presents the theoretical and experimental curves in aluminum for a long slot, 160 $\mu$m wide and 250 $\mu$m deep. The 1.5-MHz acoustic transducer is to the left. Standing waves due to reflection from the slot are evident to the left of the slot. These dynamic effects are not treated by the static theory. In the bottom of the slot and to the right, the properties of the transmitted wave agree well with theory, particularly near the slot. Further to the right, bulk waves from the bottom of the slot give rise to other dynamic effects. Taking the average displacement far to the right of the slot as the incident displacement $u_y$ (the transmission coefficient is nearly unity), the theoretical curves are normalized by the calculated constant:

$$t\,\bar{\sigma}_{zz}/Eu_y = 0.33,$$

where $E$ is Young's modulus. Note the vertical component of the incident Rayleigh wave displacement, which makes it possible to normalize the curves, also raises the curves by a constant offset. The static theory[6] provides upper and lower bounds on the displacements. The experimental points lie between these curves for the transmitted field near the slot. Perhaps more importantly, the distance $d$ between the center of the slot and the point where the amplitude equals the unperturbed Rayleigh wave amplitude can be calculated. From this distance, a crack depth of 230 $\mu$m is estimated, close to the true value of 250 $\mu$m. The calculated value of the half-width $d$ does not depend on the acoustic frequency or on the use of the upper or lower theoretical bound.

The previous experimental results have been for long saw cuts, which are almost as wide as they are deep. A potential application of the probe to the characterization of a fatigue crack in an aluminum sample is shown in Fig. 3. The defect is 450 $\mu$m long, half-penny shaped, and approximately 200 $\mu$m deep. At an acoustic frequency of 5.5 MHz, the acoustic image of vertical displacement amplitude as a function of position clearly determines the location and length of the crack. Precisely estimating the crack depth from the acoustic displacement profile is complicated by the nonuniform depth and finite length of the defect which necessitate a three-dimensional analysis.

In conclusion, we have demonstrated a pulsed acoustic laser probe which makes it possible to measure acoustic reflection coefficients and vertical displacements in the near field of surface defects. A static theory is applied to the near field amplitude distribution to accurately estimate the depth of a slot. Finally, practical application of the probe to fatigue cracks is illustrated.

The authors would like to thank R. Stearns, C. R. Steele, and S. H. Yoo for their helpful discussions. M. Resch provided the fatigue crack specimen. This work was supported by the Ames Research Laboratory for the Defense Advanced Research Projects Agency under contract No. SC-81-009 and the NSF-MRL Program through the Center for Materials Research at Stanford University.

[1] M. Hirao and H. Fukuoka, J. Acoust. Soc. Am. 72, 602 (1982).
[2] J. D. Achenbach, A. K. Gautersen, and D. A. Mendelsohn, IEEE Trans. Son. Ultrason. SU-27, 124 (1980).
[3] J. F. Bowers, Appl. Phys. Lett. 41, 231 (1982).
[4] J. F. Bowers, R. T. Jungerman, B. T. Khuri-Yakub, and G. S. Kino, J. Lightwave Tech. LT-1, 429 (1983).
[5] R. T. Jungerman, B. T. Khuri-Yakub, and G. S. Kino, J. Acoust. Soc. Am. 73, 1838 (1983).
[6] C. R. Steele and S. H. Yoo, Appl. Phys. Lett. (to be published).
[7] I. A. Viktorov, *Rayleigh and Lamb Waves* (Plenum, New York, 1967), p. 4.

# APPLICATION OF ACOUSTIC MICROSCOPY TO SURFACE PROFILING AND MATERIAL CHARACTERIZATION

by

K. Liang, G. S. Kino, and B. T. Khuri-Yakub

Preprint
G. L. Report No. 3798
November 1984

1984 IEEE Ultrasonics Symposium
Dallas, Texas

AFOSR 84-0063

Edward L. Ginzton Laboratory
W. W. Hansen Laboratories of Physics
Stanford University
Stanford, California 94305

# APPLICATION OF ACOUSTIC MICROSCOPY TO SURFACE PROFILING AND MATERIAL CHARACTERIZATION

K. Liang, G. S. Kino and B. T. Khuri-Yakub

Edward L. Ginzton Laboratory, Stanford University
Stanford, California 94305

## ABSTRACT

A Fourier transform technique is used to quantitatively determine transverse widths of surface features. This technique is based on a generalized theory which takes into account the angular dependence of the reflectance of the surface being examined and the effect of defocusing. This measurement technique is essentially independent of material properties and the focusing of the lens. Experimental results on linewidths as small as one wavelength will be presented.

New experimental results in material characterization by the inversion of $V(z)$ to obtain the complex reflectance function $R(\theta)$ of a liquid/solid interface will also be presented. The result of an alternative derivation of the integral relation between $V(z)$ and $R(\theta)$, which does not require any paraxial assumption, will be given.

## I. Line Width Measurement

Images obtained with a scanning reflection acoustic microscope contain quantitative information about the vertical depths and transverse widths of the object surface features.[1] It will be shown in this paper that in some special cases, the transverse dimensions can be determined with high precision. A particularly simple case, yet one of much practical interest, is the measurement of the widths of long strips with rectangular cross-sections. We will introduce a Fourier transform approach to the line width measurement problem. The theoretical foundation of this work is based on a complete modeling of the spatial response of a confocal imaging system to a rectangular strip, which takes account of the angular dependence of the reflectivity of the object. This Fourier technique will be shown to be especially useful in determining strip widths comparable to the focal spot size. Experiments conducted at 60 MHz will be presented to demonstrate the basic principle.

### 1. Theory

Consider a thin strip deposited on a semi-infinite substrate of a dissimilar material, as shown in Fig. 1. Suppose the strip is infinite in the $y$ direction, has width $D$ and is centered at

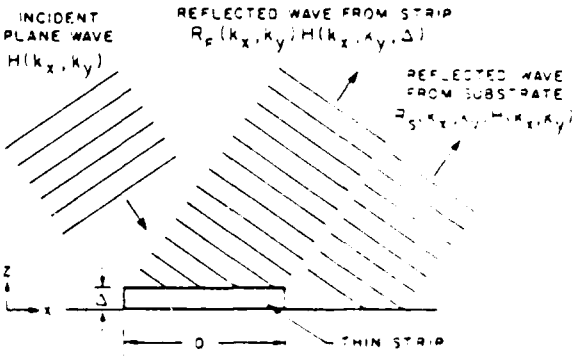


Fig. 1. Kirchoff approximation to the acoustic field reflected from a thin strip deposited on a substrate.

$x_0 = x_s$. The thickness $\Delta$ of the strip is assumed to be very much smaller than $\lambda$, so that the only significant reflection is from the top surface of the strip. It can be shown that the acoustic microscope output voltage as a function of the strip position $x_s$ has the form

$$v_0(x_s) = \int_{-\infty}^{+\infty} \mathrm{rect}\left(\frac{x_0 - x_s}{D}\right) h''(x_0)\, dx_0 + \int_{-\infty}^{+\infty} (h * m_S) h\, dx_0\, dy_0 \qquad (1)$$

where

$$h''(x_0) = \int_{-\infty}^{+\infty} [(h' * m_F) h' - (h * m_S) h]\, dy_0$$

$$m_F(x_0, y_0) = \mathcal{F}^{-1} R_F(f_x, f_y) \qquad (2)$$

$$m_S(x_0, y_0) = \mathcal{F}^{-1} R_S(f_x, f_y)$$

and $h'(x_0,y_0)$ and $h(x_0,y_0)$ are respectively the acoustic microscope point spread functions (PSF) at the top of the strip and at the surface of the substrate, and $R_F$ and $R_S$ are respectively the reflectance functions of the water/film interface and the water/substrate interface.

The second term of $v_0(x_s)$ in Eq. (1) is unimportant because it is a constant due to the background reflection from the substrate. The first term, however, explicitly shows a convolution relation between $\mathrm{rect}(x_0/D)$, which describes the geometric width of the strip, and an effective line spread function $h''(x_0)$ that takes into account the different reflectances and vertical heights of the surfaces of the strip and the substrate. In other words, $v_0(x_s)$ is a blurred image profile of the actual strip. $v_0(x_s)$ can be a very complicated waveform, particularly when the strip width $D$ is comparable to the spot size of the focused acoustic beam, or the beam is defocused. This makes it difficult to accurately determine $D$ by locating the edges of the strip. This difficulty with the spatial domain response is the primary motivation for the Fourier spectrum approach to the line width measurement problem described below.

Since a convolution in the spatial domain corresponds to a multiplication in the spatial frequency domain, one obtains from Eq. (1)

$$V_0(f_x) = D\,\mathrm{sinc}(Df_x)\,H''(f_x) + B\,\delta(f_x) \qquad (3)$$

where $H''(f_x)$ is the Fourier transform of $h''(x_0)$. $V_0(f_x)$ vanishes at the zeros of the "sinc" function, which occur at

$$Df_x = n \qquad n = \pm 1, \pm 2, \ldots \qquad (4)$$

It follows that

$$D = n/f_{x,\mathrm{zero}} \qquad (5)$$

It can be shown that for a confocal system, $|H''(f_x)|$ has low pass characteristics with a upper cutoff frequency of

$$f_{x,\max} = 1/(F\lambda) \qquad (6)$$

where $F$ is the f-number of the lens. $H''(f_x)$ is in general non-zero within the passband, and is identically zero above the cutoff frequency. Thus the zeros of $V_0(f_x)$ for $0 < f_x < f_{x,\max}$ are exactly those of the 'sinc' response of the strip. As long as the zeros fall inside the passband, i.e.

$$D > F\lambda \qquad (7)$$

the strip width can be determined from Eq. (5). For instance, if $F = 0.85\lambda$, one can, in principle, resolve line widths as small as $0.85\lambda$.

The power of this Fourier transform technique lies in its simplicity. Given a priori knowledge of the strip geometry, one only has to be aware of some general properties, but does not need to know the exact details, of the imaging system response. The mere location of the zeros of the overall spectral response suffices for the accurate determination of the line width.

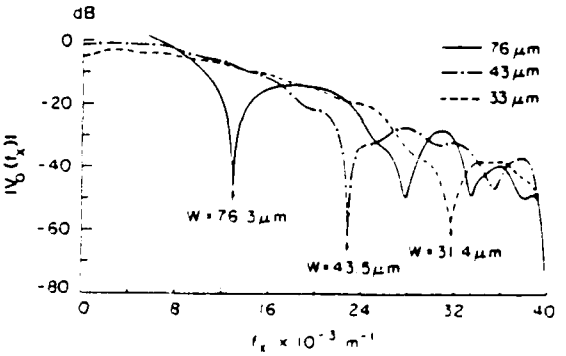


Fig. 2. Fourier spectra of the acoustic microscope spatial response to 5000 Å thick gold lines on fused silica from 1 to 2.5 wavelengths wide.

## 2. Experimental Results

Fig. 2 illustrates the experimental $|V_0(f_x)|$ for 5000 Å thick gold lines deposited on a fused quartz substrate. The optically-measured widths are $D$ = 76, 43, and 33 μm, respectively. The acoustic microscope operates at 50 MHz ($\lambda$ = 30 μm) with a f/0.85 lens, and the acoustic beam is focused on the surface of the fused quartz substrate. The line widths estimated from the position of the first zero of $V_0(f_x)$ agree very well with the optically-determined widths. The minor discrepancies are mainly due to the nonuniformity in the widths of the gold lines.

In addition, it is important to realize that this Fourier transform approach is essentially insensitive to defocusing. It is obvious from Eq. (3) that defocusing only changes the effective spectral response $H''(f_x)$ slightly, and does not introduce any new zeros to, nor does it affect the zeros of, $|V_0(f_x)|$. Fig. 3 shows the experimental $|V_0(f_x)|$ for a 2000 Å thick and 76 μm wide chrome line on fused quartz at various defocusing distances. The focus was in turn located on, and at 60 μm and 80 μm above, the substrate. The locations of the first zero in all three cases are essentially coincident, giving a width estimate of 76.3 μm.

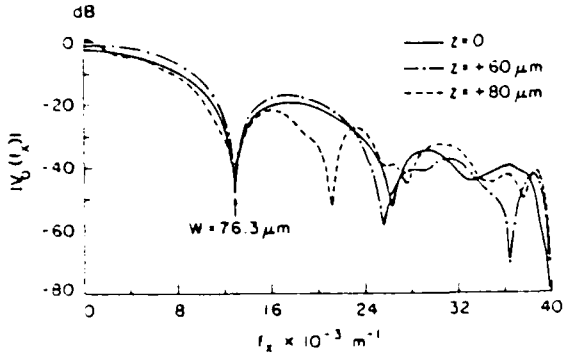


Fig. 3. Fourier spectra of the acoustic microscope spatial response to a 2000 Å thick and 76 μm wide chrome line on fused silica at different defocusing distances.

## II. Material Characterization by Inversion of V(z)

The Fourier transform relation between $V(z)$ and the the reflectance $R(\theta)$ of a liquid/solid interface has been derived and demonstrated experimentally in acoustic microscopy.[2,3] However, the $V(z)$ integral on which the derivation of the Fourier transform relation is based is formulated using the paraxial approximation, and is therefore not valid for acoustic lenses with a large angle of convergence. An alternative hybrid formulation, which combines elements of angular spectrum and ray optics formalisms, has been carried out and the result is given below. It should be noted that no paraxial assumption is necessary for its development. New results for different materials obtained by inverting complex $V(z)$ data acquired with a special spherical transducer operating at 10 MHz are also shown.

### 1. Theory

The special case of a focused spherical transducer radiating directly into water with no buffer medium is considered as shown in Fig. 4. The practical significance of this acoustic lens configuration will be explained later. The special transducer geometry simplifies the derivation, and yet the final solution has general validity for any acoustic lens configuration which produces a converging spherical wave.

It can be shown that the voltage response $V(z')$ of the focused transducer is given by

$$V(z') = \int P^2(k_z)\, R(k_z) \exp(-jk_z z')\, dk_z \qquad (8)$$

where $z' = 2z$, $k_z$ is the wave vector component in the $z$ direction, $P(k_z)$ is the pupil function of the lens, and $R(k_z)$ is the reflectance function of the liquid/solid interface. Eq. (8) shows that $V(z')$ and $P^2(k_z)R(k_z)$ form a Fourier transform pair. The inversion to obtain $R(k_z)$ is given by

$$R(k_z) = \begin{cases} \dfrac{\mathcal{F}^{-1}(V(z'))}{P^2(k_z)} & P(k_z) \neq 0 \\ 0 & P(k_z) = 0 \end{cases} \qquad (9)$$

In general, $P(k_z)$ is not known a priori. However, $P^2(k_z)$ can conveniently be calibrated by inverting the $V(z)$ for a liquid/solid interface whose reflectance has uniform magnitude and phase over the angular extent of the lens pupil function. The water/lead boundary is one such example, and the magnitude and phase of the reflectance is essentially flat from 0° to 40° incidence.

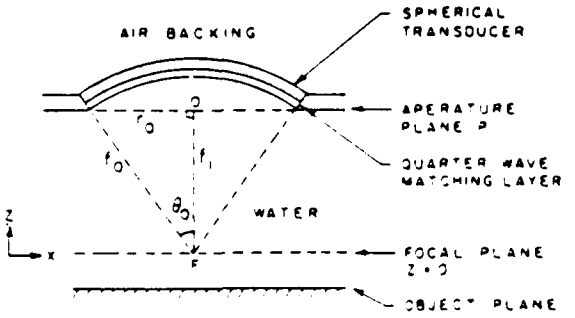


Fig. 4. Special focused transducer used for the $V(z)$ measurements.

This inversion approach to material characterization is different in that it requires the measurement of $V(z)$ in both amplitude and phase, whereas previous work[4,5] utilized only the amplitude or intensity of $V(z)$. It is generally not trivial to conduct high-accuracy phase measurements in acoustic microscopy. We have developed a phase measurement system[1] that makes possible the precision acquisition of phase data and the experimental demonstration of the inversion technique.

### 2. Experimental Results

A special acoustic lens is used for the $V(z)$ measurement. The acoustic transducer is a piezoelectric element in the form of a spherical shell with air backing and a quarter-wave matching layer on the front face. The transducer generates a converging spherical wave directly into water. This acoustic lens configuration is advantageous for the $V(z)$ measurement for the following reason. The elimination of the buffer rod removes the systematic noise due to reverberations inside the buffer rod. This type of noise tends to overlap in time with the reflected signal from the object. With the present lens construction, the acoustic lens can be translated over a wide range of $z$ to collect $V(z)$ data in an essentially noise-free environment.

The spherical transducer has a focal length of 16 mm, f/0.7 aperture, and is operated at 10.17 MHz. Many practical considerations go into this

particular choice of operating frequency range. The inversion of the $V(z)$ is most conveniently carried out for a lossless liquid medium. The loss in water is essentially negligible at 10 MHz, and so satisfies this requirement. Moreover, the wavelength in water of about 150 μm is sufficiently large to render any irregularity and instability in the vertical translation mechanism insignificant. For the same reason, the measurement is less subject to error as a result of surface finish imperfections in the sample.

Figure 5 shows the reflectance function of a water/fused silica interface obtained by inverting the corresponding $V(z)$ and then normalizing out $P^2(k_z)$ of the transducer. The theoretical reflectance is also shown in the solid curve for comparison. There is good general agreement between theory and experiment in both magnitude and phase. The experimental shear critical angle at $\theta = 23.5°$ and the Rayleigh critical angle at $\theta = 25.85°$ compare extremely well with theory. The longitudinal critical angle is not reproduced in the experimental result due to the angular resolution degradation problem caused by the spatial truncation of the $V(z)$ data.[2]

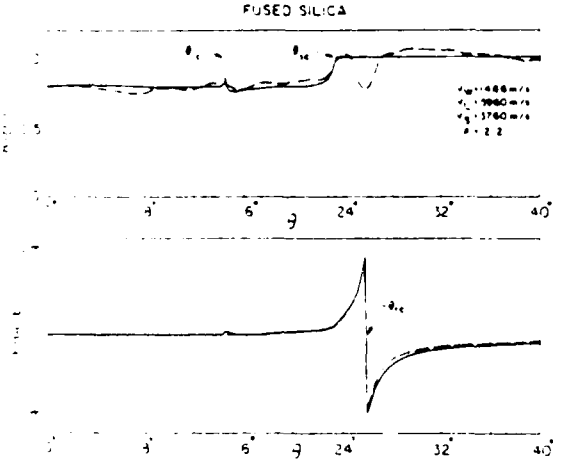


Fig. 5. Comparison of the theoretical (solid line) and experimental (dashed line) reflectance functions for a water/fused silica interface.

Figure 6 is the reflectance function for aluminum. Again, the fit between theory and experiment is very good. The longitudinal and shear critical angles show up clearly in the experimental result in this case. The Rayleigh critical angle is located at $\theta = 30.86°$, which gives a phase velocity of 2897 m/s for the leaky surface acoustic wave.

Figure 7 shows the reflectance function for Plexiglas or Lucite, a low acoustic velocity material with high loss. This example illustrates how loss in materials can be determined. The longitudinal critical angle is located at $\theta = 32.7°$

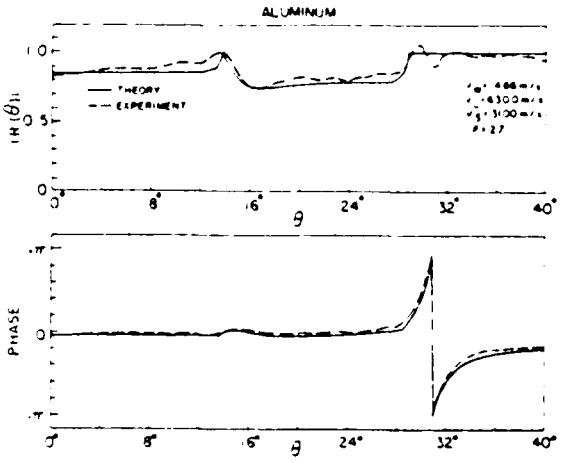


Fig. 6. Comparison of the theoretical and experimental reflectance functions for a water/aluminum interface.

which corresponds to a longitudinal wave velocity of 2750 m/s. The magnitude of the reflectance peaks at 0.7 rather than 1, as would be the case for a lossless substrate. The amount of diminution of the peak level depends on the loss for the longitudinal mode. The theoretical curve is fitted to the experimental one by varying the longitudinal loss factor $Q_L$. $Q_L$ is found to be about 50, which translates into an attenuation coefficient of 232 nepers/m, or 20 dB/cm at 10 MHz, which agrees well with other published values.[5]

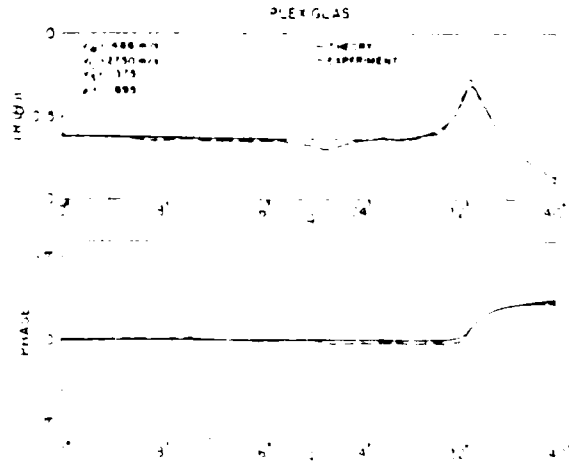


Fig. 7. Comparison of the theoretical and experimental reflectance functions for a water/Plexiglas interface.

## III. Conclusion

We have developed and demonstrated a Fourier transform approach to line-width measurement. For the case of strips with rectangular cross-sections,

the technique is essentially insensitive to the characteristics of the imaging system. Line widths comparable to a wavelength can be determined accurately with this method.

New results on material characterization by the inversion of complex V(z) data have also been shown. The result of a more general and non-paraxial formulation of the V(z) integral is given. This inversion technique represents a more complete approach to material characterization than previous V(z) related work. Phase velocities of various propagating modes in the material of interest can be determined from the reflectance function. In addition, acoustic losses can also be estimated.

## IV. Acknowledgment

The authors would like to thank Drs. Simon Bennett and Ian Smith for the stimulating discussions related to this work. This work was supported by the Air Force Office of Scientific Research under Contract No. AFOSR-84-0063.

## References

1. K. Liang, S. D. Bennett, B. T. Khuri-Yakub, and G. S. Kino, "Precision Phase Measurements in the Acoustic Microscope," IEEE Trans. Sonics & Ultrasonics, to be published (1984).
2. K. Liang, B. T. Khuri-Yakub, and G. S. Kino, "Material Characterization by the Inversion of V(z)," IEEE Trans. Sonics & Ultrasonics, to be published (1984).
3. J. A. Hildebrand, K. Liang, and S. D. Bennett, "Fourier Transform Approach to Material Characterization with the Acoustic Microscope," J. Appl. Phys. 54 (12), 7016-9 (December 1983).
4. J. Kushibiki and N. Chubachi, "Material Characterization by Line-Focus-Beam Acoustic Microscopy," IEEE Trans. Sonics & Ultrasonics, to be published (1984).
5. R. D. Weglein, "Metrology and Imaging in the Acoustic Microscope," in Scanned Image Microscopy, edited by E. A. Ash, Academic Press, London (1980).
6. T. Bourbie, "Effects of Attenuation on Reflections," Ph.D. Thesis, Stanford University (April 1982).

Invited Paper

# MEASUREMENT TECHNIQUES FOR ELECTRONIC DEVICES

by

Gordon S. Kino

Preprint
G. L. Report No. 3762
August 1984

Presented at the DARPA/AF Review of Progress in Quantitative NDE
San Diego, California

AFOSR F49620-79-C-0217/ONR N00014-78-C-0283/CMR

Edward L. Ginzton Laboratory
W. W. Hansen Laboratories of Physics
Stanford University
Stanford, California 94305

Invited Paper

# MEASUREMENT TECHNIQUES FOR ELECTRONIC DEVICES

Gordon S. Kino

Edward L. Ginzton Laboratory
Stanford University
Stanford, California 94305

## INTRODUCTION

Recently, a great deal of attention has been devoted to problems of manufacturing technology. NDE techniques are beginning to be considered and to be applied to problems of measurement of structures during the manufacturing process, rather than only determining whether there are faults present after manufacture. The major advantage of adopting such procedures is their cost effectiveness. Either expensive manufacturing processes need not be carried out on parts which already have faults, or an earlier process can be repeated to eliminate the fault before carrying out further manufacturing steps.

Such problems occur on both large-scale devices familiar in conventional NDE, and on small-scale devices such as semiconductors, diamond machined parts, and magnetic recording heads and disks. The conventional NDE techniques can prove extremely useful, but they must be scaled down to the appropriate sizes.

We shall discuss, in this paper, measurements of surface features, measurements of near-surface material properties, and to a limited extent, measurements of certain types of electronic properties of semiconductors. We will discuss techniques which we have examined and which may be of help, in particular, for use with semiconductor devices and magnetic recording devices. We summarize some of the possibilities of measurement of semiconductors in Table 1. We consider first the problem of evaluating surface profiles. A typical sequence of operations in the manufacture of a semiconductor device is shown in Fig. 1. Layers of $SiO_2$ are routinely used in semiconductor devices. Holes are cut in them by the photoresist process shown in Fig. 1. The photoresist in this example is laid down on top of the $SiO_2$, and is exposed photographically. A hole is cut in it by removing unexposed photoresist with solvent; the $SiO_2$ in this region can then be removed by etching. In practice, multiple-layer systems can be

Table 1

SEMICONDUCTORS

Examples of Needs for Surface Feature Measurements

Surface Profiles
Width and Thickness of Metal Films
Width of Holes in Photoresist
Edge Profiles in Photoresist
Width of Holes in $SiO_2$
Thickness of $SiO_2$ Layers

Other Needs

To measure thermal bonds, film adhesion, carrier recombination rates, and doping density

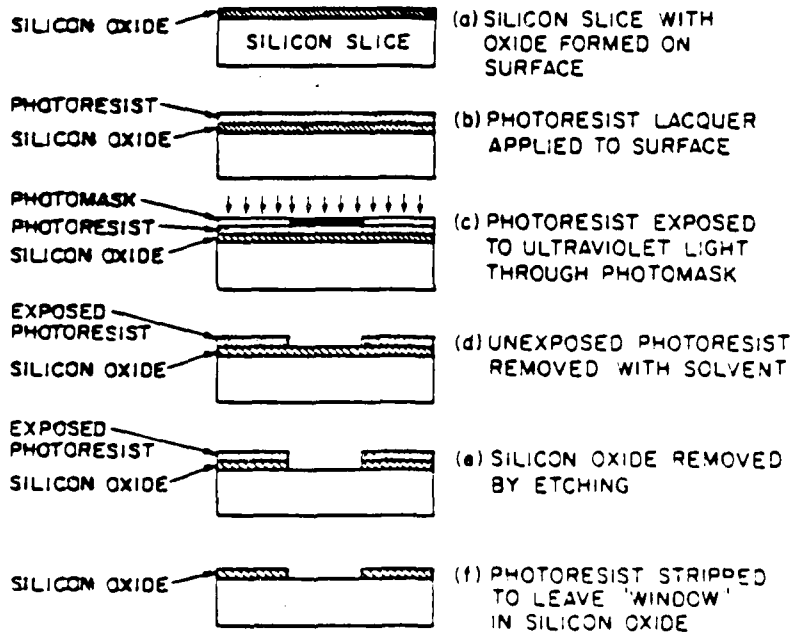


Fig. 1. Selective oxide removal by the photoresist process.

made in this way, and it is obviously of importance to be able to measure the width of the holes so cut, the shape of the edges of the holes, and the thickness of the individual layers that are being formed.

Further steps in the process may be carried out, as illustrated in Fig. 2. Similar kinds of measurements are required at each step. Each of the features that must be measured are presently of the order of one to a few micrometers in width; as progress is made, the requirements become more and more severe, down to 0.5 μm or even less. As there may be several hundred thousand devices built on one chip, it is impractical, regardless of the measurement system used, to measure every device on the chip; the information content is too large. What can and should be done is to measure test samples on each chip to evaluate whether the processing methods employed are working correctly.

A similar set of problems occur with magnetic recording disks and heads. A simplified illustration of such a recording disk and head is shown in Fig. 3, listing some of the properties that need to be measured. In magnetic recording, the magnetic recording head floats on an air bearing a few thousand Angstroms away from the disk on which the recording is made. The disk is typically of aluminum with a ~1 μm thick layer of ferrite-filled epoxy laid down on it. The thickness of the air gap is of great importance.

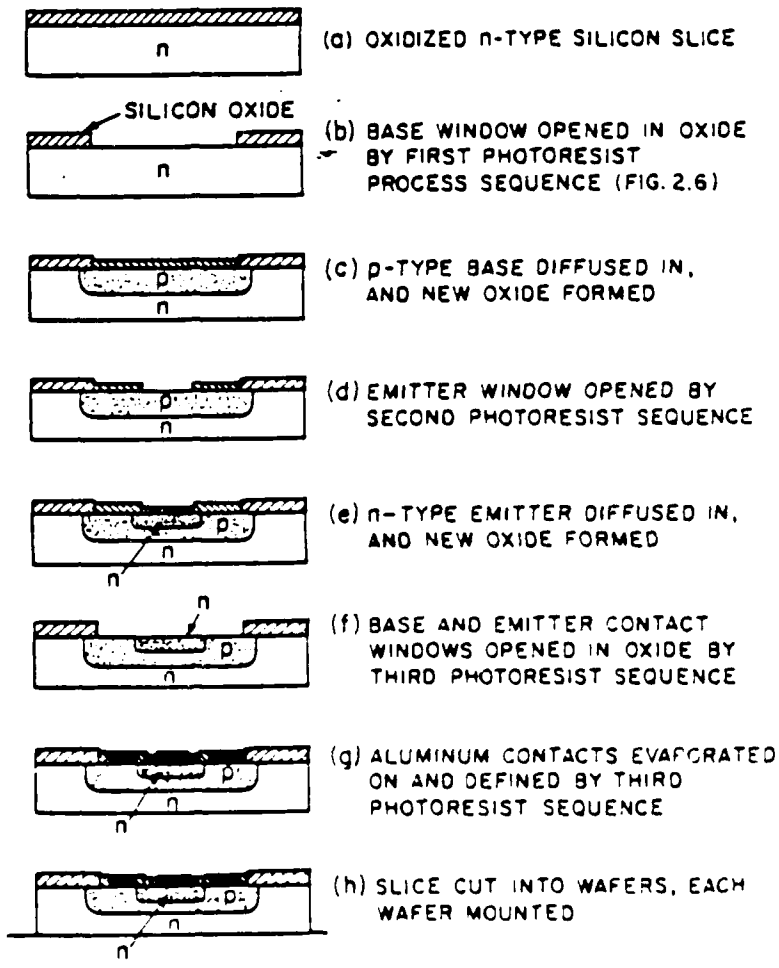


Fig. 2. Steps in the diffused planar process.

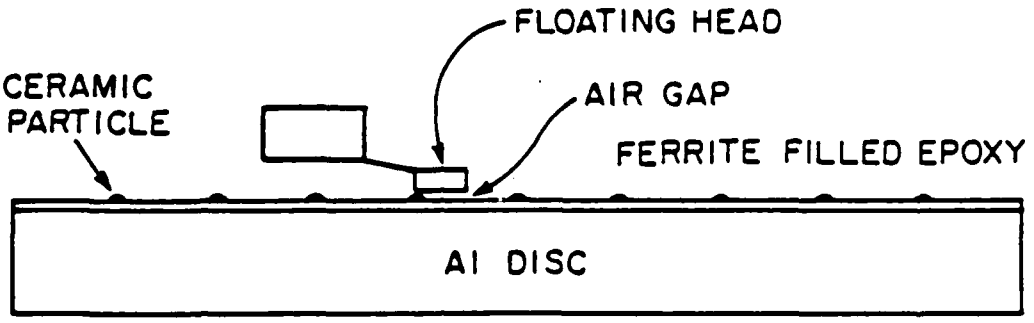


Fig. 3. Simplified schematic of a magnetic disk and head. Need to measure: surface waviness, roughness, thickness of epoxy, filling factor, air gap, head surface, stress profile.

The filling factor of the epoxy must be known and the thickness and waviness of this layer must be controlled very carefully. Furthermore, in order to stop the head from "crashing" on the disk as the disk slows down, ceramic particles are distributed in the epoxy on which the head can rest. Other problems occur in the manufacture of the head itself. Stress in the ceramic material of the head can cause it to bow. Careful control of its surface finish and its flatness are required, as well as measurements of the air gap between the disk and the head and measurements of the disk itself.

The types of sensors which can be used to make the required measurements are varied, but are basically scaled down versions of the sensors normally used in NDE applications. Thus, the optical and acoustic sensors required typically become microscopes of one kind or another, as often the photoacoustic sensors become. A summary of the types of sensors that could be used is given in Table 2.

We shall now discuss some examples of the sensors which can be used and which we have tried in simple applications.

Table 2

TYPES OF SENSORS

| | |
|---|---|
| Optical: | Scanning and Standard Microscopes |
| Acoustic: | Range Sensors, Scanned Microscope. Acoustic Wave Propagates in Solids, Liquids, or Air. |
| Photoacoustic: | Measures Thermal Effects in Solids, Liquids and Air. Also Measures Electronic Effects in Semiconductors. |

## THE ACOUSTIC MICROSCOPE

The scanning acoustic microscope was developed at Stanford by Calvin Quate and his co-workers.[1] An early version of this microscope is illustrated in Figs. 4 and 5. An acoustic transducer on a sapphire or quartz substrate excites a plane wave. A spherical hole is cut into the opposite surface of the sapphire or quartz substrate. This forms a spherical lens which produces a tightly focused beam in water. The focused beam, which impinges on the material being examined, is reflected from it and received back again at the transducer. As the reflectivity of the material being examined varies with its surface properties, the intensity of the received image from a small region controlled by the focused beam will depend on the nature of the material being examined. A two-dimensional image is obtained by mechanically scanning either the sample or the transducer using essentially a loudspeaker movement for a scan in one direction, and a slower mechanical scan for the scan in the other direction. Thus, a raster image is obtained which can be displayed on a video screen. The definition of the system is comparable to the wavelength in water so that at a frequency of 3 GHz , the definition is of the order of 4000-5000 Å with correspondingly poorer definitions at lower frequencies. Definitions of 300 Å have been obtained with liquid helium as the operating medium.

The contrast of the image is determined not only by the reflectivity of the surface, but also by the phase of the reflected waves, as illustrated in Fig. 6.[2] Suppose the beam is focused so that the focal point is below the surface of the solid. It is then possible for the lens to excite Rayleigh or surface waves on the substrate, which can be reflected back to the lens and received by it. Only certain rays from the lens cause Rayleigh wave excitation. These rays are incident at an angle $\theta_R$ where

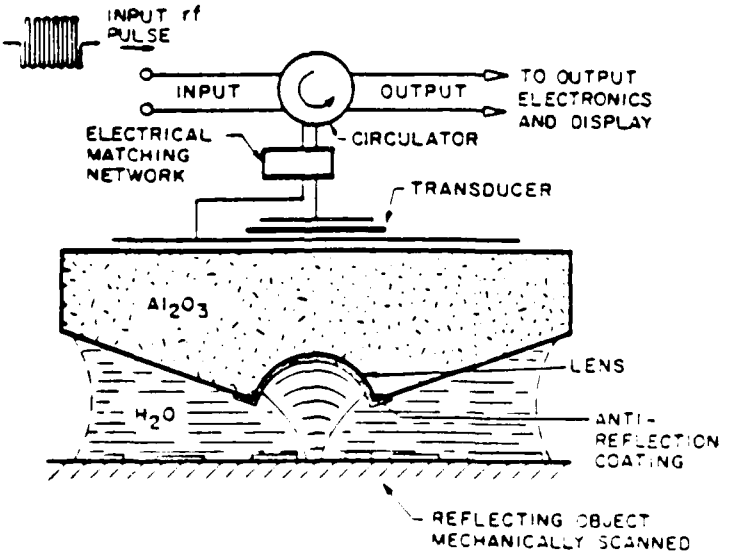


Fig. 4. Schematic of acoustic microscope.

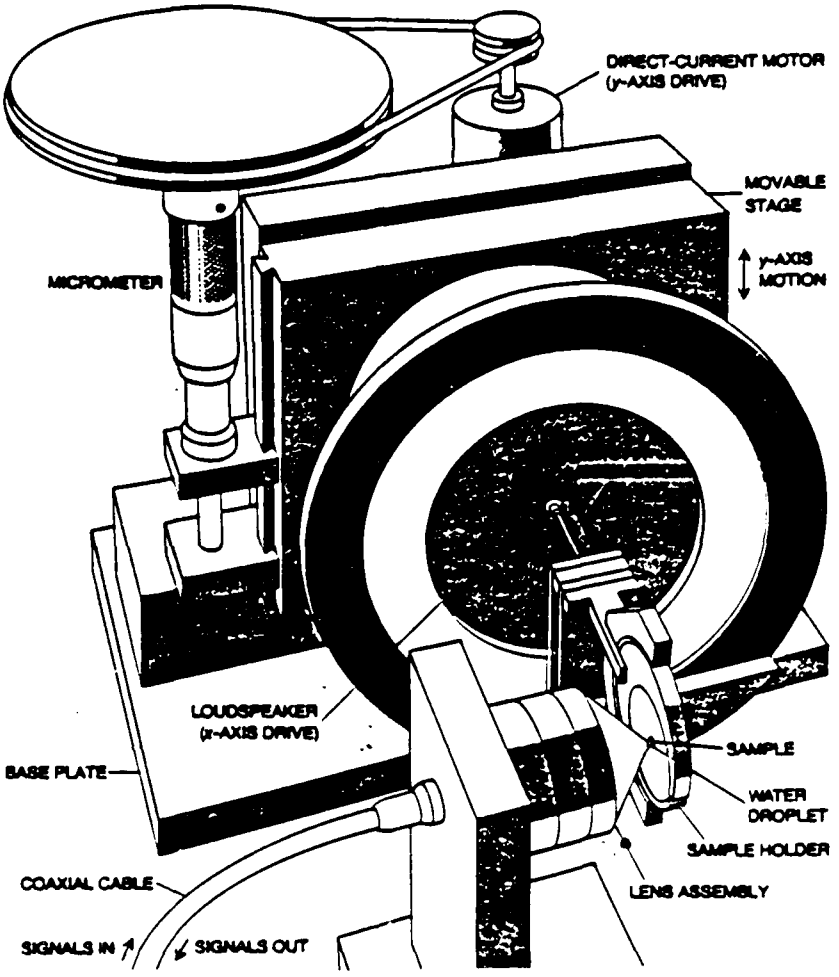


Fig. 5. Mechanical scanning of the sample in two dimensions is accomplished in the present version of the Stanford acoustic microscope by means of the apparatus depicted here. The round disk holding the sample is displaced horizontally 100-200 μm by a loudspeaker vibrating at a frequency of 60 Hz. The vertical displacement of the sample and the loudspeaker assembly are driven by a direct-current electric motor (the vertical motion is much slower than the horizontal motion). The reflected acoustic signals from the sample are processed electronically and are used to modulate the intensity of the electron beam in a television monitor. The image is formed by scanning the electron beam across the screen in synchrony with the motion of the sample across the focal point of the acoustic beam. It is the ratio of displacements of the two beams that determines the magnification of the final image.

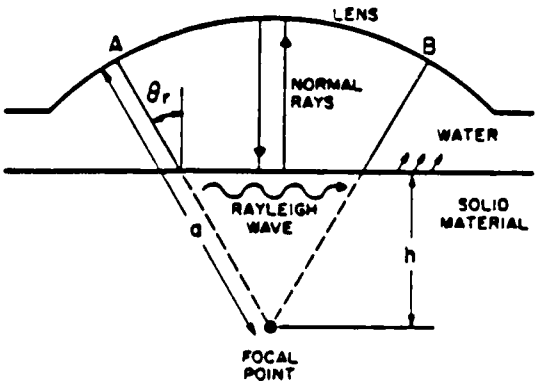


Fig. 6. Specular and Rayleigh reflected waves in the acoustic microscope.

$$\sin \theta_R = V_W V_R$$

where $V_W$ is the acoustic wave velocity in water, and $V_R$ is the Rayleigh wave velocity on the solid.

As shown in Fig. 6, two signal components arrive back at the lens, those which follow the Rayleigh wave path and those which are specularly reflected from the surface. These two sets of rays can interfere with each other and may add in phase or out of phase, depending on the distance $z$ of the focal point from the surface. As the lens is moved up and down, the voltage $V(z)$ received by the transducer varies with $z$. As the lens is moved across a surface whose material properties vary, $V(z)$ will vary. Therefore, the contrast changes obtained with the microscope are very sensitive to surface properties.

Fig. 7 is an illustration of an image of a metal film laid down on a glass substrate.[3] The optical images shown for comparison and the images obtained at two different values of $z$ are also shown. It will be seen that the contrast changes with $z$. The poor adhesion of the metal films near their edges shows up very clearly in the acoustic microscope pictures, but is not observed optically. This is because the Rayleigh wave velocity varies radically with the adhesion of the metal film. Consequently, acoustic microscopy techniques can be very useful for measuring adhesion, bonding and other mechanical properties which are difficult to evaluate by other techniques.[3]

We have attempted to put acoustic microscopy on a more quantitative basis and have arrived at techniques for measuring the phase and the amplitude of the reflected signal components separately.[4,5] This makes it possible to determine the height and width of surface features separately, as well as to determine sur-

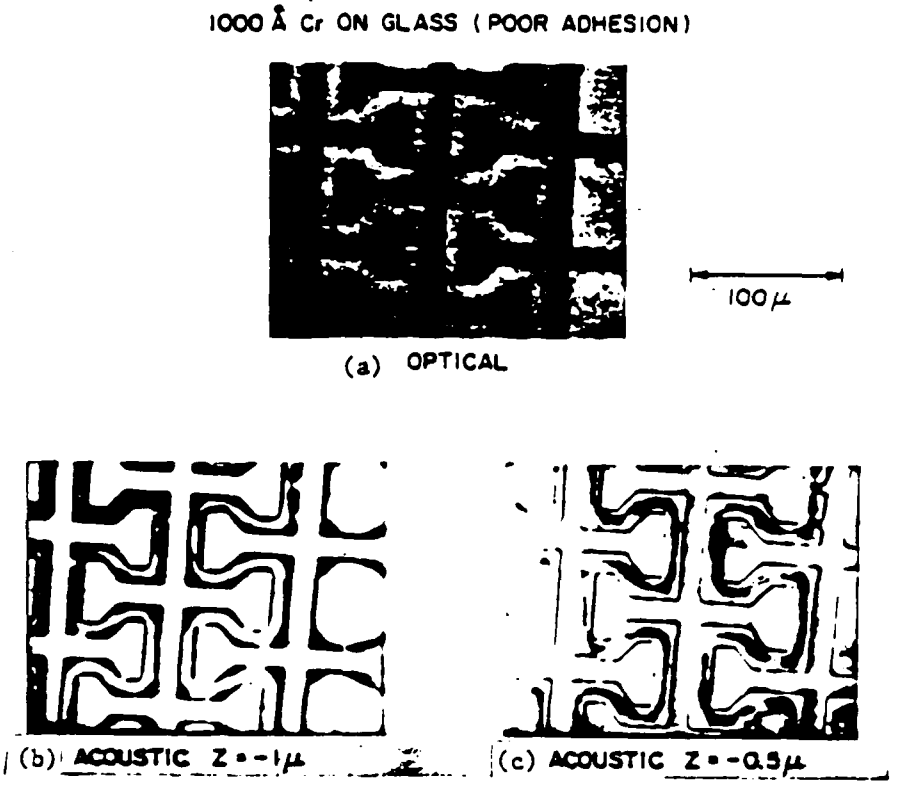


Fig. 7. Images of a metal film on glass. (a) An optical image. (b) An image taken with a 2 GHz acoustic microscope. (c) An image with a defocus distance of $-0.5\ \mu m$ .

face material properties from the measurement of the Rayleigh wave velocity. It also makes it possible to carry out Fourier transforms of the reflected image and other kinds of processing since both amplitude and phase information are available. The technique employed is illustrated in Fig. 8. A short tone burst is inserted into the transducer and is reflected from it. The specularly-reflected component arrives at a different time from the Rayleigh wave component so that they can be measured separately. Using this technique, we can determine the phase difference between these two signals to an accuracy of $0.1^{\circ}$ which corresponds to being able to measure the Rayleigh wave velocity to one part in $10^3$ .

In an alternative mode of operation, we excite a hollow beam on an outer ring surrounding the lens. This beam is reflected from the substrate and is used as a reference. We compare it with the reflection from a focused beam whose focal point is at the surface of the substrate. We can control the average height of the transducer from the substrate by comparing the phase of the signal returned from the reference beam (several millimeters in diameter) with an external reference; we use a piezoelectric

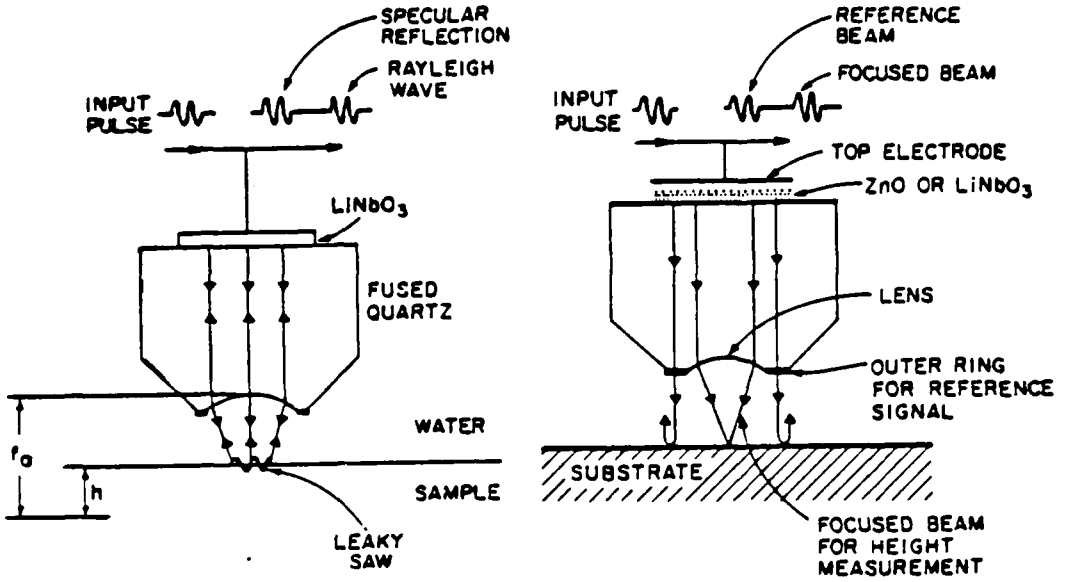


(a) (b)

Fig. 8. (a) Rayleigh wave velocity measurement. (b) Acoustic microscope lens for topography profiling.

pusher to move the transducer up and down. As the transducer is moved across the substrate, the phase of the specularly-reflected focused beam (~30 μm diameter) gives an accurate measure of the height of the region being observed. By this means, we can measure changes in height of the surface to an accuracy of $\lambda/3000$, where $\lambda$ is the acoustic wavelength in water.

An example of work by Liang, Bennett, Khuri-Yakub and Kino is shown in Fig. 9, in which these techniques were used to measure the thickness of a 5000 Å layer of aluminum using 50 MHz acoustic waves with a wavelength of 30 μm.[4] The Rayleigh wave technique was then used to measure the velocity of a surface wave along the aluminum, thus giving a measure of the material properties of the surface.

The technique can also be used to measure the width of surface features very accurately. Using the focused beam, and measuring its phase, we have been able to measure the width of surface films whose widths are quite comparable to the spot size of the beam. By using Fourier transform techniques, it is possible to put these measurements on a highly quantitative basis in which the results do not depend too critically on the fact that the focus of the beam is exactly at the substrate.[6] Thus, acoustic microscopy and related scanning optical microscopy techniques can be very useful in this application.

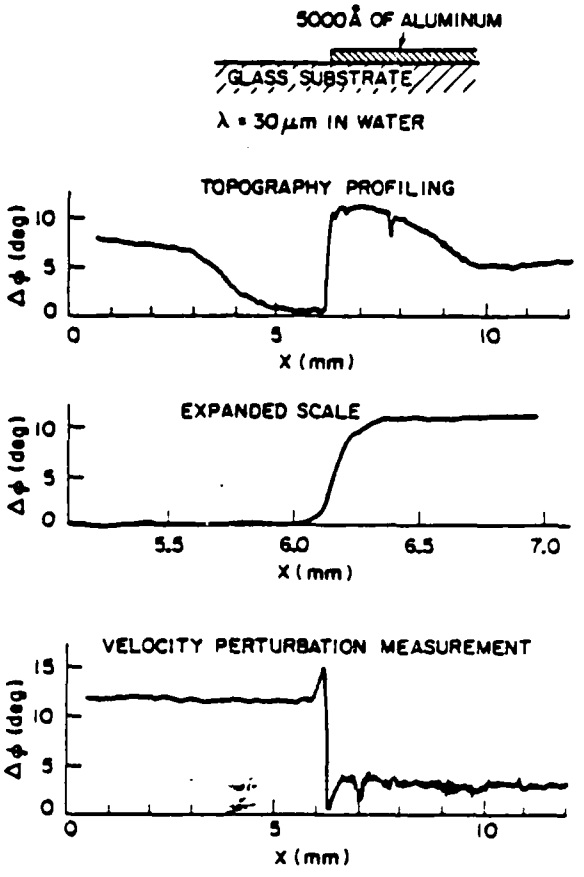


Fig. 9. Measurements and topography of velocity perturbation taken with a 50 MHz acoustic microscope.

## SCANNING OPTICAL MICROSCOPE

After we were able to obtain good phase and amplitude information directly with a scanned acoustic microscope, we were prompted to see if we could duplicate this kind of operation with an optical microscope. One of the problems with scanning optical microscopy, or any kind of quantitative microscopy for that matter, is that, because of the precision required, vibrations can cause great difficulty in measurements. Therefore, a very solid optical bench and other equipment are needed. One of our aims was to eliminate this difficulty; another was to use modern electronic signal processing techniques to measure phase to an accuracy of a few degrees rather than using standard optical interference techniques. This would make it possible to measure, simultaneously, the width and height of surface profiles using the same system. Presently, such measurements of width can typically be made with one kind of device, and measurements of height with another, but it is not usually possible to measure the height or thickness accurately in regions of very small transverse dimensions.

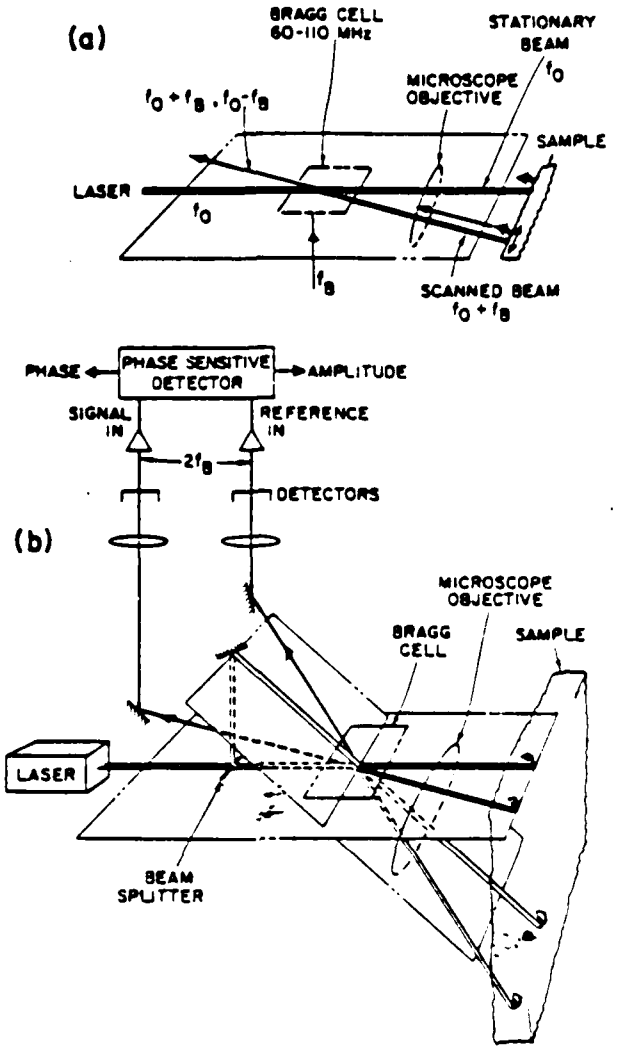


Fig. 10. Scanning optical microscope. The Bragg cell splits the input beam and scans the deflected and frequency shifted beam across the sample. The undiffracted beam is used as a reference. (a) Simplified schematic. (b) Secondary reference on sample to compensate for surface tilt.

The system we have developed is an electronically-scanned optical microscope with a stationary reference on the sample so as to eliminate the effect of vibrations. The basic device is shown in Figs. 10a and 10b. A laser beam of frequency $f_0$ is passed through a Bragg cell whose frequency can be varied from 60-110 MHz . The Bragg cell deflects the acoustic beam. The deflection angle is linearly proportional to the frequency $f_B$ , the input to the Bragg cell. A deflected and undeflected beam pass through a microscope objective lens, producing two focused spots on the surface of the sample. The incident beams are reflected from the sample, pass again through the Bragg cell, and produce two signals along the path shown; these signals are of frequencies $f_0 + f_B$

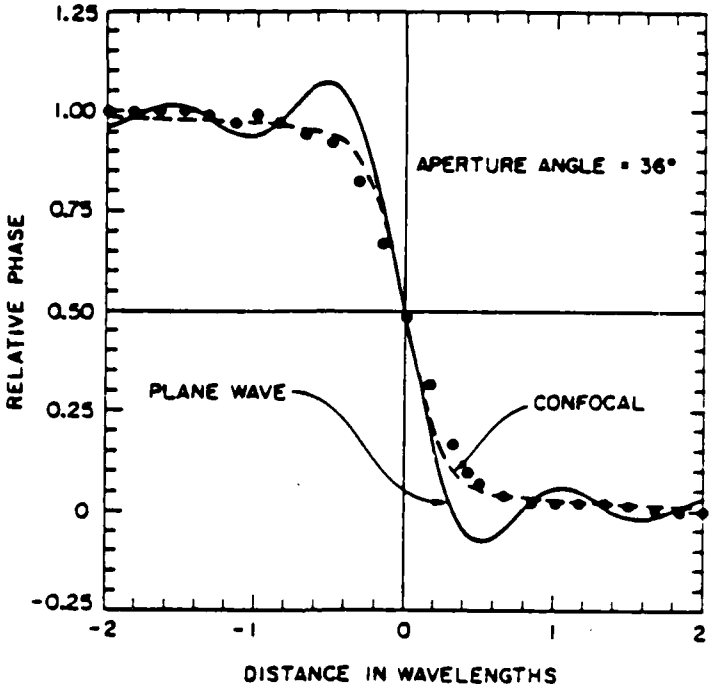


Fig. 11. Theoretical and experimental phase profiles of a step taken with plane wave illumination (solid line) and a confocal lens system (broken line).

and $f_0 - f_B$, respectively. The phase difference between these two signals is equal to the optical phase difference of the two reflected beams from the sample. By passing the received beams into a photodetector, a product signal is obtained from the photodetector at a frequency $2f_B$ whose amplitude depends on the amplitude of the scanned beam and whose phase is the phase difference of the signals of the two beams. We therefore have arrived at a technique for measuring the phase and amplitude of the optical beams, but carry out this measurement at frequencies that can be handled by electronic circuitry.[6]

The actual system is somewhat more complicated because it is necessary to provide a reference signal at a frequency $2f_B$. Since there is a phase change from the input signal to the Bragg cell to the point where the optical beam is incident, and this phase change varies with frequency, and hence deflection angle, it is necessary to eliminate this error. We do this by using two incident beams on the Bragg cell, as shown in Fig. 10b, obtaining the reference signal from the second set of beams. The second set of beams is passed through a narrow aperture and therefore produces two wide beams on the sample whose transverse size is perhaps fifty times that of the well-focused spot. Therefore, as the secondary set of reference beams is scanned by the Bragg cell, it is not much affected by fine changes in surface profile.

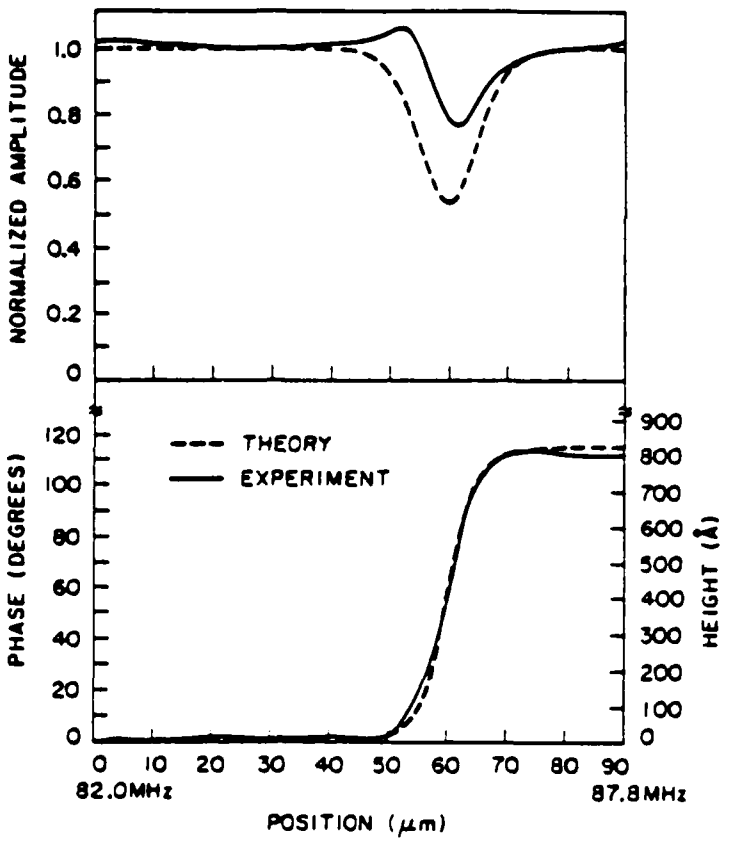


Fig. 12. Amplitude and phase variation across an aluminum step on a metallized substrate. The phase step indicates a height of 820 Å .

A major advantage of this reference system is that it is neither sensitive to vibration normal to the lens, or to tilt. The operating system is so insensitive to these parameters that banging on the optical bench with a hand has very little effect.

Another advantage of such a scanned optical system is that, because the same beam is used for transmission and reception, the point spread function of the lens is squared. Hence, the sidelobe levels are extremely low, and there is very little ripple when one observes sharp steps. We have carried out a detailed theory to predict what should occur and have carried out measurements to confirm our theory. Some simple results which were obtained for the acoustic microscope are shown in Fig. 11.[4,5] As the beam is passed over a step, the transition is extremely smooth as opposed to what would be expected theoretically for a plane wave illumination, where the transition shows some ripple. The theoretical profile to be expected for this confocal scanned system is shown as the dashed line; the experimental results for the acoustic microscope are shown as points. The agreement is excellent.

We have used this optical microscope to obtain the results shown in Fig. 12; in these preliminary experiments we measured a step of 800 Å of aluminum on aluminum.[6] It will be seen that

the measured phase is in good agreement with what would be expected. The amplitude profile is only in fair agreement with what would be expected; later results indicate far better agreement than shown here.

## PHOTOACOUSTIC TECHNIQUES

Photoacoustic methods are ideal for measuring thermal properties of materials such as the integrity of a bond between a silicon substrate and a heat sink, the lack of adhesion of a metal film, the presence of near-surface defects in materials, and the integrity and quality of current-carrying conductors. Related techniques can also be useful for measuring electronic properties of materials such as doping density profiles and recombination rates of carriers. We shall describe here a subset of problems of this nature which we have investigated. Other related problems are described in a paper in this issue by Stearns et al.[7]

The technique we have employed is different from conventional photoacoustic methods. Most commonly, a heat source such as a modulated light beam is incident on a sample.[8] This modulates the near-surface temperature of the sample. In turn the thermal expansion and contraction of the material, caused by the change in temperature, excite an acoustic wave in the material which is detected with an acoustic transducer on the opposite side of the sample. An alternative method, which has been used extensively, is to measure the acoustic wave generated in the air above the sample.

In one example, shown in Fig. 13a, we excite an acoustic surface wave with a wedge transducer placed on the sample and receive it on a similar transducer.[8] The modulated light incident on the sample changes its near-surface temperature. This temperature modulation in turn varies the phase of the received signal. Thus, with this technique, the laser heating perturbs an acoustic wave rather than excites one. A second method, shown in Fig. 13b, uses an acoustic wave incident on the surface of the substrate from a focused transducer in air; the reflected wave is received on a second transducer. The phase change of the acoustic wave caused by the temperature modulation of the air yields a direct measurement of temperature. The technique is extremely sensitive and can be operated over a broad band of frequencies. It also has the advantage that it can be used to localize the region being examined. In another example of the technique, an acoustic microscope excites acoustic surface waves so that we can examine regions where the temperature is modulated on the surface of a material. In this case we obtain the transverse definition of the acoustic microscope.

An accompanying paper by Stearns et al includes a discussion on how these techniques can be exploited to measure the thermal properties of silicon bonded to a heat sink.[7] We shall therefore not discuss thermal measurements any further. Instead, we shall focus on the utility of alternative methods which measure the electronic properties of a semiconductor.[9]

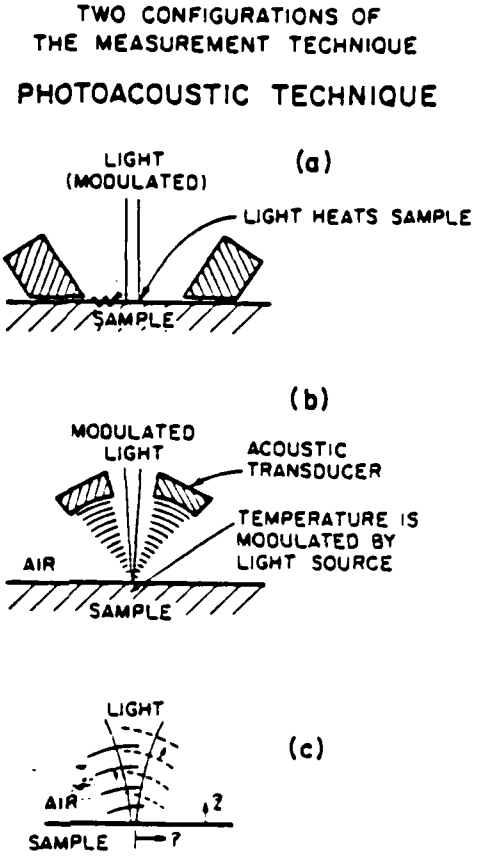


Fig. 13. Configuration of a photoacoustic measurement technique. (a) Surface wave measurement with a wedge transducer. (b) Acoustic transducer in air. (c) An illustration of the path of a light beam and acoustic beams in air.

Suppose we use the configuration of Fig. 13a with argon light incident on a silicon sample. In this case, the light will generate electrons and holes. The electrons and holes will, in turn, perturb the acoustic surface wave velocity. The perturbation will be proportional to the carrier density. As the frequency of modulation is increased, the phase perturbation will not change in amplitude until the modulation frequency becomes comparable to the recombination frequency of the carriers. At this point the effects begins to fall off. At very low frequencies temperature effects are also important.

Some results taken on a P-type silicon sample are shown in Fig. 14. It is seen that the magnitude of the effect falls off, as predicted. Furthermore, the phase of the perturbation relative to the phase of the input chopping signal also changes, as illustrated in Fig. 14b. It will be seen that the phenomenon is well understood, and the agreement between experiment and theory is excellent.

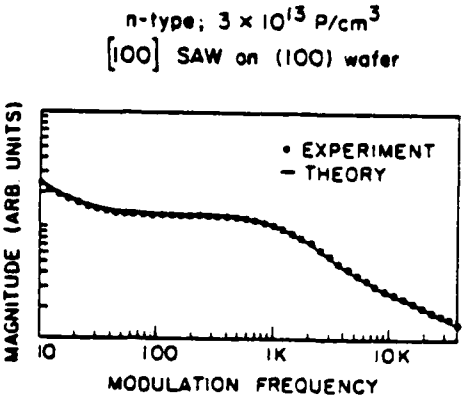


Fig. 14. Acoustic phase perturbatin in Si.

The technique, therefore, provides a method of measuring recombination rates of carriers in a small region of the semiconductor. If an acoustic microscope is used for exciting the surface waves, then no contact need be made to the semiconductor.

## CONCLUSIONS

We have discussed a number of techniques for examination of electronic devices. Due to limitations of space, we have concentrated on only a few of the available methods. The acoustic and optical microscopes are very powerful tools for measuring mechanical properties, adhesion surface profiles, and sizes of small features. Photoacoustic techniques are useful for measuring thermal properties of materials; they can also be used for measuring electronic properties. Related techniques may be useful for measuring doping profiles in materials without making contact with the surface.[10] Other techniques, which employ acoustic waves excited in air, are also being developed for measuring surface profiles. The great advantage of these techniques is that the surface is not contaminated by the probing technique itself.

## ACKNOWLEDGMENT

This work was supported by the Air Force Office of Scientific Research under Contract No. F49620-79-C-0217, the Office of Naval Research under Contract No. N00014-78-C-0283, and the NSF-MRL Program through the Center for Materials Research at Stanford University.

## REFERENCES

1. R. A. Lemmons, C. F. Quate, "Acoustic Microscopy," in Physical Acoustics: Principles and Methods, Eds: W. P. Mason and R. N. Thurston 14, Academic Press, New York (1975).
2. A. Atalar, "A Physical Model for Acoustic Signatures," J. Appl. Phys. 50, 8237-8239 (1979).
3. R. C. Bray, J. Calhoun, R. Kock, and C. F. Quate, "Film Adhesion Studies with the Acoustic Microscope," J. Thin Solid Films 74, 295-302 (1980).

4. K. Liang, B. T. Khuri-Yakub, S. D. Bennett, and G. S. Kino, "Phase Measurements in Acoustic Microscopy," Proc. IEEE Ultrasonics Symp., Atlanta, Georgia (October 1983).
5. K. Liang, S. D. Bennett, and G. S. Kino, "Precision Phase Measurements with the Acoustic Microscope" submitted to IEEE Sonics and Ultrasonics for the Special Issue on Acoustic Microscopy (March 1985).
6. R. L. Jungerman, P. C. D. Hobbs, and G. S. Kino, "Phase Sensitive Scanning Optical Microscope," submitted to Appl. Phys. Lett. (June 1984).
7. R. G. Stearns, B. T. Khuri-Yakub, and G. S. Kino, "Phase-Modulated Photoacoustics," presented at the DARPA/AF Review of Progress in Quantitative NDE, San Diego, California (July 1984).
8. R. G. Stearns, B. T. Khuri-Yakub, and G. S. Kino, "Phase Modulated Photoacoustics," Proc. IEEE Ultrasonics Symp., Atlanta, Georgia (October 1983).
9. R. G. Stearns, B. T. Khuri-Yakub, and G. S. Kino, "A Photoacoustic Technique for Measuring Excess Carrier Density and Lifetimes in Silicon," submitted to Appl. Phys. Lett. (June 1984).
10. G. S. Kino, J. D. Fox, and B. T. Khuri-Yakub, "Very High-Frequency Acoustic Transducers for Operation in Air," presented at the Second Symposium on Energy Engineering Sciences, Argonne National Laboratory (April 1984).

and $h'(x_0,y_0)$ and $h(x_0,y_0)$ are respectively the acoustic microscope point spread functions (PSF) at the top of the strip and at the surface of the substrate, and $R_F$ and $R_S$ are respectively the reflectance functions of the water/film interface and the water/substrate interface.

The second term of $v_0(x_s)$ in Eq. (1) is unimportant because it is a constant due to the background reflection from the substrate. The first term, however, explicitly shows a convolution relation between $\mathrm{rect}(x_0/D)$, which describes the geometric width of the strip, and an effective line spread function $h''(x_0)$ that takes into account the different reflectances and vertical heights of the surfaces of the strip and the substrate. In other words, $v_0(x_s)$ is a blurred image profile of the actual strip. $v_0(x_s)$ can be a very complicated waveform, particularly when the strip width D is comparable to the spot size of the focused acoustic beam, or the beam is defocused. This makes it difficult to accurately determine D by locating the edges of the strip. This difficulty with the spatial domain response is the primary motivation for the Fourier spectrum approach to the line width measurement problem described below.

Since a convolution in the spatial domain corresponds to a multiplication in the spatial frequency domain, one obtains from Eq. (1)

$$V_0(f_x) = D \,\mathrm{sinc}(Df_x)\, H''(f_x) + B\,\delta(f_x) \qquad (3)$$

where $H''(f_x)$ is the Fourier transform of $h''(x_0)$. $V_0(f_x)$ vanishes at the zeros of the "sinc" function, which occur at

$$Df_x = n \qquad n = \pm 1, \pm 2, \ldots \qquad (4)$$

It follows that

$$D = n/f_{x,\mathrm{zero}} \qquad (5)$$

It can be shown that for a confocal system, $H''(f_x)$ has low pass characteristics with a upper cutoff frequency of

$$f_{x,\max} = 1/(\lambda F) \qquad (6)$$

where F is the f-number of the lens. $H''(f_x)$ is in general non-zero within the passband, and is identically zero above the cutoff frequency. Thus the zeros of $V_0(f_x)$ for $0 < f_x < f_{x,\max}$ are exactly those of the "sinc" response of the strip. As long as the zeros fall inside the passband, i.e.

$$D > F\lambda$$

the strip width can be determined from Eq. (5). For instance, if $F = 0.35\lambda$, one can, in principle, resolve line widths as small as $0.35\lambda$.

The power of this Fourier transform technique lies in its simplicity. Given a priori knowledge of the strip geometry, one only has to be aware of some general properties, but does not need to know the exact details, of the imaging system response. The mere location of the zeros of the overall spectral response suffices for the accurate determination of the line width.

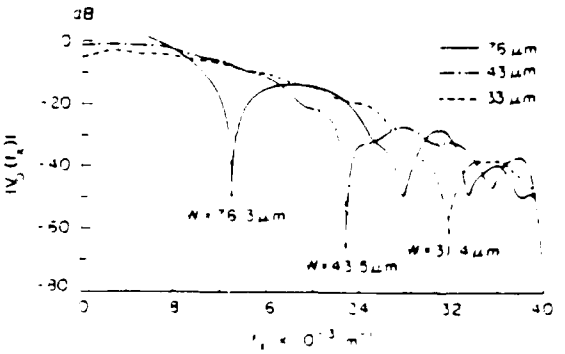


Fig. 2. Fourier spectra of the acoustic microscope spatial response to 5000 Å thick gold lines on fused silica from 1 to 2.5 wavelengths wide.

## 2. Experimental Results

Fig. 2 illustrates the experimental $|V_0(f_x)|$ for 5000 Å thick gold lines deposited on a fused quartz substrate. The optically-measured widths are D = 76, 43, and 33 μm, respectively. The acoustic microscope operates at 50 MHz ($\lambda$ = 30 μm) with a f/0.35 lens, and the acoustic beam is focused on the surface of the fused quartz substrate. The line widths estimated from the position of the first zero of $|V_0(f_x)|$ agree very well with the optically-determined widths. The minor discrepancies are mainly due to the nonuniformity in the widths of the gold lines.

In addition, it is important to realize that this Fourier transform approach is essentially insensitive to defocusing. It is obvious from Eq. (3) that defocusing only changes the effective spectral response $H''(f_x)$ slightly, and does not introduce any new zeros to, nor does it affect the zeros of, $V_0(f_x)$. Fig. 3 shows the experimental $|V_0(f_x)|$ for a 2000 Å thick and 76 μm wide chrome line on fused quartz at various defocusing distances. The focus was in turn located on, and at 60 μm and 40 μm above, the substrate. The locations of the first zero in all three cases are essentially coincident, giving a width estimate of 76.3 μm.

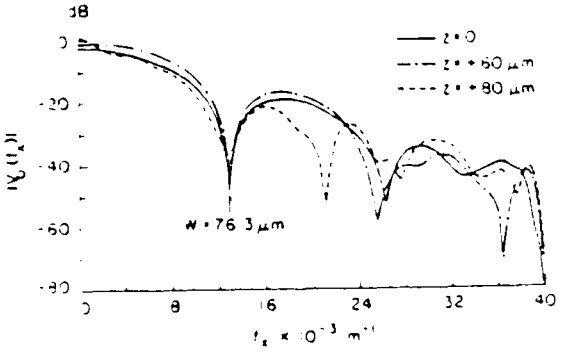


Fig. 3. Fourier spectra of the acoustic microscope spatial response to a 2000 Å thick and 76 μm wide chrome line on fused silica at different defocusing distances.

## II. Material Characterization by Inversion of V(z)

The Fourier transform relation between $V(z)$ and the the reflectance $R(\theta)$ of a liquid/solid interface has been derived and demonstrated experimentally in acoustic microscopy.[2,3] However, the $V(z)$ integral on which the derivation of the Fourier transform relation is based is formulated using the paraxial approximation, and is therefore not valid for acoustic lenses with a large angle of convergence. An alternative hybrid formulation, which combines elements of angular spectrum and ray optics formalisms, has been carried out and the result is given below. It should be noted that no paraxial assumption is necessary for its development. New results for different materials obtained by inverting complex $V(z)$ data acquired with a special spherical transducer operating at 10 MHz are also shown.

### 1. Theory

The special case of a focused spherical transducer radiating directly into water with no buffer medium is considered as shown in Fig. 4. The practical significance of this acoustic lens configuration will be explained later. The special transducer geometry simplifies the derivation, and yet the final solution has general validity for any acoustic lens configuration which produces a converging spherical wave.

It can be shown that the voltage response $V(z)$ of the focused transducer is given by[4]

$$V(z) = \int P^2(k_z) R(k_z) \exp(-jk_z 2z) \, dk_z \qquad (1)$$

where $2z = 2z_0 \cos\theta$, $k_z$ is the wave vector component in the z direction, $P(k_z)$ is the pupil function of the lens, and $R(k_z)$ is the reflectance function of the liquid/solid interface. Eq. (1) shows that $V(2z)$ and $P^2(k_z)R(k_z)$ form a Fourier transform pair. The inversion to obtain $R(k_z)$ is given by

$$R(k_z) = \begin{cases} \dfrac{\mathcal{F}^{-1}\{V(z')\}}{P^2(k_z)} & P(k_z) \neq 0 \\ 0 & P(k_z) = 0 \end{cases} \qquad (3)$$

In general, $P(k_z)$ is not known a priori. However, $P^2(k_z)$ can conveniently be calibrated by inverting the $V(z)$ for a liquid/solid interface whose reflectance has uniform magnitude and phase over the angular extent of the lens pupil function. The water/lead boundary is one such example, and the magnitude and phase of the reflectance is essentially flat from 0° to 40° incidence.

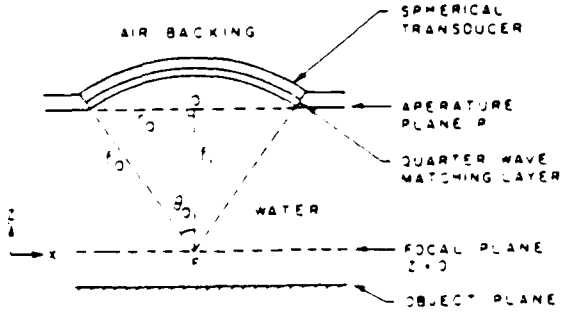


Fig. 4. Special focused transducer used for the $V(z)$ measurements.

This inversion approach to material characterization is different in that it requires the measurement of $V(z)$ in both amplitude and phase, whereas previous work[4,5] utilized only the amplitude or intensity of $V(z)$. It is generally not trivial to conduct high-accuracy phase measurements in acoustic microscopy. We have developed a phase measurement system that makes possible the precision acquisition of phase data and the experimental demonstration of the inversion technique.

### 2. Experimental Results

A special acoustic lens is used for the $V(z)$ measurement. The acoustic transducer is a piezoelectric element in the form of a spherical shell with air backing and a quarter-wave matching layer on the front face. The transducer generates a converging spherical wave directly into water. This acoustic lens configuration is advantageous for the $V(z)$ measurement for the following reason. The elimination of the buffer rod removes the systematic noise due to reverberations inside the buffer rod. This type of noise tends to overlap in time with the reflected signal from the object. With the present lens construction, the acoustic lens can be translated over a wide range of $z$ to collect $V(z)$ data in an essentially noise-free environment.

The spherical transducer has a focal length of 15 mm, f/0.7 aperture, and is operated at 10.1 MHz. Many practical considerations go into this

particular choice of operating frequency range. The inversion of the $V(z)$ is most conveniently carried out for a lossless liquid medium. The loss in water is essentially negligible at 10 MHz, and so satisfies this requirement. Moreover, the wavelength in water of about 150 μm is sufficiently large to render any irregularity and instability in the vertical translation mechanism insignificant. For the same reason, the measurement is less subject to error as a result of surface finish imperfections in the sample.

Figure 5 shows the reflectance function of a water/fused silica interface obtained by inverting the corresponding $V(z)$ and then normalizing out $P^2(k_z)$ of the transducer. The theoretical reflectance is also shown in the solid curve for comparison. There is good general agreement between theory and experiment in both magnitude and phase. The experimental shear critical angle at $\theta = 23.6^\circ$ and the Rayleigh critical angle at $\theta = 25.85^\circ$ compare extremely well with theory. The longitudinal critical angle is not reproduced in the experimental result due to the angular resolution degradation problem caused by the spatial truncation of the $V(z)$ data.[2]

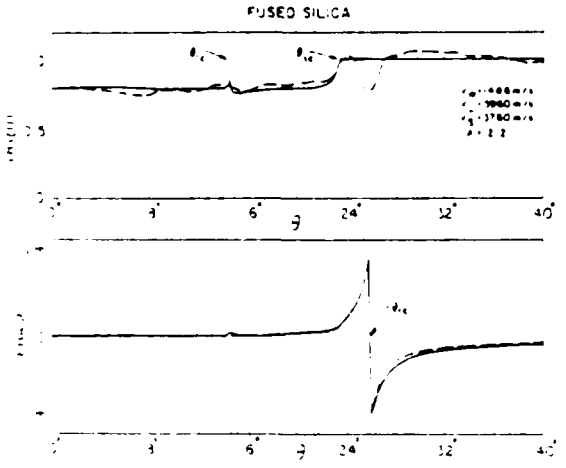


Fig. 5. Comparison of the theoretical (solid line) and experimental (dashed line) reflectance functions for a water/fused silica interface.

Figure 6 is the reflectance function for aluminum. Again, the fit between theory and experiment is very good. The longitudinal and shear critical angles show up clearly in the experimental result in this case. The Rayleigh critical angle is located at $\theta = 30.36^\circ$, which gives a phase velocity of 2997 m/s for the leaky surface acoustic wave.

Figure 7 shows the reflectance function for Plexiglas or Lucite, a low acoustic velocity material with high loss. This example illustrates how loss in materials can be determined. The longitudinal critical angle is located at $\theta = 32.7^\circ$

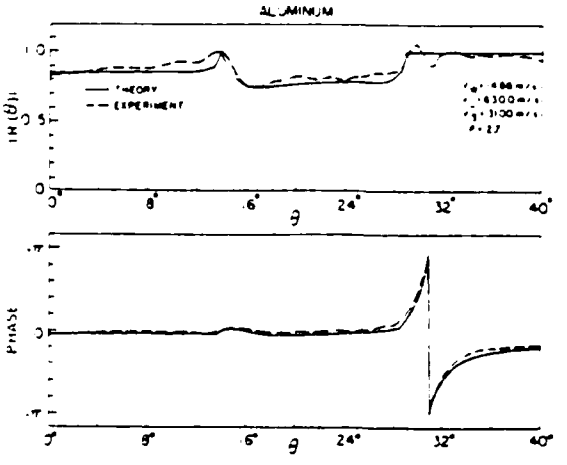


Fig. 6. Comparison of the theoretical and experimental reflectance functions for a water/aluminum interface.

which corresponds to a longitudinal wave velocity of 2750 m/s. The magnitude of the reflectance peaks at 0.7 rather than 1, as would be the case for a lossless substrate. The amount of diminution of the peak level depends on the loss for the longitudinal mode. The theoretical curve is fitted to the experimental one by varying the longitudinal loss factor $Q_L$. $Q_L$ is found to be about 50, which translates into an attenuation coefficient of 232 nepers/m, or 20 dB/cm at 10 MHz, which agrees well with other published values.[5]

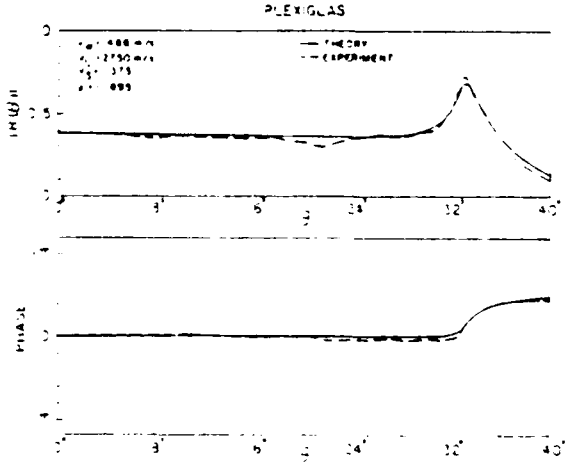


Fig. 7. Comparison of the theoretical and experimental reflectance functions for a water Plexiglas interface.

## III. Conclusion

We have developed and demonstrated a Fourier transform approach to line width measurement. For the case of strips with rectangular cross-sections,

the technique is essentially insensitive to the characteristics of the imaging system. Line widths comparable to a wavelength can be determined accurately with this method.

New results on material characterization by the inversion of complex V(z) data have also been shown. The result of a more general and non-paraxial formulation of the V(z) integral is given. This inversion technique represents a more complete approach to material characterization than previous V(z) related work. Phase velocities of various propagating modes in the material of interest can be determined from the reflectance function. In addition, acoustic losses can also be estimated.

## IV. Acknowledgment

The authors would like to thank Drs. Simon Bennett and Ian Smith for the stimulating discussions related to this work. This work was supported by the Air Force Office of Scientific Research under Contract No. AFOSR-84-0063.

## References

1. K. Liang, S. D. Bennett, B. T. Khuri-Yakub, and G. S. Kino, 'Precision Phase Measurements in the Acoustic Microscope,' IEEE Trans. Sonics & Ultrasonics, to be published (1984).
2. K. Liang, B. T. Khuri-Yakub, and G. S. Kino, 'Material Characterization by the Inversion of V(z),' IEEE Trans. Sonics & Ultrasonics, to be published (1984).
3. J. A. Hildebrand, K. Liang, and S. D. Bennett, 'Fourier Transform Approach to Material Characterization with the Acoustic Microscope,' J. Appl. Phys. 54 (12), 7016-9 (December 1983).
4. J. Kushibiki and N. Chubachi, 'Material Characterization by Line-Focus-Beam Acoustic Microscopy,' IEEE Trans. Sonics & Ultrasonics, to be published (1984).
5. R. D. Weglein, 'Metrology and Imaging in the Acoustic Microscope,' in Scanned Image Microscopy, edited by E. A. Ash, Academic Press, London (1980).
6. T. Bourdie, 'Effects of Attenuation on Reflections,' Ph.D. Thesis, Stanford University (April 1982).

Invited Paper

# MEASUREMENT TECHNIQUES FOR ELECTRONIC DEVICES

by

Gordon S. Kino

Preprint
G. L. Report No. 3762
August 1984

Presented at the DARPA/AF Review of Progress in Quantitative NDE
San Diego, California

AFOSR F49620-79-C-0217/ONR N00014-78-C-0283/CMR

Edward L. Ginzton Laboratory
W. W. Hansen Laboratories of Physics
Stanford University
Stanford, California 94305

Invited Paper

# MEASUREMENT TECHNIQUES FOR ELECTRONIC DEVICES

*Gordon S. Kino*

Edward L. Ginzton Laboratory
Stanford University
Stanford, California 94305

## INTRODUCTION

Recently, a great deal of attention has been devoted to problems of manufacturing technology. NDE techniques are beginning to be considered and to be applied to problems of measurement of structures during the manufacturing process, rather than only determining whether there are faults present after manufacture. The major advantage of adopting such procedures is their cost effectiveness. Either expensive manufacturing processes need not be carried out on parts which already have faults, or an earlier process can be repeated to eliminate the fault before carrying out further manufacturing steps.

Such problems occur on both large-scale devices familiar in conventional NDE, and on small-scale devices such as semiconductors, diamond machined parts, and magnetic recording heads and disks. The conventional NDE techniques can prove extremely useful, but they must be scaled down to the appropriate sizes.

We shall discuss, in this paper, measurements of surface features, measurements of near-surface material properties, and to a limited extent, measurements of certain types of electronic properties of semiconductors. We will discuss techniques which we have examined and which may be of help, in particular, for use with semiconductor devices and magnetic recording devices. We summarize some of the possibilities of measurement of semiconductors in Table 1. We consider first the problem of evaluating surface profiles. A typical sequence of operations in the manufacture of a semiconductor device is shown in Fig. 1. Layers of $SiO_2$ are routinely used in semiconductor devices. Holes are cut in them by the photoresist process shown in Fig. 1. The photoresist in this example is laid down on top of the $SiO_2$, and is exposed photographically. A hole is cut in it by removing unexposed photoresist with solvent; the $SiO_2$ in this region can then be removed by etching. In practice, multiple-layer systems can be

Table 1

SEMICONDUCTORS

Examples of Needs for Surface Feature Measurements

Surface Profiles
Width and Thickness of Metal Films
Width of Holes in Photoresist
Edge Profiles in Photoresist
Width of Holes in $SiO_2$
Thickness of $SiO_2$ Layers

Other Needs

To measure thermal bonds, film adhesion, carrier recombination rates, and doping density

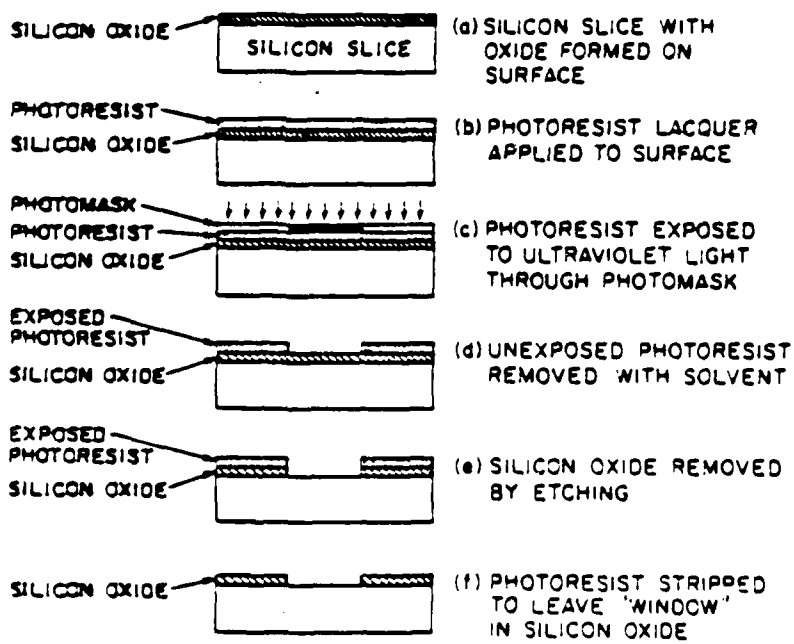


Fig. 1. Selective oxide removal by the photoresist process.

made in this way, and it is obviously of importance to be able to measure the width of the holes so cut, the shape of the edges of the holes, and the thickness of the individual layers that are being formed.

Further steps in the process may be carried out, as illustrated in Fig. 2. Similar kinds of measurements are required at each step. Each of the features that must be measured are presently of the order of one to a few micrometers in width; as progress is made, the requirements become more and more severe, down to 0.5 μm or even less. As there may be several hundred thousand devices built on one chip, it is impractical, regardless of the measurement system used, to measure every device on the chip; the information content is too large. What can and should be done is to measure test samples on each chip to evaluate whether the processing methods employed are working correctly.

A similar set of problems occur with magnetic recording disks and heads. A simplified illustration of such a recording disk and head is shown in Fig. 3, listing some of the properties that need to be measured. In magnetic recording, the magnetic recording head floats on an air bearing a few thousand Angstroms away from the disk on which the recording is made. The disk is typically of aluminum with a ~1 μm thick layer of ferrite-filled epoxy laid down on it. The thickness of the air gap is of great importance.

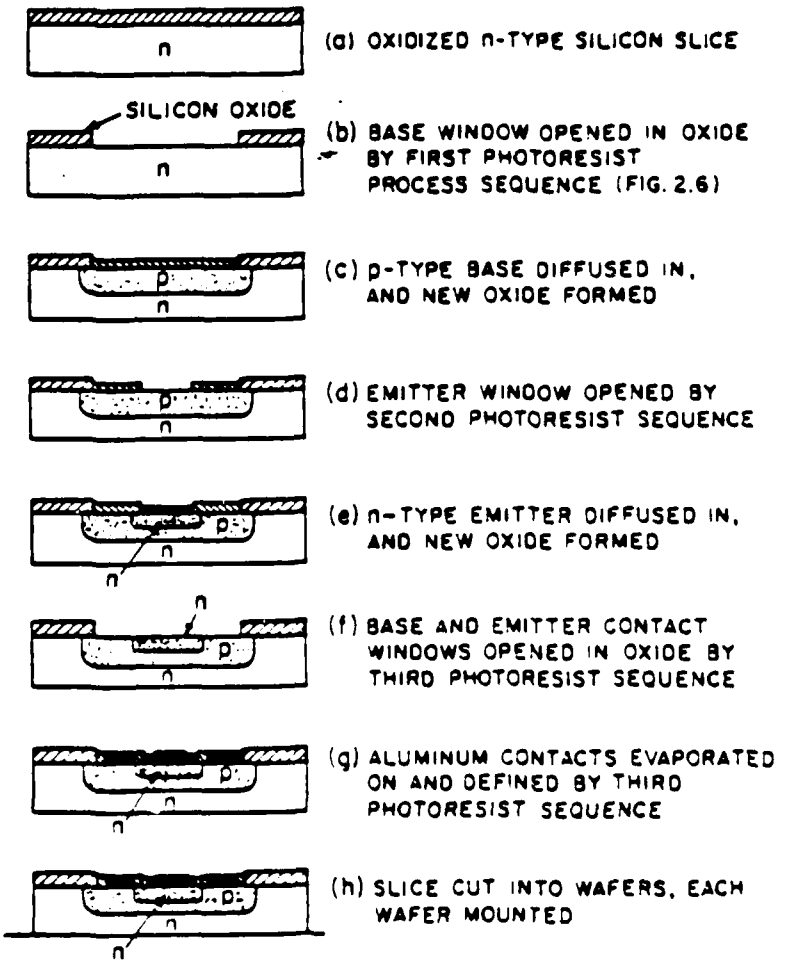


Fig. 2. Steps in the diffused planar process.

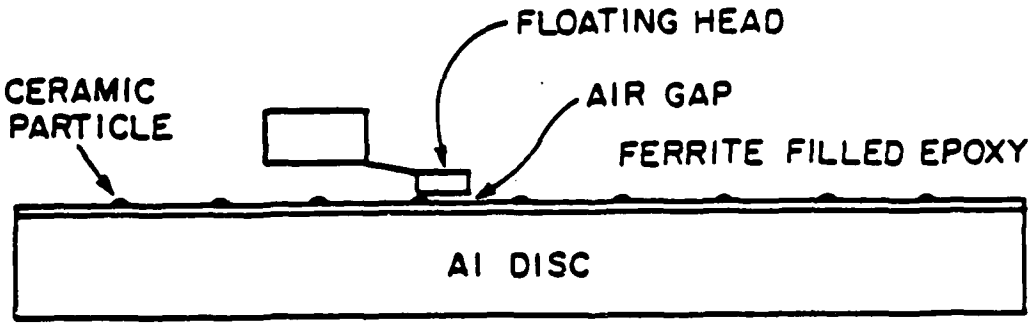


Fig. 3. Simplified schematic of a magnetic disk and head. Need to measure: surface waviness, roughness, thickness of epoxy, filling factor, air gap, head surface, stress profile.

The filling factor of the epoxy must be known and the thickness and waviness of this layer must be controlled very carefully. Furthermore, in order to stop the head from "crashing" on the disk as the disk slows down, ceramic particles are distributed in the epoxy on which the head can rest. Other problems occur in the manufacture of the head itself. Stress in the ceramic material of the head can cause it to bow. Careful control of its surface finish and its flatness are required, as well as measurements of the air gap between the disk and the head and measurements of the disk itself.

The types of sensors which can be used to make the required measurements are varied, but are basically scaled down versions of the sensors normally used in NDE applications. Thus, the optical and acoustic sensors required typically become microscopes of one kind or another, as often the photoacoustic sensors become. A summary of the types of sensors that could be used is given in Table 2.

We shall now discuss some examples of the sensors which can be used and which we have tried in simple applications.

Table 2

TYPES OF SENSORS

| | |
|---|---|
| Optical: | Scanning and Standard Microscopes |
| Acoustic: | Range Sensors, Scanned Microscope. Acoustic Wave Propagates in Solids, Liquids, or Air. |
| Photoacoustic: | Measures Thermal Effects in Solids, Liquids and Air. Also Measures Electronic Effects in Semiconductors. |

## THE ACOUSTIC MICROSCOPE

The scanning acoustic microscope was developed at Stanford by Calvin Quate and his co-workers.[1] An early version of this microscope is illustrated in Figs. 4 and 5. An acoustic transducer on a sapphire or quartz substrate excites a plane wave. A spherical hole is cut into the opposite surface of the sapphire or quartz substrate. This forms a spherical lens which produces a tightly focused beam in water. The focused beam, which impinges on the material being examined, is reflected from it and received back again at the transducer. As the reflectivity of the material being examined varies with its surface properties, the intensity of the received image from a small region controlled by the focused beam will depend on the nature of the material being examined. A two-dimensional image is obtained by mechanically scanning either the sample or the transducer using essentially a loudspeaker movement for a scan in one direction, and a slower mechanical scan for the scan in the other direction. Thus, a raster image is obtained which can be displayed on a video screen. The definition of the system is comparable to the wavelength in water so that at a frequency of 3 GHz , the definition is of the order of 4000-5000 Å with correspondingly poorer definitions at lower frequencies. Definitions of 300 Å have been obtained with liquid helium as the operating medium.

The contrast of the image is determined not only by the reflectivity of the surface, but also by the phase of the reflected waves, as illustrated in Fig. 6.[2] Suppose the beam is focused so that the focal point is below the surface of the solid. It is then possible for the lens to excite Rayleigh or surface waves on the substrate, which can be reflected back to the lens and received by it. Only certain rays from the lens cause Rayleigh wave excitation. These rays are incident at an angle $\theta_R$ where

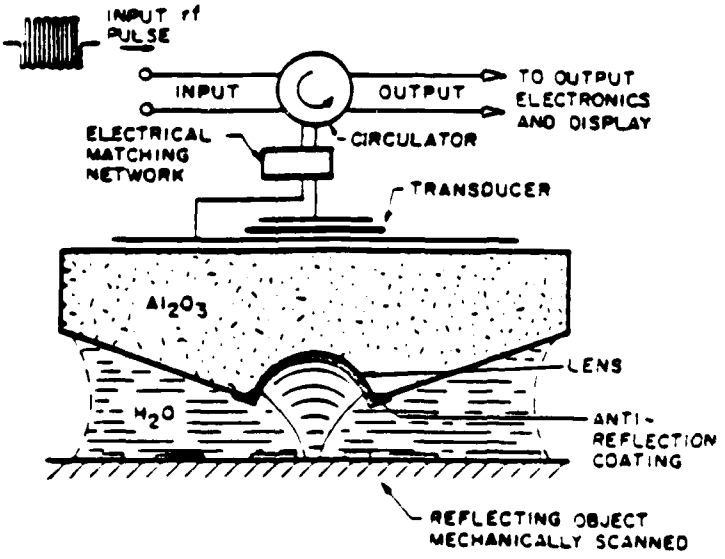


Fig. 4. Schematic of acoustic microscope.

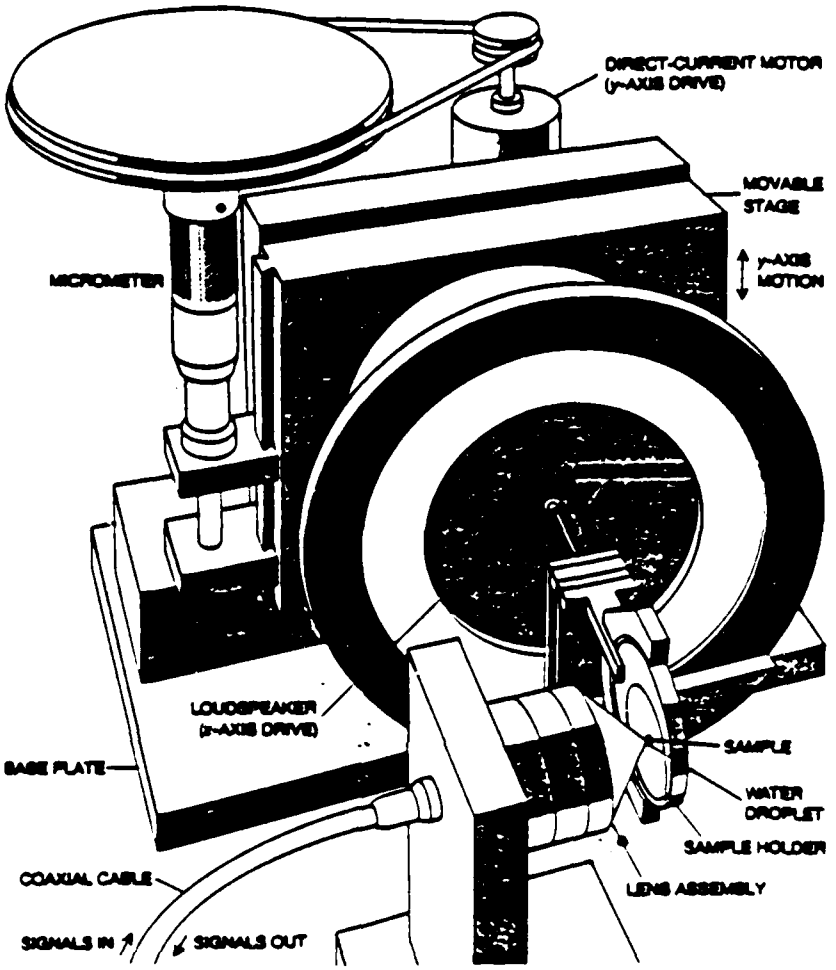


Fig. 5. Mechanical scanning of the sample in two dimensions is accomplished in the present version of the Stanford acoustic microscope by means of the apparatus depicted here. The round disk holding the sample is displaced horizontally 100-200 μm by a loudspeaker vibrating at a frequency of 60 Hz. The vertical displacement of the sample and the loudspeaker assembly are driven by a direct-current electric motor (the vertical motion is much slower than the horizontal motion). The reflected acoustic signals from the sample are processed electronically and are used to modulate the intensity of the electron beam in a television monitor. The image is formed by scanning the electron beam across the screen in synchrony with the motion of the sample across the focal point of the acoustic beam. It is the ratio of displacements of the two beams that determines the magnification of the final image.

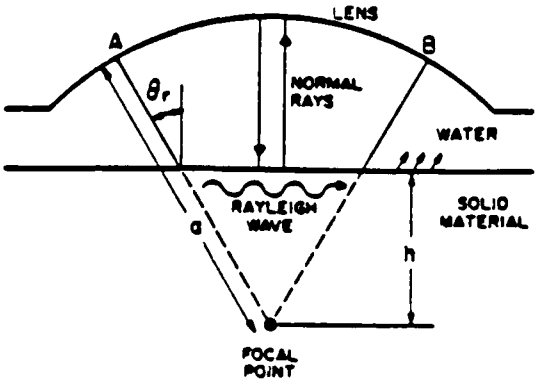


Fig. 6. Specular and Rayleigh reflected waves in the acoustic microscope.

$$\sin \theta_R = V_W V_R$$

where $V_W$ is the acoustic wave velocity in water, and $V_R$ is the Rayleigh wave velocity on the solid.

As shown in Fig. 6, two signal components arrive back at the lens, those which follow the Rayleigh wave path and those which are specularly reflected from the surface. These two sets of rays can interfere with each other and may add in phase or out of phase, depending on the distance $z$ of the focal point from the surface. As the lens is moved up and down, the voltage $V(z)$ received by the transducer varies with $z$. As the lens is moved across a surface whose material properties vary, $V(z)$ will vary. Therefore, the contrast changes obtained with the microscope are very sensitive to surface properties.

Fig. 7 is an illustration of an image of a metal film laid down on a glass substrate.[3] The optical images shown for comparison and the images obtained at two different values of $z$ are also shown. It will be seen that the contrast changes with $z$. The poor adhesion of the metal films near their edges shows up very clearly in the acoustic microscope pictures, but is not observed optically. This is because the Rayleigh wave velocity varies radically with the adhesion of the metal film. Consequently, acoustic microscopy techniques can be very useful for measuring adhesion, bonding and other mechanical properties which are difficult to evaluate by other techniques.[3]

We have attempted to put acoustic microscopy on a more quantitative basis and have arrived at techniques for measuring the phase and the amplitude of the reflected signal components separately.[4,5] This makes it possible to determine the height and width of surface features separately, as well as to determine sur-

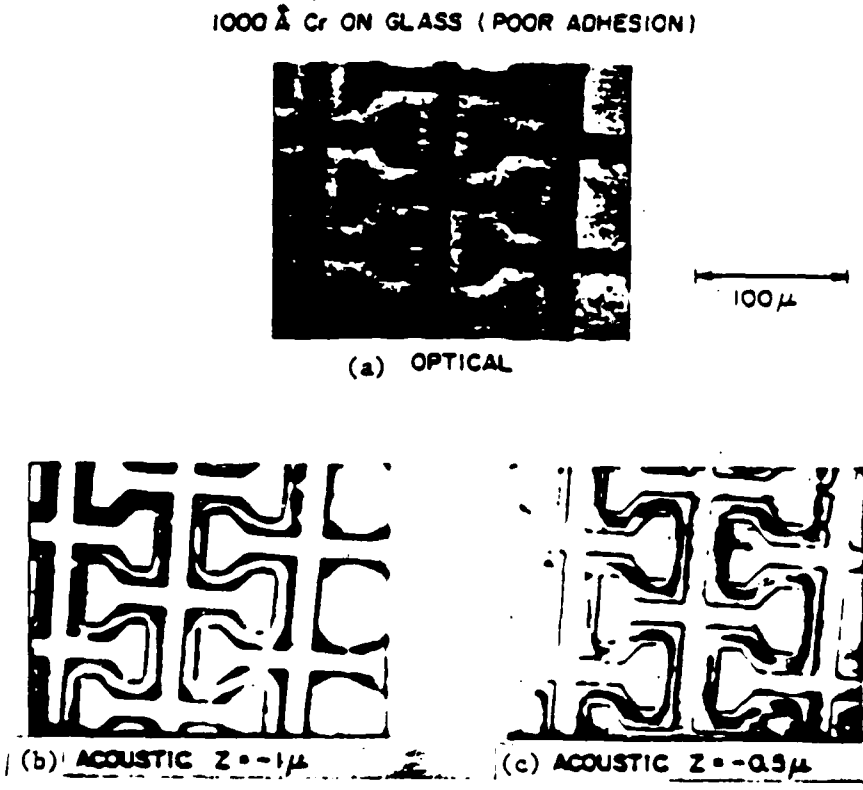


Fig. 7. Images of a metal film on glass. (a) An optical image. (b) An image taken with a 2 GHz acoustic microscope. (c) An image with a defocus distance of $-0.5\,\mu m$ .

face material properties from the measurement of the Rayleigh wave velocity. It also makes it possible to carry out Fourier transforms of the reflected image and other kinds of processing since both amplitude and phase information are available. The technique employed is illustrated in Fig. 8. A short tone burst is inserted into the transducer and is reflected from it. The specularly-reflected component arrives at a different time from the Rayleigh wave component so that they can be measured separately. Using this technique, we can determine the phase difference between these two signals to an accuracy of $0.1^{\circ}$ which corresponds to being able to measure the Rayleigh wave velocity to one part in $10^{5}$ .

In an alternative mode of operation, we excite a hollow beam on an outer ring surrounding the lens. This beam is reflected from the substrate and is used as a reference. We compare it with the reflection from a focused beam whose focal point is at the surface of the substrate. We can control the average height of the transducer from the substrate by comparing the phase of the signal returned from the reference beam (several millimeters in diameter) with an external reference; we use a piezoelectric

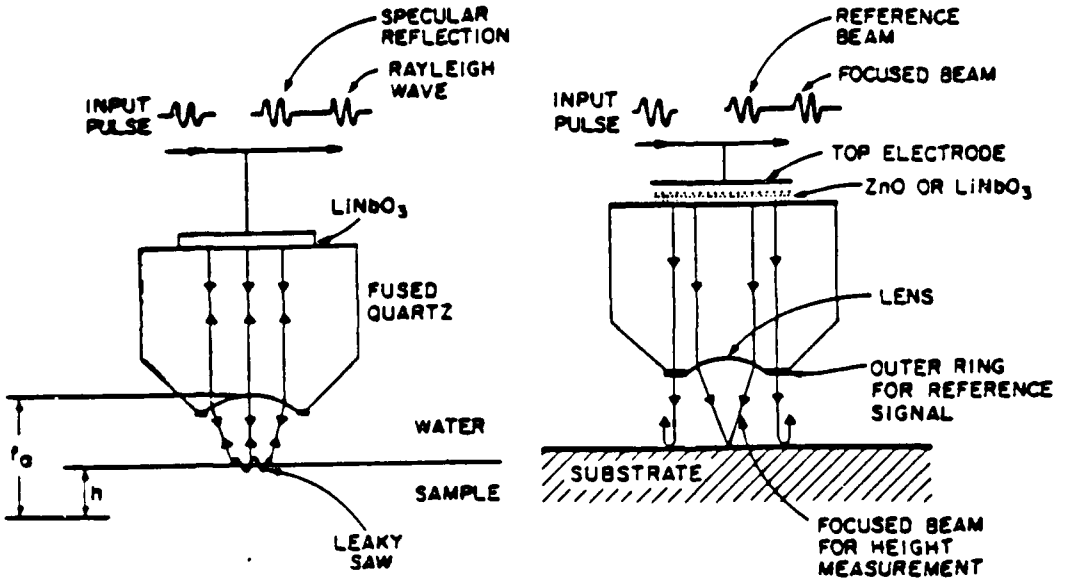


(a) (b)

Fig. 8. (a) Rayleigh wave velocity measurement. (b) Acoustic microscope lens for topography profiling.

pusher to move the transducer up and down. As the transducer is moved across the substrate, the phase of the specularly-reflected focused beam (~30 μm diameter) gives an accurate measure of the height of the region being observed. By this means, we can measure changes in height of the surface to an accuracy of $\lambda/3000$, where $\lambda$ is the acoustic wavelength in water.

An example of work by Liang, Bennett, Khuri-Yakub and Kino is shown in Fig. 9, in which these techniques were used to measure the thickness of a 5000 Å layer of aluminum using 50 MHz acoustic waves with a wavelength of 30 μm.[4] The Rayleigh wave technique was then used to measure the velocity of a surface wave along the alumimum, thus giving a measure of the material properties of the surface.

The technique can also be used to measure the width of surface features very accurately. Using the focused beam, and measuring its phase, we have been able to measure the width of surface films whose widths are quite comparable to the spot size of the beam. By using Fourier transform techniques, it is possible to put these measurements on a highly quantitative basis in which the results do not depend too critically on the fact that the focus of the beam is exactly at the substrate.[6] Thus, acoustic microscopy and related scanning optical microscopy techniques can be very useful in this application.

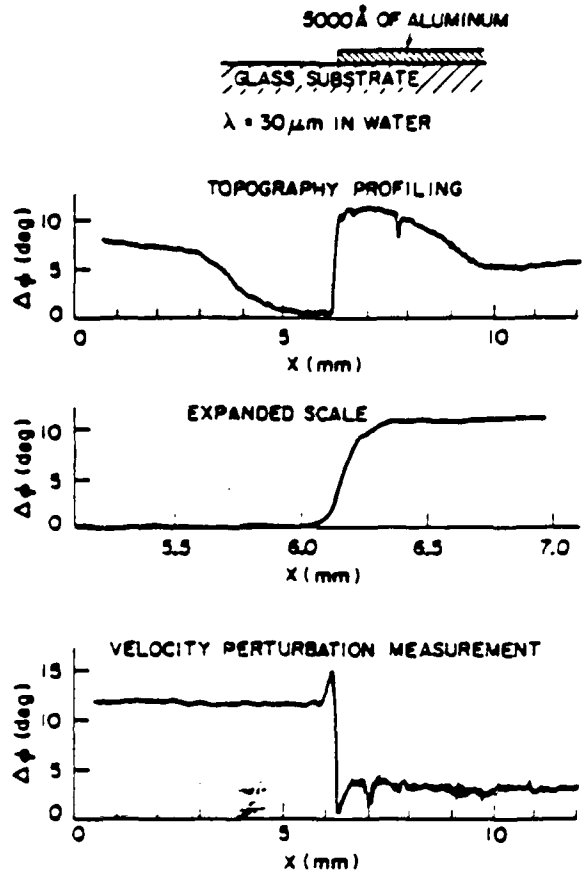


Fig. 9. Measurements and topography of velocity perturbation taken with a 50 MHz acoustic microscope.

SCANNING OPTICAL MICROSCOPE

After we were able to obtain good phase and amplitude information directly with a scanned acoustic microscope, we were prompted to see if we could duplicate this kind of operation with an optical microscope. One of the problems with scanning optical microscopy, or any kind of quantitative microscopy for that matter, is that, because of the precision required, vibrations can cause great difficulty in measurements. Therefore, a very solid optical bench and other equipment are needed. One of our aims was to eliminate this difficulty; another was to use modern electronic signal processing techniques to measure phase to an accuracy of a few degrees rather than using standard optical interference techniques. This would make it possible to measure, simultaneously, the width and height of surface profiles using the same system. Presently, such measurements of width can typically be made with one kind of device, and measurements of height with another, but it is not usually possible to measure the height or thickness accurately in regions of very small transverse dimensions.

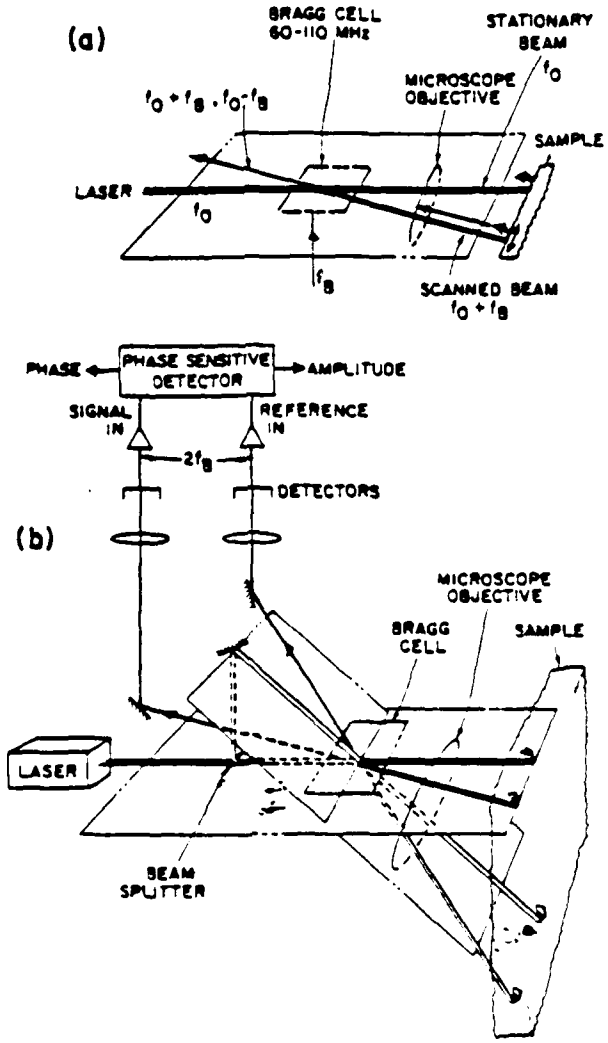


Fig. 10. Scanning optical microscope. The Bragg cell splits the input beam and scans the deflected and frequency shifted beam across the sample. The undiffracted beam is used as a reference. (a) Simplified schematic. (b) Secondary reference on sample to compensate for surface tilt.

The system we have developed is an electronically-scanned optical microscope with a stationary reference on the sample so as to eliminate the effect of vibrations. The basic device is shown in Figs. 10a and 10b. A laser beam of frequency $f_0$ is passed through a Bragg cell whose frequency can be varied from 60-110 MHz . The Bragg cell deflects the acoustic beam. The deflection angle is linearly proportional to the frequency $f_B$ , the input to the Bragg cell. A deflected and undeflected beam pass through a microscope objective lens, producing two focused spots on the surface of the sample. The incident beams are reflected from the sample, pass again through the Bragg cell, and produce two signals along the path shown; these signals are of frequencies $f_0 + f_B$

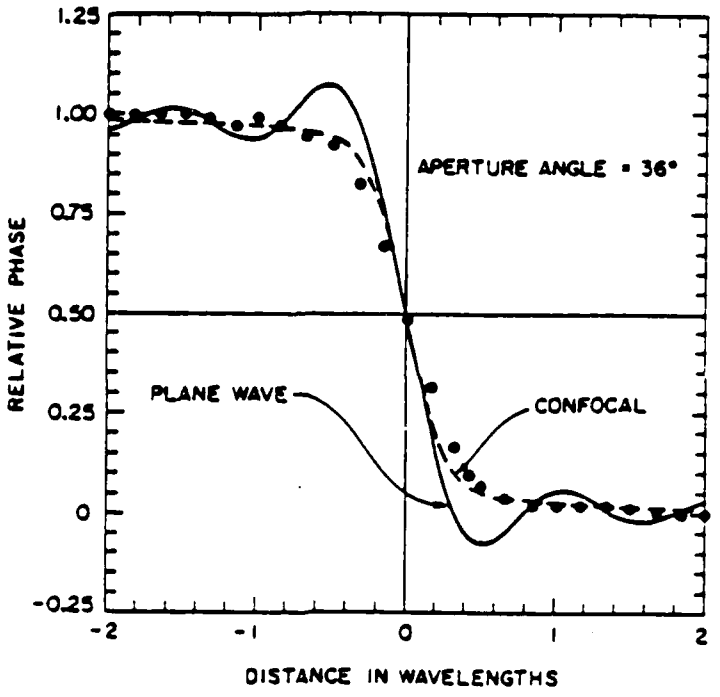


Fig. 11. Theoretical and experimental phase profiles of a step taken with plane wave illumination (solid line) and a confocal lens system (broken line).

and $f_0 - f_B$, respectively. The phase difference between these two signals is equal to the optical phase difference of the two reflected beams from the sample. By passing the received beams into a photodetector, a product signal is obtained from the photodetector at a frequency $2f_B$ whose amplitude depends on the amplitude of the scanned beam and whose phase is the phase difference of the signals of the two beams. We therefore have arrived at a technique for measuring the phase and amplitude of the optical beams, but carry out this measurement at frequencies that can be handled by electronic circuitry.[6]

The actual system is somewhat more complicated because it is necessary to provide a reference signal at a frequency $2f_B$. Since there is a phase change from the input signal to the Bragg cell to the point where the optical beam is incident, and this phase change varies with frequency, and hence deflection angle, it is necessary to eliminate this error. We do this by using two incident beams on the Bragg cell, as shown in Fig. 10b, obtaining the reference signal from the second set of beams. The second set of beams is passed through a narrow aperture and therefore produces two wide beams on the sample whose transverse size is perhaps fifty times that of the well-focused spot. Therefore, as the secondary set of reference beams is scanned by the Bragg cell, it is not much affected by fine changes in surface profile.

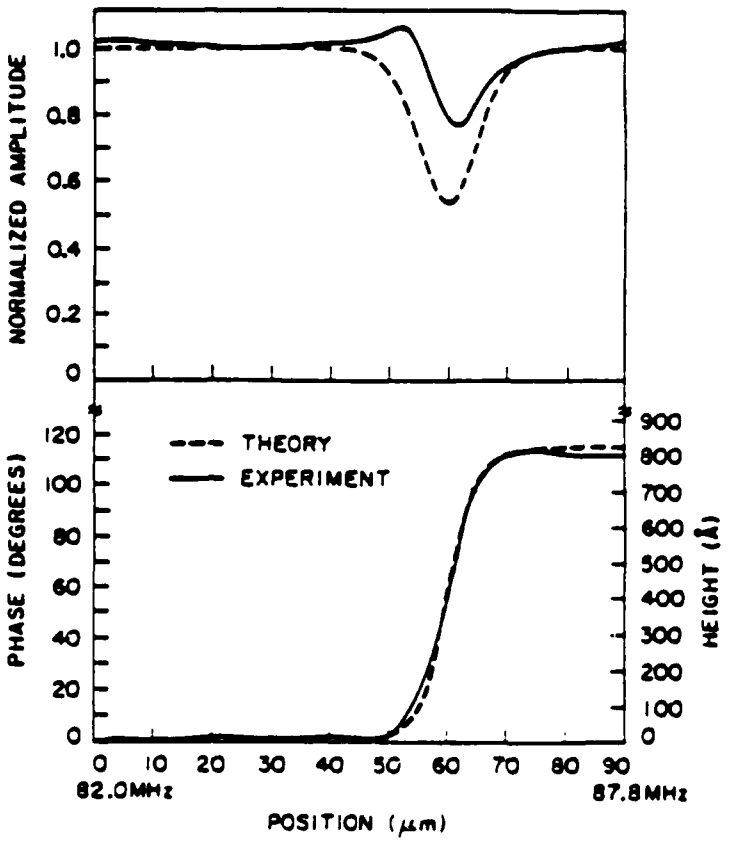


Fig. 12. Amplitude and phase variation across an aluminum step on a metallized substrate. The phase step indicates a height of 820 Å .

A major advantage of this reference system is that it is neither sensitive to vibration normal to the lens, or to tilt. The operating system is so insensitive to these parameters that banging on the optical bench with a hand has very little effect.

Another advantage of such a scanned optical system is that, because the same beam is used for transmission and reception, the point spread function of the lens is squared. Hence, the sidelobe levels are extremely low, and there is very little ripple when one observes sharp steps. We have carried out a detailed theory to predict what should occur and have carried out measurements to confirm our theory. Some simple results which were obtained for the acoustic microscope are shown in Fig. 11.[4,5] As the beam is passed over a step, the transition is extremely smooth as opposed to what would be expected theoretically for a plane wave illumination, where the transition shows some ripple. The theoretical profile to be expected for this confocal scanned system is shown as the dashed line; the experimental results for the acoustic microscope are shown as points. The agreement is excellent.

We have used this optical microscope to obtain the results shown in Fig. 12; in these preliminary experiments we measured a step of 800 Å of aluminum on aluminum.[5] It will be seen that

the measured phase is in good agreement with what would be expected. The amplitude profile is only in fair agreement with what would be expected; later results indicate far better agreement than shown here.

## PHOTOACOUSTIC TECHNIQUES

Photoacoustic methods are ideal for measuring thermal properties of materials such as the integrity of a bond between a silicon substrate and a heat sink, the lack of adhesion of a metal film, the presence of near-surface defects in materials, and the integrity and quality of current-carrying conductors. Related techniques can also be useful for measuring electronic properties of materials such as doping density profiles and recombination rates of carriers. We shall describe here a subset of problems of this nature which we have investigated. Other related problems are described in a paper in this issue by Stearns et al.[7]

The technique we have employed is different from conventional photoacoustic methods. Most commonly, a heat source such as a modulated light beam is incident on a sample.[8] This modulates the near-surface temperature of the sample. In turn the thermal expansion and contraction of the material, caused by the change in temperature, excite an acoustic wave in the material which is detected with an acoustic transducer on the opposite side of the sample. An alternative method, which has been used extensively, is to measure the acoustic wave generated in the air above the sample.

In one example, shown in Fig. 13a, we excite an acoustic surface wave with a wedge transducer placed on the sample and receive it on a similar transducer.[8] The modulated light incident on the sample changes its near-surface temperature. This temperature modulation in turn varies the phase of the received signal. Thus, with this technique, the laser heating perturbs an acoustic wave rather than excites one. A second method, shown in Fig. 13b, uses an acoustic wave incident on the surface of the substrate from a focused transducer in air; the reflected wave is received on a second transducer. The phase change of the acoustic wave caused by the temperature modulation of the air yields a direct measurement of temperature. The technique is extremely sensitive and can be operated over a broad band of frequencies. It also has the advantage that it can be used to localize the region being examined. In another example of the technique, an acoustic microscope excites acoustic surface waves so that we can examine regions where the temperature is modulated on the surface of a material. In this case we obtain the transverse definition of the acoustic microscope.

An accompanying paper by Stearns et al includes a discussion on how these techniques can be exploited to measure the thermal properties of silicon bonded to a heat sink.[7] We shall therefore not discuss thermal measurements any further. Instead, we shall focus on the utility of alternative methods which measure the electronic properties of a semiconductor.[9]

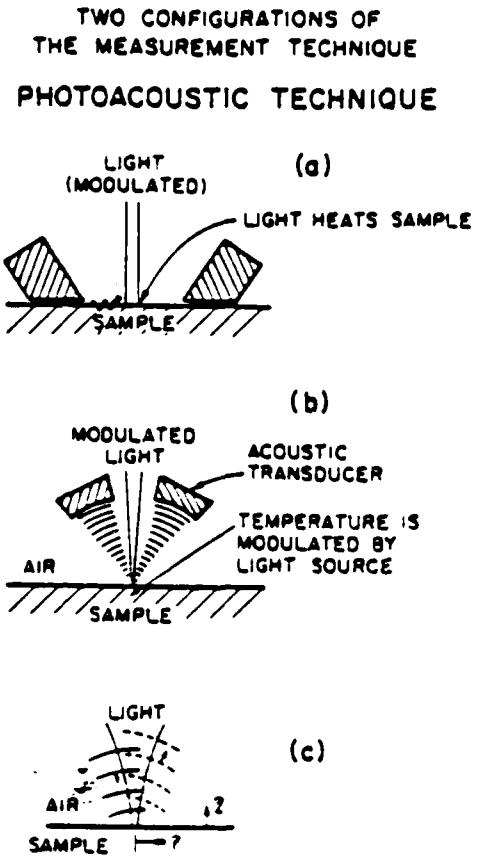


Fig. 13. Configuration of a photoacoustic measurement technique. (a) Surface wave measurement with a wedge transducer. (b) Acoustic transducer in air. (c) An illustration of the path of a light beam and acoustic beams in air.

Suppose we use the configuration of Fig. 13a with argon light incident on a silicon sample. In this case, the light will generate electrons and holes. The electrons and holes will, in turn, perturb the acoustic surface wave velocity. The perturbation will be proportional to the carrier density. As the frequency of modulation is increased, the phase perturbation will not change in amplitude until the modulation frequency becomes comparable to the recombination frequency of the carriers. At this point the effects begins to fall off. At very low frequencies temperature effects are also important.

Some results taken on a P-type silicon sample are shown in Fig. 14. It is seen that the magnitude of the effect falls off, as predicted. Furthermore, the phase of the perturbation relative to the phase of the input chopping signal also changes, as illustrated in Fig. 14b. It will be seen that the phenomenon is well understood, and the agreement between experiment and theory is excellent.

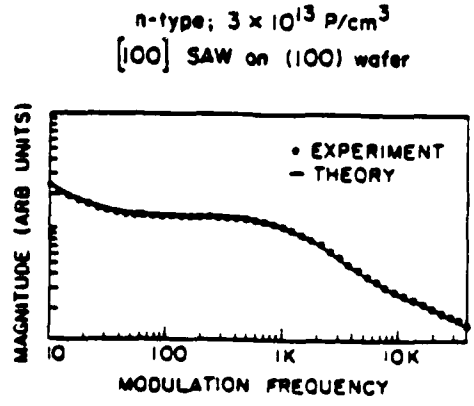


Fig. 14. Acoustic phase perturbatin in Si.

The technique, therefore, provides a method of measuring recombination rates of carriers in a small region of the semiconductor. If an acoustic microscope is used for exciting the surface waves, then no contact need be made to the semiconductor.

## CONCLUSIONS

We have discussed a number of techniques for examination of electronic devices. Due to limitations of space, we have concentrated on only a few of the available methods. The acoustic and optical microscopes are very powerful tools for measuring mechanical properties, adhesion surface profiles, and sizes of small features. Photoacoustic techniques are useful for measuring thermal properties of materials; they can also be used for measuring electronic properties. Related techniques may be useful for measuring doping profiles in materials without making contact with the surface.[10] Other techniques, which employ acoustic waves excited in air, are also being developed for measuring surface profiles. The great advantage of these techniques is that the surface is not contaminated by the probing technique itself.

## ACKNOWLEDGMENT

This work was supported by the Air Force Office of Scientific Research under Contract No. F49620-79-C-0217, the Office of Naval Research under Contract No. N00014-78-C-0283, and the NSF-MRL Program through the Center for Materials Research at Stanford University.

## REFERENCES

1. R. A. Lemmons, C. F. Quate, "Acoustic Microscopy," in Physical Acoustics: Principles and Methods, Eds: W. P. Mason and R. N. Thurston 14, Academic Press, New York (1979).
2. A. Atalar, "A Physical Model for Acoustic Signatures," J. Appl. Phys. 50, 8237-8239 (1979).
3. R. C. Bray, J. Calhoun, R. Kock, and C. F. Quate, "Film Adhesion Studies with the Acoustic Microscope," J. Thin Solid Films 74, 295-302 (1980).

4. K. Liang, B. T. Khuri-Yakub, S. D. Bennett, and G. S. Kino, "Phase Measurements in Acoustic Microscopy," Proc. IEEE Ultrasonics Symp., Atlanta, Georgia (October 1983).
5. K. Liang, S. D. Bennett, and G. S. Kino, "Precision Phase Measurements with the Acoustic Microscope" submitted to IEEE Sonics and Ultrasonics for the Special Issue on Acoustic Microscopy (March 1985).
6. R. L. Jungerman, P. C. D. Hobbs, and G. S. Kino, "Phase Sensitive Scanning Optical Microscope," submitted to Appl. Phys. Lett. (June 1984).
7. R. G. Stearns, B. T. Khuri-Yakub, and G. S. Kino, "Phase-Modulated Photoacoustics," presented at the DARPA/AF Review of Progress in Quantitative NDE, San Diego, California (July 1984).
8. R. G. Stearns, B. T. Khuri-Yakub, and G. S. Kino, "Phase Modulated Photoacoustics," Proc. IEEE Ultrasonics Symp., Atlanta, Georgia (October 1983).
9. R. G. Stearns, B. T. Khuri-Yakub, and G. S. Kino, "A Photoacoustic Technique for Measuring Excess Carrier Density and Lifetimes in Silicon," submitted to Appl. Phys. Lett. (June 1984).
10. G. S. Kino, J. D. Fox, and B. T. Khuri-Yakub, "Very High-Frequency Acoustic Transducers for Operation in Air," presented at the Second Symposium on Energy Engineering Sciences, Argonne National Laboratory (April 1984).

END

4-87

DTIC